The investigation of an inexpensive infra-red camera based building monitoring system for the aid of efficient building development.

Prepared by:

N. M. Vorajee

Student Number: VRJNAA002

Supervised by:

Dr. Amit Kumar Mishra

Department of Electrical Engineering

October 2019

A dissertation submitted to the Department of Electrical Engineering,

University of Cape Town,

in partial fulfilment of the requirements

for the degree of

Master of Science in Engineering specializing in *Mechatronic Engineering.*

October 6, 2019

Declaration

I know the meaning of plagiarism and declare that all the work in the document, save for that which is properly acknowledged, is my own. This thesis/dissertation has been submitted to the Turnitin module (or equivalent similarity and originality checking software) and I confirm that my supervisor has seen my report and any concerns revealed by such have been resolved with my supervisor.

1. I know that plagiarism is wrong. Plagiarism is to use another's work and pretend that it is one's own.
2. I have used the IEEE convention for citation and referencing. Each contribution to, and quotation in, this report from the work(s) of other people has been attributed, and has been cited and referenced.
3. This report is my own work.
4. I have not allowed, and will not allow, anyone to copy my work with the intention of passing it off as their own work or part thereof.

Signature: Signed by candidate

N. M. Vorajee

Date: 06 October 2019.

Acknowledgements

A project such as this could not have been possible without the help of the individuals mentioned below. I would like to sincerely thank all those who played a role in this project; from the small comments from individuals on how to better my design, to the lending of a simple tool to those who assisted me on a daily basis with the implementation, I am truly grateful to you all.

Firstly, I would like to than my supervisor, Associate Professor Amit Mishra for guidance from our regular meetings that always kept me on par with my goals and ensured that I would think outside the box. I am a truly privileged individual to have been supervised by him. I thank him for all the knowledge, interesting facts and new ideas that he has passed down. Apart from his guidance, his friendship has been a constant help throughout this process. In addition, his versatility and plethora of knowledge has pushed me to look beyond the scope of this project and intrigued me in th the field of Engineering as a whole. I am forever in debt to him.

All the member of the radar lab, Imraan Khan, harpreet Singh, Kathleen Macwilliam, Matthew Pike, Wian Van Zyl, Asif Parker and Ming Gao. Thank you for making everyday a pleasure to work. Their stories of travel, work and research have pushed me to work harder and open my mind to issues beyond the common engineering problems that we face in our everyday lives. I hope that one day I will be able to work with such a diverse group of individuals again.

I'd like to thank all the workshop staff for their dedicated service, expertise and ideas: Phillip Titus, Riyaad, Masi, Maysam, Mr Dominique de Maar, Justin Pead, Brendon Daniels and Tashrique Karriem. With over 100 years of experience collectively, words cannot describe how grateful I am for their support and attention to detail. A special thanks to Tashrique and Phillip: For arriving earlier than the specified working hours and leaving later just so that I could complete my work. It is truly a pleasure to work when such dedication is shown.

I would like to thank my EEE class friends. No part of my project could have been possible without the help of Nadeem Wagley and Farhanah Latief. Special thanks must be given to them for all the consultations and ideas.

I would also like to thank additional academic members, in particular, Dr Yunus Gaffar for his consultations on life and the ideas thereof and my second supervisor Dr. Asit Mishra for firstly allowing me to work on this topic and secondly for his constant, structured guidance and expertise in this field.

A huge thanks must go to my family. My dearest late aunt, whose long fight with cancer has always been an inspiration for me, for always believing in me and motivating me. May her soul rest in peace. My Mom, Rayisa Vorajee and Dad, Mohamed Vorajee for their continuous support through my poor health and positive attitude towards my work. Nadia and Naai'la, my sisters, as well as Muhammed Ameen deserve as much credit for always being there in times of need. I am very lucky to call you all my family. It has been an honour to share these 6 years of study with you all.

Lastly, I would like to thank my dearest friends, Miss Sarah Tandy, Mitchell Usayiwevu, Navya George, Tia Pillay, Nirav Beni, Ally Barry, Sadiya Bux, Tessa Smythe, Zaynab Asmal, Thami and Mr. Jonathan Nothling for their advice throughout my studies and constant belief in me as an individual.

Abstract

As the world is moving toward a greener, more sustainable future, the use of HVAC (Heating, Ventilation and Air-conditioning) systems are detrimental toward providing more efficient structures. Current UAVs (Unmanned Aerial Vehicle) used for surveying purpose are highly priced, with costs ranging upwards of R25 000. In this project, we propose a possible cost effective solution, with a budget of R10 000, that can be used in order to accurately survey a building for cracks and thermal inefficiencies within the envelope of the building. The project proposes a low cost Thermal camera to be used for the surveying as well as a validation of thermal camera for temperature reading. The project also proposes a low cost drone to be used for the possible prototype.

The project follows a typical engineering design approach, specifically via the use of a V-model for the thermal camera used for image processing. After the constraints and requirements were defined, the engineering design commenced with a careful selection of both the IR camera and drone to be used for the possible prototype. Thereafter, experiments were set up to validate the use of the drone and IR camera as a viable option as a tool for building envelope surveyance.

There were 6 experiments that were recorded during the process of this project. Firstly as statistical validation occurred through four tests whereby the thermal camera was validated with a mercury thermometer for temperature measurement. The second experiment was focused on the capability of the thermal camera to detect anomalies in a structure. This experiment made use of 3 holes of varying size drilled into a ceramic material with a heat source behind. Thermal images were then taken at various distances and then processed accordingly.

The third experiment was focused on the ability to detect the area of the anomaly given a known distance from the thermal camera to the anomaly. The experiment followed the same set-up as described in the second experiment, however instead of 3 holes of varying size, only one hole was used. The fourth experiment looked at the building envelope and was focused on developing an algorithm to calculate the weighted average of the temperature of the structure rather than using the given structure temperature at a single point. In addition, the experiment qualitatively showed a difference between new and older insulation types. The fifth experiment focused on the development of an algorithm that would result in automatic image segmentation. The sixth experiment focused on the low cost drone and its ability to be used to survey a building.

All experiments were successfully carried out. The thermal camera was validated as a reliable source for temperature measurement and could be used to detect anomalies as

small as 3mm in diameter from a distance of 750mm from the target. In addition, an algorithm was developed that could be used to automatically tell the user the area of the anomaly with a 95% accuracy in certain cases. An algorithm was also developed to indicate the weighted mean temperature of an area of a building envelope. Lastly, the drone was successfully used to survey a building via the use of a developed protocol.

Contents

1 Introduction **1**

1.1 Background to the Study 1

1.2 Objectives of this Study 2

1.2.1 Problems to be Investigated 2

1.2.2 Purpose of the Study 3

1.3 Scope and Limitations 3

1.4 Plan of Development 4

1.4.1 Literature Review 4

1.4.2 Requirement Analysis 4

1.4.3 Engineering Designs 4

1.4.4 Experiment Designs 4

1.4.5 Conclusions and Recommendations 5

1.4.6 Future Work 5

2 Literature Review **6**

2.1 Infra-Red Radiation 6

2.2 Thermography 7

2.3 Thermal cameras and IR sensors 15

2.4 Digital images 19

2.5 Image Segmentation Techniques 21

3 Requirement Analysis **28**

3.1 Requirement Baseline 29

3.2 Functional Requirements 31

3.3 Performance Requirements 31

3.4 Design Requirements 32

3.5 Acceptance Test Procedures (ATP) 32

3.6 Constraints 33

4 Engineering Design **34**

4.1 Conceptual Design 34

4.2 Device Selection 35

4.2.1 Infra-red Cameras 36

4.2.2 Drone selection 39

4.3 Segmentation Algorithm Selection 42

4.3.1 Global Thresholding 44

4.3.2 Adaptive Thresholding using Otsu's Method 45

4.3.3 Edge-Based Segmentation 46

4.3.4 Region-Based Segmentation 47

4.3.5 Segmentation Results 48

5 Experiment Designs **51**

5.1 Sensor Validation 51

5.1.1 The temperature accuracy test 51

5.2 Infra-Red Camera Testing 60

5.2.1 The detection test 60

5.2.2 The Area Test 67

5.2.3 The building envelope test 83

5.2.4 The building envelope insulation test 87

5.3 IR-Drone Automation Experimentation 95

5.3.1 Automatic segmentation algorithm tests 95

5.3.2 The drone flight test 108

6 Conclusions, Limitations and Future Work **119**

6.1 Conclusions 119

6.2 Limitations 121

6.2.1 IR Camera Limitations 121

6.2.2 Drone Limitations 122

6.3 Comparisons 122

6.4 Future Work 123

List of Figures

2.1 *The electromagnetic spectrum with indication of wavelength and frequencies* 7

2.2 *The PMV sensation scale* 9

2.3 *Two thermal images of a room. The picture to the left uses a wide-span whilst that on the right uses a narrow span* 11

2.4 *Figure showing the total emissivity coefficients of common materials* 12

2.5 *Figure indicating the developed protocol for IR-UAV flights to survey building thermography in the construction domain* 15

2.6 *General block diagram depicting formation of IR image.* 15

2.7 *General representation of IR devices.* 16

2.8 *The created voltage output of a pyroelectric sensor.* 17

2.9 *The workings of the Seebeck Effect.* 18

2.10 *The general layout of a microbolometer* 19

2.11 *Indication of the levels of grey in an 8-bit scale* 20

2.12 *Indication of the 24-bit RGB ideology.* 21

2.13 *Image Segmentation Techniques Adapted from:* 22

2.14 *The process of histogram - based segmentation via thresholding* 23

2.15 *The process of Canny filtering used for Edge detection* 26

2.16 *A basic optical image used to explain the watershed algorithm.* 27

2.17 *The side view of the optical image above if transformed to basins.* 27

4.1 *General design philosophy of the Quadcopter and IR camera used for the prototype of this project.* 34

4.2 *A geometrical interpretation of equation 1.* 36

4.3 *Process flow of the infra-red resolution and contrast enhancement with fusion.* 38

4.4 *FLIR 1 (a) and SEEK Thermal (b) IR images of a target object.* 38

4.5 *An image of the DJI Phantom Drone, which could be used for the purpose of surveying.* 39

4.6 *An image of the DJI Spark Drone, which could be used for the purpose of surveying.* 40

4.7 *An image of the Up Air One Drone, which could be used for the purpose of surveying.* 40

4.8 *A plot showing the relationship between battery capacity and flight time.* . . 41

4.9 *A plot showing the relationship between Average Amp Draw and flight time.* 42

4.10 *A 3-Dimensional plot indication the plot of Flight time in minutes with respect to Average Amp Draw in amps and Battery Capacity in Amp Hours.* 43

4.11 *Figure showing a flow chart of the Global thresholding algorithm used for image segmentation.* 44

4.12 *Figure showing a flow chart of the Adaptive thresholding algorithm using Otsu's Method used for image segmentation.* 45

4.13 *Figure showing a flow chart of the Edge-Based Segmentation algorithm used for image segmentation.* 46

4.14 *Figure showing a flow chart of the Region-Based Segmentation algorithm used for image segmentation.* 47

4.15 *Figure showing the original IR image taken of the 60mm diameter hole taken at 750mm away.* 48

4.16 *Images of (a) Global and (b) Adaptive Thresholding applied to the IR image of the 60mm diameter hole taken at 750mm away.* 48

4.17 *Images of (a) Edge-Based and (b) Region-Based Segmentation applied to the IR image of the 60mm diameter hole taken at 750mm away.* 48

4.18 *Figure showing the original IR image taken of the 60mm diameter hole taken at 3750mm away.* 49

4.19 *Images of (a) Global and (b) Adaptive Thresholding applied to the IR image of the 60mm diameter hole taken at 3750mm away.* 49

4.20 *Images of (a) Edge-Based and (b) Region-Based Segmentation applied to the IR image of the 60mm diameter hole taken at 3750mm away.* 49

5.1 *Optical (a) and Thermal (b) images of the mercury thermometer tested in a cup of ice.* 52

5.2 *Optical (a) and Thermal (b) images of the mercury thermometer in water at room temperature which was kept constant at 21˚(C)* 53

5.3 *Optical (a) and Thermal (b) images of the mercury thermometer in previously boiling water in a cooling stage* 53

5.4 *Optical (a) and Thermal (b) images of the mercury thermometer placed against a PC screen at 35˚(C).* 53

5.5 *Scatter plots showing the temperatures recorded from the mercury thermometer and IR camera of the (a) Ice test and (b) Room temperature tests respectively.* 54

5.6 *Scatter plots showing the temperatures recorded from the mercury thermometer and IR camera of the (a) Boiling water test and (b) PC screen tests respectively.* 54

5.7 *Histograms showing the frequency of temperatures recorded from the mercury thermometer (a) and IR camera (b) respectively.* 55

5.8 *Histogram plot showing the overlay of data from (a) and (b) of figure 5.7 above.* 55

5.9 *The two thermal cameras, not to scale, used for this experiment (a) Seek Thermal compact 206x156 and (b) Testo 882 thermal imager (640x480).* . . . 61

5.10 *The physical setup for experiment 2.* 61

5.11 *Optical images showing the tiles used for experiment 2 with (a) 16mm, 14mm and 10mm and(b) 8mm, 5mm and 3mm respectively.* 62

5.12 *Line Graphs showing the Actual Area (red) and the Calculated Area (blue) for anomalies of (a) 60mm and (b) 40mm in diameter as taken from distances of 750mm, 1750mm, 2750mm, 3750mm and 4750mm respectively.* 78

5.13 *Line Graphs showing the Actual Area (red) and the Calculated Area (blue) for anomalies of (a) 30mm and (b) 20mm in diameter as taken from distances of 750mm, 1750mm, 2750mm, 3750mm and 4750mm respectively.* 79

5.14 *Line Graphs showing the Actual Area (red) and the Calculated Area (blue) for anomalies of 10mm in diameter as taken from distances of 750mm, 1750mm, 2750mm, 3750mm and 4750mm respectively.* 79

5.15 *Optical (a) and Thermal (b) images of the Mathematics building on UCT upper campus.* 84

5.16 *Optical (a) and Thermal (b) images of the of the Jagger Library on UCT upper campus* 84

5.17 *Optical (a) and Thermal (b) images of the Chemical Engineering building on UCT upper campus.* 84

5.18 *Optical (a) and Thermal (b) images of the of the Snape building on UCT upper campus* 85

5.19 *A comparison of old and new buildings as seen through IR images.* 85

5.20 *Internal (a) and External (b) IR images of wall of the Mathematics building on UCT upper campus.* 88

5.21 *Optical (a) and Thermal (b) images of the of the Jagger Library on UCT upper campus* 88

5.22 *Optical (a) and Thermal (b) images of the Chemical Engineering building on UCT upper campus.* 88

5.23 *Optical (a) and Thermal (b) images of the of the Snape building on UCT upper campus* 89

5.24 *A general quantitative methodology used to determine the effectiveness of an insulator with regards to thermal efficiency.* 89

5.25 *An electrical circuit analogy used to explain the derivation of equation 5.10 and the dependencies on the insulation of an insulating structure.* 90

5.26 *Figure showing the algorithm flow for the weighted-temperature algorithm used to determine the weighted-average temperature.* 93

5.27 *Figure showing the anomaly that will be used for the optimization process as the "window" of a building will be used. This image of the anomaly was taken at 750mm away and the size of the anomaly is 60mm in diameter.* . 96

5.28 *Figure showing (a) Histogram representation and (b) Entropy vs thresholds of the associated greyscale image 5.27* 97

5.29 *Figure showing (a) White Pixels vs Intensity Threshold(b) Entropy vs number of pixels of the associated greyscale image 5.27* 98

5.30 *Plot indicating the number of white pixels with respect to the intensities for an anomaly of 60mm imaged at a distance of 750mm after being passed through the optimization algorithm.* 99

5.31 *Plot indicating the number of white pixels with respect to the intensities for an anomaly of 60mm imaged at a distance of 750mm after being passed through the optimization algorithm.* 99

5.32 *Image showing the Parrot Ar.Drone2.0 quadcopter that will be used for the building survey.* 108

5.33 *Figure showing the flight path in white along the Northern breadth and side of the Mathematics Building at the University Cape Town which will be surveyed as part of the Flight test.* 114

5.34 *Figure showing the flight path in white along the length of the Mathematics Building at the University Cape Town which will be surveyed as part of the Flight test.* 114

5.35 *Figure showing the flight path in white along the Southern breadth and side of the Mathematics Building at the University Cape Town which will be surveyed as part of the Flight test.* 114

5.36 *Optical images of (a) Set-up point and (b) Southern Side Wall of the Mathematics Building during the flight test at UCT upper campus.* 117

5.37 *Optical images of the (a) North North Western roof-line and (b) Northern Side Wall of the Mathematics Building during the flight test at UCT upper campus.* 117

5.38 *Figure showing the secondary landing sight that was used for the drone flight test.* 117

List of Tables

3.1 *Table showing the Functional requirements for the proposed IR-UAV set-up.* 31

3.2 *Table showing the Performance requirements for the proposed IR-UAV set-up.* 31

3.3 *Table showing the Design requirements for the proposed IR-UAV set-up.* . . 32

3.4 *Table indicating the Acceptance Test Procedures for the proposed IR-UAV set-up.* 32

4.1 *Table indicating the specifications of various thermal cameras.* 36

4.2 *Table indicating the specifications and area per pixel of various thermal cameras.* 37

4.3 *Table indicating the specifications of selected drones for the IR-Drone set-up.* 40

4.4 *Table indicating the specifications of selected drone batteries for the IR-Drone setup.* 40

4.5 *Table indicating the results of image segmentation methods after taking thermal images with the Seek thermal Compact of an illuminated hole of 60mm diameter size taken at 750mm away.* 49

4.6 *Table indicating the results of image segmentation methods after taking thermal images with the Seek thermal Compact of an illuminated hole of 60mm diameter size taken at 3750mm away.* 50

5.1 *Table indicating the results of the Shapiro-Wilk test for the mercury thermometer and IR camera temperature readings.* 57

5.2 *Table indicating the Wilcoxon Rank statistics calculated from each of the temperature validation experiments as well as all the experiments combined.* 58

5.3 *Table indicating the thermal images taken with both the Testo and Seek thermal cameras at various distances of a tile with holes of 16mm, 14mm and 10mm diameters respectively.* 62

5.4 *Table indicating the thermal images taken with both the Testo and Seek thermal cameras at various distances of a tile with holes of 16mm, 14mm and 20mm diameters respectively.* 64

5.5 *Table indicating the results after taking thermal images with the Testo 882 Thermal imager and the Seek Thermal Compact and processing of the Seek Thermal Compact images of a tile with holes of 16mm, 14mm and 10mm holes drilled from left to right.* 66

5.6 *Table indicating the results after taking thermal images with the Testo 882 Thermal imager and the Seek Thermal Compact and processing of the Seek Thermal Compact images of a tile with holes of 8mm, 5mm and 3mm holes drilled from left to right.* 66

5.7 *Table indicating the thermal images and processed images taken with the Seek Thermal camera at various distances of 750mm, 1750mm, 2750mm, 3750mm, 4750mm of a 60mm diameter anomaly.* 68

5.8 *Table indicating the thermal images and processed images taken with the Seek Thermal camera at various distances of 750mm, 1750mm, 2750mm, 3750mm and 4750mm of a 40mm diameter anomaly.* 70

5.9 *Table indicating the thermal images and processed images taken with the Seek Thermal camera at various distances of 750mm, 1750mm, 2750mm, 3750mm and 4750mm of a 30mm diameter anomaly.* 72

5.10 *Table indicating the thermal images and processed images taken with the Seek Thermal camera at various distances of 750mm, 1750mm, 2750mm, 3750mm and 4750mm of a 20mm diameter anomaly.* 74

5.11 *Table indicating the thermal images and processed images taken with the Seek Thermal camera at various distances of 750mm, 1750mm, 2750mm, 3750mm and 4750mm of a 10mm diameter anomaly.* 75

5.12 *Table indicating the results from the Area Test from the images in Table 5.7 taken with the Seek Thermal camera at various distances of 750mm, 1750mm, 2750mm, 3750mm and 4750mm of a 60mm diameter anomaly.* . 77

5.13 *Table indicating the results from the Area Test from the images in Table 5.8 taken with the Seek Thermal camera at various distances of 750mm, 1750mm, 2750mm, 3750mm and 4750mm of a 40mm diameter anomaly.* . 77

5.14 *Table indicating the results from the Area Test from the images in Table 5.9 taken with the Seek Thermal camera at various distances of 750mm, 1750mm, 2750mm, 3750mm and 4750mm of a 30mm diameter anomaly.* . 78

5.15 *Table indicating the results from the Area Test from the images in Table 5.10 taken with the Seek Thermal camera at various distances of 750mm, 1750mm, 2750mm, 3750mm and 4750mm of a 20mm diameter anomaly.* . 78

5.16 *Table indicating the results from the Area Test from the images in Table 5.11 taken with the Seek Thermal camera at various distances of 750mm, 1750mm, 2750mm, 3750mm and 4750mm of a 10mm diameter anomaly.* . 78

5.17 *Table indicating the results of the temperature calculation of the walls of 4 buildings on the University of Cape Town Upper Campus. The New Engineering Building, The Snape Building, the Mathematics building and the RW James building.* 94

5.18 *Table indicating the thermal images and processed images taken with the Seek Thermal camera at various distances of 750mm, 1750mm, 2750mm of a 60mm diameter anomaly after optimization has occurred.* 100

5.19 *Table indicating the thermal images and processed images taken with the Seek Thermal camera at various distances of 750mm, 1750mm, 2750mm of a 40mm diameter anomaly after optimization has occurred.* 101

5.20 *Table indicating the thermal images and processed images taken with the Seek Thermal camera at various distances of 750mm, 1750mm, 2750mm of a 30mm diameter anomaly after optimization has occurred.* 102

5.21 *Table indicating the thermal images and processed images taken with the Seek Thermal camera at various distances of 750mm, 1750mm, 2750mm of a 10mm diameter anomaly after optimization has occurred.* 104

5.22 *Table indicating the results from the Automatic Segmentation experiments from the images in Table 5.18 taken with the Seek Thermal camera at various distances of 750mm, 1750mm, 2750mm of a 60mm diameter anomaly.* 105

5.23 *Table indicating the results from the Automatic Segmentation experiment from the images in Table 5.19 taken with the Seek Thermal camera at various distances of 750mm, 1750mm, 2750mm of a 40mm diameter anomaly.* 105

5.24 *Table indicating the results from the Automatic Segmentation experiment from the images in Table 5.20 taken with the Seek Thermal camera at various distances of 750mm, 1750mm, 2750mm of a 30mm diameter anomaly.* 105

5.25 *Table indicating the results from the Automatic Segmentation experiment from the images in Table 5.21 taken with the Seek Thermal camera at various distances of 750mm, 1750mm, 2750mm of a 10mm diameter anomaly.* 106

5.26 *Table indicating the flight procedures used for the final drone flight test on the Mathematics Building at the University of Cape Town as described by the protocol developed by the University of Twente.* 109

6.1 *Table showing the comparison between three IR-drone setups, namely the Seek Thermal and AR Parrot, The Mavic Enterprise 2 Dual and the Inspire 1 - Zenmuse XT* 122

Chapter 1

Introduction

1.1 Background to the Study

Nearly a third of global final energy consumption [1] and emissions [2] can be attributed to the built environment. At the same time, the building construction sector accounts for 10% of global GDP and provides employment to over 100 million workers [3]. With growing concerns for a looming energy crisis, climate change, and the need for moving towards a sustainable future, the issue of optimal energy use in buildings is an area of considerable concern and extensive investigations.

For bringing about sustained improvements to building energy consumption, building performance standards and labelling of buildings have become the norm across most countries [4]. Effective implementation of such standards during design and operation have been shown to appropriately aid the goals of energy conservation, achieve cost savings for the end users, and reduce emissions [1, 5].

A building's envelope, both transparent and opaque, modulates its interaction with the outdoor environment, and helps in maintaining liveable indoor conditions. About a third of building energy use is directed towards indoor heating and cooling needs [6]. The envelope thus plays an essential role in buildings' overall energy performance and has dedicated portions of building energy codes guiding selection of materials, effective insulation, and performance in-use [7, 6]. The building envelope, which includes the walls, windows, roof, and foundation, forms the primary thermal barrier between the interior and exterior environments. With envelope technologies accounting for approximately 30% of the primary energy consumed in residential and commercial buildings, it plays a key role in determining levels of comfort, natural lighting, ventilation, and how much energy

is required to heat and cool a building [8].

However, in-use buildings are prone to diverge from their predicted performance [9]. Ensuring that they do not, to undertake appropriate and timely maintenance activities, and to prove in-use compliance to building energy codes, regular inspections are needed, including that of the building envelope. Such inspections can become prohibitively costly in terms of manpower and the analytical resources required, especially considering the expanse of a building's envelope.

As code compliance becomes increasingly important for buildings, there is a consistent demand for means that can support building inspection and reduce the required time and cost. To this end, thermal infra-red (IR) inspection of buildings has been proposed as a useful tool. IR imaging can provide a quick picture of the envelope's temperature profile and as such, help detect damaged insulation, thermal bridges, air leakage, and moisture entrainment. The process is non-destructive, non-contact, and can quickly inspect a significant area. It does not project any radiation on to the buildings and only senses what the buildings themselves radiate. Even greater versatility can be achieved with IR imaging system mounted on Unmanned Aerial Vehicles (UAVs)with a particular focus on roofs and high rise walls. The effectiveness of detection of anomalies remains dependent on the quality of the imaging system. Systems with high quality imaging sensors remain prohibitively costly to be adopted at a much wider scale. The use of infrared thermography in investigating the built environment got a new boost when(UAVs) were brought into the domain. As studies have shown, IR cameras may be successfully integrated with UAVs to survey buildings and produce relevant output regarding their performance [10].

1.2 Objectives of this Study

1.2.1 Problems to be Investigated

This project will take an in depth look at the use of a low cost thermal camera for the purpose of surveying. Firstly we will look at the use of the thermal camera as a means of temperature measurement. Secondly, we try to understand the limitations of the camera via experimental testing. In addition, we also use the thermal images to calculate areas of anomalies detected after image processing has been completed. We also focus on the use of the thermal camera for surveying purposes. Lastly, the flight of a low cost drone is investigated for the purpose of surveying a building.

1.2.2 Purpose of the Study

The purpose of this study is to:

- Develop a possible low cost UAV with attached thermal camera that can be used to survey buildings for construction, maintenance and efficiency purposes.
- Understand the limitations of the chosen thermal camera.
- Develop an algorithm that can calculate the average thermal temperature of the wall of a building.
- Develop an algorithm that can be used to detect a thermal anomaly and indicate the size of the said anomaly.
- Compare the performance of an expensive thermal camera (over R25 000) and inexpensive thermal camera (under R5 000).
- Determine if a low cost UAV can be used for the purpose of surveying with an attached thermal camera.

1.3 Scope and Limitations

The scope of this project is to focus mainly on a prototype of a UAV with an attached IR camera that can be used for the purpose of surveying. The project will contain an in depth look at the use of a camera for temperature readings as well as limitations of the camera. As a scope, the tests have been conducted using a Seek Thermal Compact and a Testo 882 Thermal Imager. Thus the readings attained will not be true for other thermal cameras.

Time is always a limitation in any project. Due to the fact of a poor postal Service in South Africa, the time for experimental trials to take place was severely limited. The type of thermal camera and drone available to the local consumer was also limited due to strict export regulations in the supplier country, hence the chosen thermal camera and drone were not necessarily the ideal chosen choice.

Due to the fact that the tests depend on temperature, the weather was also a limiting factor. The drone could not be flown in rainy or windy weather, this did limit the time for tests. In addition, the IR images needed to be taken a specific time of day due to temperature interference from the weather. Due to the fact that the reflection of the sun skewed some results, most of the images for this project were taken at night or the early morning.

The funds available for this project were also limited. The project needed to be completed within a R10 000 budget, which is not trivial given the highly fluctuating exchange rates in South Africa.

1.4 Plan of Development

1.4.1 Literature Review

The project first begins with the literature review that explains the current use of UAV's and thermal cameras in the construction industry.The literature review also explains the basics of imagery, thermography as well as provides a brief background on IR sensors.

1.4.2 Requirement Analysis

Chapter 3 contains a user requirement document which outlines the requirements for the project as well as the ATP's which will later be treated as the experiments for the project.

1.4.3 Engineering Designs

Chapter 4 focuses on the engineering design of the project which firstly looks at a conceptual design for the prototype. Secondly a selection of the IR camera will be discussed as well as the UAV to be used. Lastly this chapter includes a comparison and then selection for the algorithms to be used in the experiments.

1.4.4 Experiment Designs

Chapter 5 discusses the experiments used as ATP's of this project: Experiment 1 discusses the use of an IR camera as a means for temperature reading. Experiment 2 discusses the comparison between an expensive and inexpensive thermal camera and whether or not image processing can be used to attain the results of the expensive thermal camera using the inexpensive one. Experiment 3 indicates the use of an algorithm to detect an anomaly and calculate it's size. Experiment 4 is broken into two parts namely "a" and "b". Part "a" looks at the use of thermal imaging for surveying of new and old structure and Part

"b" looks at the use of an algorithm to indicate the weighted average temperature of the wall of a building as well as providing a electrical model of the temperature flow through a wall. Experiment 5 focuses on the development of an algorithm for automatic image segmentation and Experiment 6 is the last test and focuses on the use of a low cost UAV for the purpose of surveying.

1.4.5 Conclusions and Recommendations

This chapter explains the reasons for the results and occurrences in the project. The chapter will also share a few thoughts on lessons learnt whilst carrying out the experiments and how to better execute them in future if need be.

1.4.6 Future Work

This chapter provides a more forward thinking approach with regards to the technology being applied to the constructions and surveying industry.

Chapter 2

Literature Review

2.1 Infra-Red Radiation

British astronomer William Herschel discovered infra-red light in 1800, according to NASA. In an experiment to measure the difference in temperature between the colours in the visible spectrum, he placed thermometers in the path of light within each colour of the visible spectrum. He observed an increase in temperature from blue to red, including an even warmer temperature measurement just beyond the red end of the visible spectrum[11].

Infra-red radiation is a type of electromagnetic radiation, as are radio waves, ultraviolet radiation, X-rays and microwaves. Infra-red (IR) light is the part of the EM spectrum that people encounter most in everyday life, although much of it goes unnoticed. It is invisible to human eyes, but people can feel it as heat[11].

Everything with a temperature above about 5 degrees Kelvin (minus 268 degrees Celsius) emits IR radiation. The sun gives off half of its total energy as IR, and much of its visible light is absorbed and re-emitted as IR, according to the University of Tennessee[11].

Electromagnetic (EM) radiation is transmitted in waves or particles at different wavelengths and frequencies. This broad range of wavelengths is known as the electromagnetic spectrum. The spectrum is generally divided into seven regions in order of decreasing wavelength and increasing energy and frequency. The common designations are radio waves, microwaves, infra-red (IR), visible light, ultraviolet (UV), X-rays and gamma-rays[11].

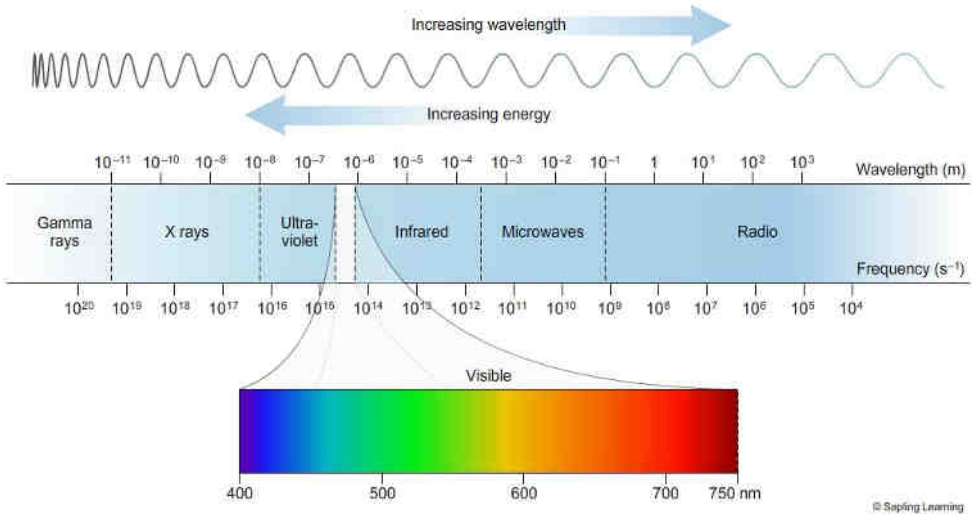

Figure 2.1: *The electromagnetic spectrum with indication of wavelength and frequencies* [12].

Infra-red waves are longer than those of visible light, just beyond the red end of the visible spectrum. Infra-red (IR) falls in the range of the (EM) spectrum between microwaves and visible light. It has frequencies from about 300 GHz up to about 400 THz and wavelengths of about 1 millimeter to 700 nanometers, although these values are not definitive[11].

2.2 Thermography

It has been found that modern lifestyle demands the average human to spend roughly 20hrs per day indoor [13]. As a result, there has been sudden influx in research into thermal comfort within the living space.

Since the 1960s formal bodies have been looking into providing a standard for the minimum requirements for acceptable thermal indoor environments [14]. ASHRAE, the American Society of Heating, Refrigeration and Air-Conditioning Engineers, is one such body. ASHRAE Standard 55 is a standard that establishes the ranges of indoor environmental conditions that are acceptable to achieve thermal comfort for occupants."The purpose of the standard is to specify the combinations of indoor thermal environmental factors and personal factors that will produce thermal environmental conditions acceptable to a majority of the occupants within the space"[14]. ASHRAE uses essentially two methods methods to evaluate thermal comfort, the first is based on human heat balance and the other, adaptive thermal comfort. These methods are practised via a multitude of techniques , they are:

- **Graphic comfort zone method.**
  This method utilizes factors such as operative temperatures and humidity at which thermal comfort can be reached. It is based on the Predicted Mean Vote model, as seen in Figure 2.2, which makes use of heat-balancing equations about skin temperature to define comfort. [15].
- **Analytical comfort zone method.**
  This method is also based on the PMV model. It makes use of different Thermal Comfort Tools to evaluate thermal comfort and takes factors such as air speed, metabolic rate, and clothing insulation in to account.
- **Elevated air speed.**
  This approach sets provisions for the increasing of upper air temperature limits at air speeds above 0.2m/s [14].
- **Local thermal discomfort.**
  This approach takes into account the radiant temperature asymmetry between ceiling and floor as well as air and walls. It states that air speeds due to HVAC systems must be 0.15m/s or below. The vertical air temperature difference between ankle and head should be limited to 3 °C for seated occupants and 4 °C for standing occupants [14].
- **Temperature variations with time.**
  This section applies to occupants that do not have control of indoor thermal environments. It states that the temperature should not fluctuate more than 1.1 °C within 15 minutes, nor more than 2.2 °C within 1 hour.
- **Acceptable thermal conditions in occupant-controlled naturally conditioned spaces.**
  This method is used for buildings that do not contain mechanical cooling. The standard provides a graph of acceptable indoor temperature limits at mean outdoor temperatures.

Although the above methods and techniques have been put in place, there have been many attempts to accurately measure the thermal comfort levels within a building, however, most of the available methods require a rather invasive approach in the form of thermocouples or an expensive one with the use of other instruments [16, 17]. Pavlin *et al* have suggested that thermographic imaging has been shown to be a reliable method for a real-time and non-invasive monitoring of local cutaneous temperature over the body's surface [18, 19, 20]. This method of thermography has been used to detect the temperature of the forehead as it has been described to be a good indicator of comfort of the individual [13].

Thermal comfort spreads much wider, leaving the individual and focusing on the surrounding environment as well. This together with HVAC systems has resulted in a large

Value	Sensation
-3	Cold
-2	Cool
-1	Slightly cool
0	Neutral
1	Slightly warm
2	Warm
3	Hot

Figure 2.2: *The PMV sensation scale* [15].

focus being drawn to thermal comfort being incorporated in building design. One such example of this is explained as part of the UBC Sustainability Scholars program of July 20th 2016 [21]. The report focused on the use of thermal cameras to promote energy efficiency in buildings. It was found that thermography can be used to calculate energy efficiency of structural envelopes and aid in building inspections and bridge health monitoring. It also proves highly useful as a form of non destructive testing.

Energy Efficiency:

The envelope of the building is the part of the building that separates the, typically air-conditioned, indoors from the outdoors. The quality of the envelope is directly proportional to the energy efficiency of the building. Given that in cold climates, approximately 50% of the building's energy is used by HVAC systems and over 60% in the residential sub-sector in cold-climate countries. Overall, buildings are responsible for more than one-third of global energy consumption. While whole-building approaches are ideal, every day building envelope components are upgraded or replaced using technologies that are less efficient than the best options available [22]. The potential for a well-designed envelope is substantial. This in turn leads to a huge saving for building owners as well as environmental benefits [21].

Building Inspections:

Thermal imaging cameras can be used to identify construction problems, design flaws, ageing building materials and other sources of heat loss. They can also be used to indicate the flow of heat which in turn can be used to detect faulty materials. The technology can also be used for the detection of moisture which would usually be naked to the human eye - this can be done by locating areas below the dew point [21].

Bridge health monitoring:

Detecting sub-surface cracks and de-laminations within concrete bridges has been always a challenge for bridge inspectors and transportation authorities. This type of subsurface deterioration can appear either on the bridge deck or girder; however, de-laminated areas underneath the bridge can be more critical as it raises safety issues for passing by traffic. Visual inspection, which is a common practice technique for bridge condition evaluation, is not able to provide enough information of internal defects and deteriorations. Although, recent developments in non-destructive techniques provide bridge inspectors with advanced tools and methods for bridge inspection, most of these methods are either expensive,difficult to apply or require an extensive background in the field in order to interpret.

Subsurface de-laminations and anomalies appear as hot spots on the thermal IR image during the day as they interrupt the heat transfer through the concrete. In this way, de-laminations can be detected before turning to spalls on the bridge. Applying this technology can enhance the current bridge inspection practice as well as providing useful information for maintenance and repair decision making [23].

Vaghefi *et al* suggest the use of IR technology for bridge evaluation. Their paper focuses on the detection of de-laminations in the concrete as well as the deficiency of bridge elements and the detection of chemical staining.

Non-destructive Testing:

Non-destructive testing (NDT) is the process of inspecting, testing, or evaluating materials, components or assemblies for discontinuities, or differences in characteristics without destroying the serviceability of the part or system. In other words, when the inspection or test is completed the part can still be used [24].

NDT is particularly useful on older and antique structures as one can detect anomalies early as well as be non-destructive to the structure. With regards to wooden structures,

by far, one of the most cost effective methods to detect anomalies in the wooden structure is to use percussion with a blunt object. This however, relies on years of experience from the operator when it comes to detecting the anomaly. This form of detection is also slow and relies on many aspects. In addition, the recording and interpretation can also be problematic due to a lack of formal standards [25].

Careful consideration should be applied when using the device due to the simple fact that thermal images can be misinterpreted. The following should always be taken into account when using a thermal camera:

- **Display**
  The "span" is a very important parameter to consider when inspecting the thermal camera's display. The effect can be seen in Figure 2.3. It is advisable to keep the span as narrow as possible so that the thermal image can be accentuated to portray as much detail as possible [21]. The wider the span, the more complementary the colours across the temperature range being displayed, therefore resulting in an image that does not accentuate small differences clearly.

- **Viewing Angle**
  Due to the nature of thermal radiation being either diffuse or specular, the viewing angle is of utmost importance. It is therefore ideal to view the targets at a perpendicular angle from the surface.

- **Emissivity**
  The emissivity of objects are unique to each object. In order for accurate measurements to be given, the emissivity of each object should be known.

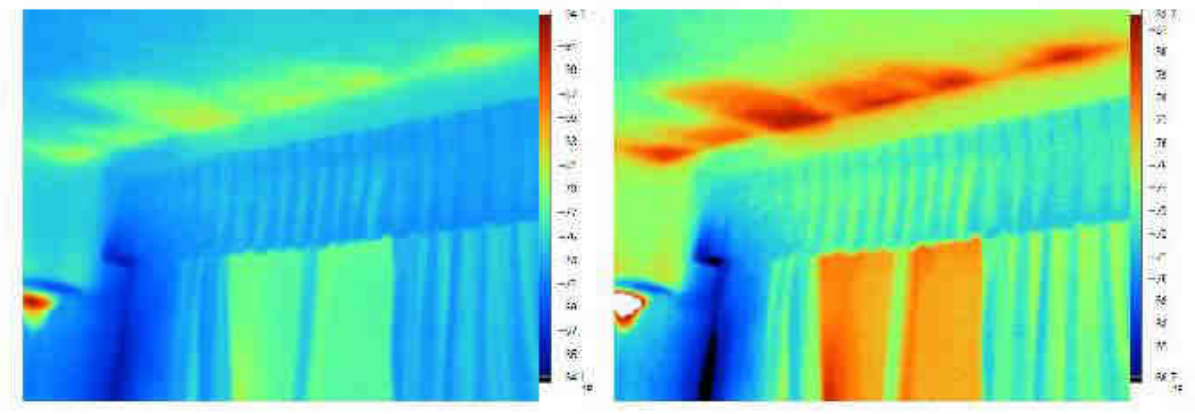

Figure 2.3: *Two thermal images of a room. The picture to the left uses a wide-span whilst that on the right uses a narrow span* [21].

Thermographic cameras detect infra-red radiation directly and convert it to an electrical signal which is then interpreted into an image that represents the radiation intensity. It

is important to note that thermal cameras do not detect heat directly, only radiation, therefore, it is of utmost importance that the following formula is understood:

$$IncidentRadiation = EmittedRadiation + TransmittedRadiation + ReflectedRadiation$$

$$(radiosity) = (emissivity) + (transmissivity) + (reflectivity)$$

- **Radiosity**
  The radiosity of an object is defined as the total radiation leaving an objects surface [21]. The radiosity of an object includes all energy reflected off the surface of the objects surface as well as the energy radiated through the object itself.

- **Emissivity**
  The emissivity of an object is a true indicator of the objects surface temperature [21]. It is defined as the materials efficiency in emitting thermal radiation and is unique to individual materials as seen in Figure 2.4 below. The emissivity of an object indicates the ability of an object to emit radiation in comparison to a black body which is an ideal emitter and absorber of energy. Therefore, if the emissivity is close to 1, then the object is defined as a good emitter and if the closer to 0, then the object is defined as a good retainer of heat. It should also be noted that the surface texture will have a significant impact on emissivity as well with a polished surface having a much lower emissivity than a roughened one [21].

EMISSIVITY

The following table presents the emissivity coefficients for some common materials.

MATERIAL	EMISSIVITY	MATERIAL	EMISSIVITY
Aluminum foil	0.03	Limestone	0.92
Aluminum roofing	0.24	Mortar	0.90
Asphalt	0.88	Nickel, electroplated	0.03
Brass, oxidized	0.60	Nickel, solar absorber	0.05 - 0.11
Brass, polished	0.04	Paints, silver chromatone	0.24
Brick	0.90	Paints, acrylic	0.90
Concrete, rough	0.91	Paints, gloss	0.85
Copper, electroplated	0.03	Paints, epoxy	0.85
Copper, oxidized	0.76	Paper, roofing	0.88 - 0.86
Glass, polished	0.87 - 0.92	Plaster, rough	0.89
Glass, smooth	0.91	Silver, polished	0.02
Granite	0.44	Snow	0.82
Gravel	0.30	Soil	0.94
Ice	0.96 - 0.97	Water	0.90

Figure 2.4: *Table showing the emissivity coefficients of common materials* [21].

- **Angle of Incidence**
  It is important to note that the direction of radiation is dependant on the type of material. While radiation from some materials is concentrated in a single direction, other materials disperse it evenly. Therefore, when emitted radiation is dependant on direction, it is termed "specular" and when it is not dependant on direction, it is termed "diffuse".This important as the thermal appearance of an object will be different depending on the angle from which it is viewed [21].

- **Temperature Differential**
  Due to the flow of energy from a warm body to a cold one, the difference in temperature between the outside or surrounding areas should always be taken into account when targeting an object with a thermal camera.

- **Evaporative Cooling**
  As water evaporates, it draws in heat from its surrounding environment, which in turn reduces the temperature of the substance in contact with the moisture. This will result in the surface appearing cooler due to its evaporation.

- **Thermal bridges**
  Due to the movement of heat from a body with a high temperature to that with a low temperature in order to reach equilibrium, thermal energy generally takes the path of least thermal resistance. These concentrated pathways have significantly different temperatures than their surroundings and are known as "Thermal Bridges". Geometrical thermal bridges are generally found at corners of roofs, walls and floors. Due to the fact that the exterior provides a larger area than the interior, there will appear to be a larger opportunity for heat to escape from the exterior. Generally, geometrical thermal bridges depend on building design and can be managed, but are inevitable. Structural bridges, on the other hand, are as a result of the set-up of building materials and if not managed properly can result in temperatures being lowered beneath the dew point which results in moisture build-up and mould problems. [21]. Structural bridges are generally a result of design faults.

In order to get the best results from thermography, there are many considerations that must be taken into account. These generally have to do with the capabilities of the thermal camera itself. The following was taken from [21]:

- **Detector Resolution**
  A higher resolution allows one to see finer details as well as sharper contrasts. A problem with thermal imaging cameras is that they generally have poor resolutions.

- **Accuracy vs Sensitivity**
  The accuracy of a thermal imaging system is defined as the margin of error of its readings, and is generally expressed as a percentage. This specification should be distinguished from a device's sensitivity, which is the smallest variation in temperature that it can detect. Sensitivity is given as a change in absolute temperature, generally between 0.05 and 0.15°C for most hand held thermal cameras.In general, this is acceptable for surveying purposes.

- **Thermal Range**
  A cameras thermal range describes the maximum and minimum temperatures that it can accurately measure. These vary considerably depending on the model.

The use of thermography has been extended so far as to being employed on Unmanned Arial Vehicles. Recent studies carried out by the East Tennessee State University show that a thermal imaging camera can be successfully attached to the drone to survey the a building and produce positive results regarding energy performance. The study also showed that the dictated Resistance values of building materials does vary over time and in this particular case, have varied far below the recommended ASHRAE values based on assume indoor conditions [10].

Engineers from the University of Twente have even gone to the extent of trying to create a protocol for the for IR-UAV flights to survey building thermography in the construction domain. Figure 2.5 below shows the developed protocol [26]:

1. Plan the initial set-up phase
a. Become acquainted with the *object of research* (e.g. PV-system or the thermal shell of a high rise building)
b. Become acquainted with the national, regional and local *regulations* related to flying UAVs
c. Find a location close to the object of research to *assemble* the UAV so enough space is available
d. Check the *weather* forecasts and the local weather conditions
e. Find a location safe to the pilot, video pilot and any audience to control the UAV (*operation subsystem*)
f. Conduct a short test flight to ensure the *UAV* is operational
2. Outline a safe and secure flight area (as a 3D flight space)
a. To adequately cover the zone of interest around the *object of research*
b. That provides an unobstructed view between the *UAV* and the pilot (*operation subsystem*)
c. That contains no *ancillary* objects that can be impacted with the UAV
d. Consider safety landing locations (*secondary landing spot*) in case the final landing zones cannot be reached
3. Account for requirements to momentarily photos and continuous video collection
a. Decide what camera(-s) and lens(-es) have the proper *specifications* for studying the object of research
b. Consider appropriate camera *angles* to capture elements of interest in the *object of research*
c. Determine *distances* between the camera(-s) and elements of interest in the object of research
d. Account for the rotation, horizontal and vertical speed of the UAV in flight (*drone flight dynamics*)
4. For each element of interest within the object of research
a. Construct a flight path that takes into account *drone flight dynamics* or in other words the speed
b. Connect flight paths moving the UAV around *ancillary objects*, while ensuring a proper *camera distance/angle*
c. Check the length of the (total) flight path(-s) in relation to the capacity of the *battery* of the UAV

Figure 2.5: *Table indicating the developed protocol for IR-UAV flights to survey building thermography in the construction domain* [21].

2.3 Thermal cameras and IR sensors

Thermal cameras are cameras that create an image of temperature distribution or thermal radiation. They are different from night vision cameras in that while night vision cameras take and use any surrounding and available light, such as moonlight and street light, to brighten up an image, a thermal camera utilizes the infra-red radiation being emitted from an object to create an image. In order to understand how a thermal image is created, it is of vital importance that one understands the sensors behind it all. The general image creation process can be summarized into the block diagram below:

Figure 2.6: *General block diagram depicting formation of IR image.*

The above block diagram is summarised as follows:

The thermal scene depicts all objects above absolute zero that emit infra-red radiation. The IR is focused through the lens of the camera, which is generally made of a Germanium compound since glass is not a good transmitter of IR. The IR is then focused on an array

of sensors that result in the creation of the resolution of the image. The more sensors are present, the higher the resolution. The sensors then create an impulse or voltage that is dependant on intensity and is taken in by the signal processor. The signal processor then converts the impulses into data that creates and image via intensities, represented in a 2D array, that can be seen on the display.

IR cameras can be categorized as follows:

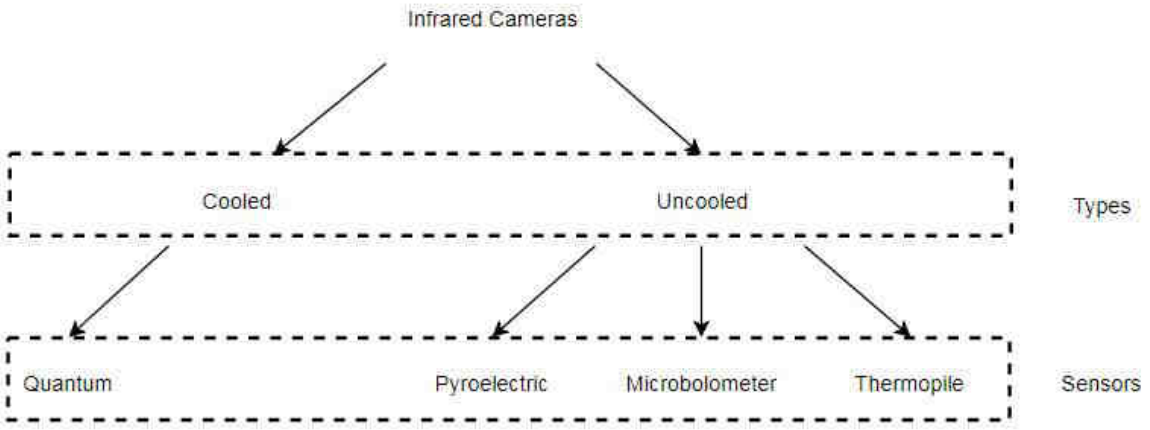

Figure 2.7: *General representation of IR devices.*

Cooled vs Uncooled

A cooled thermal camera's imaging sensor is integrated with a cryocooler. The cryocooler lowers the sensor temperature. This drop in sensor temperature is necessary to lessen thermally induced noise to a level below that of the signal from the scene being imaged. Cooled thermal cameras are more sensitive to small differences in scene temperature than are uncooled cameras, making cooled cameras more suitable for extremely long-range imaging in low-contrast scenes. In addition, the lens of uncooled thermal cameras become large, bulky and expensive when viewing areas in the km range, but, for short range viewing, cooled thermal cameras tend to be much more expensive [27].

Quantum Thermal Cameras

In materials used for quantum detectors, at room temperature there are electrons at different energy levels. Some electrons have sufficient thermal energy that they are in the conduction band, meaning the electrons there are free to move and the material can conduct an electrical current. Most of the electrons, however, are found in the valence band, where they do not carry any current because they cannot move freely.

When the material is cooled to a low enough temperature, which varies with the cho-

sen material, the thermal energy of the electrons may be so low that there are none in the conduction band. Hence the material cannot carry any current. When these materials are exposed to incident photons, and the photons have sufficient energy, this energy can stimulate an electron in the valence band, causing it to move up into the conduction band. Thus the material (the detector) can carry a photo-current, which is proportional to the intensity of the incident radiation [28].

Pyro-electric Sensors

These sensors are used primarily for detecting motion, but use IR to do so. The PIR (Pyroelectric Infra-red Radiation) sensor itself has two slots in it, each slot is made of a special material that is sensitive to IR. The lens used here is not really doing much and so we see that the two slots can 'see' out past some distance (basically the sensitivity of the sensor). When the sensor is idle, both slots detect the same amount of IR, the ambient amount radiated from the room or walls or outdoors. When a warm body like a human or animal passes by, it first intercepts one half of the PIR sensor, which causes a positive differential change between the two halves. When the warm body leaves the sensing area, the reverse happens, whereby the sensor generates a negative differential change. These change pulses are what is detected [29].

As the sensor stays in constant view of the object, the static voltage that has developed across the structure tends to decline, for this reason, the signal needs to be refreshed at a constant rate.

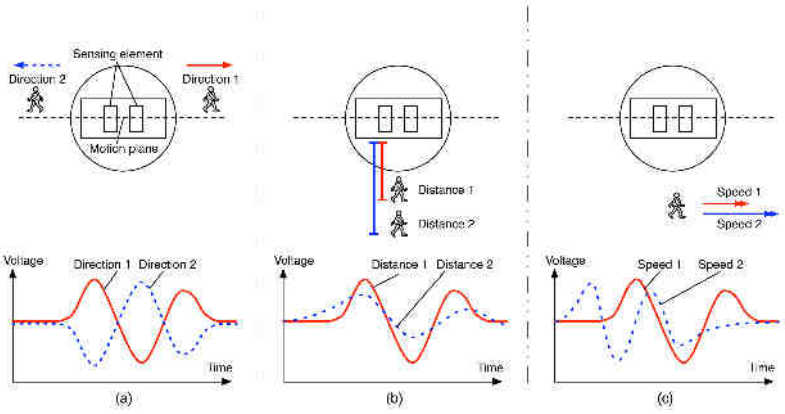

Figure 2.8: *The created voltage output of a pyroelectric sensor.* [30].

As seen in Figure 2.8 above, in all cases, a,b and c a change in voltage is created when the shown scenario takes place. This is then converted into a readable measurement.

Thermopile Sensors

A thermopile refers to a set of thermocouple sensors arranged, either in series or parallel, for measuring small quantities of radiant heat. The principle of operation for this sensor is via the Seebeck Effect:

When heat is applied to one of the junctions formed by two conductors or semiconductors, heated electrons flow toward the cooler one. If the pair is connected through an electrical circuit, direct current (DC) flows through that circuit.The voltages produced by Seebeck effect are small, usually only a few microvolts (millionths of a volt) per kelvin of temperature difference at the junction. If the temperature difference is large enough, some Seebeck-effect devices can produce a few millivolts (thousandths of a volt). Numerous such devices can be connected in series to increase the output voltage or in parallel to increase the maximum deliverable current. Large arrays of Seebeck-effect devices can provide useful, small-scale electrical power if a large temperature difference is maintained across the junctions [31].

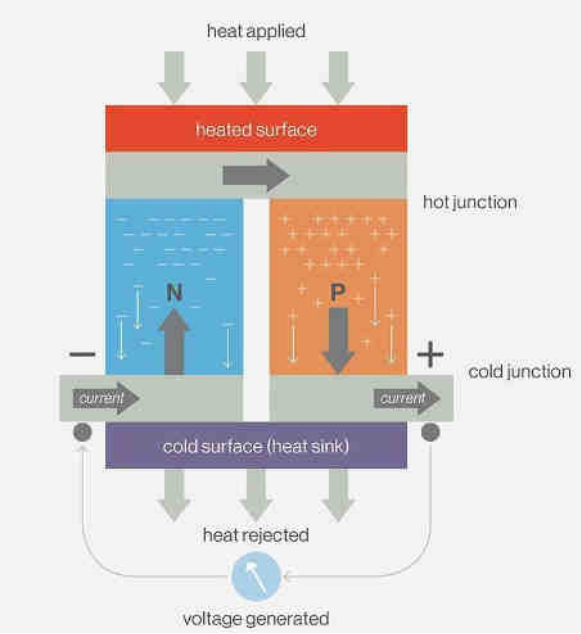

Figure 2.9: *The workings of the Seebeck Effect.* [32].

Microbolometers

Bolometers are small infrared sensors that do not require cooling. When IR light enters the bolometer, the bolometer resistance heats up, causing a change in its resistance. This change is converted to a voltage for a readout. Therefore, all bolometers come with a readout integrated circuit (ROIC) [31].

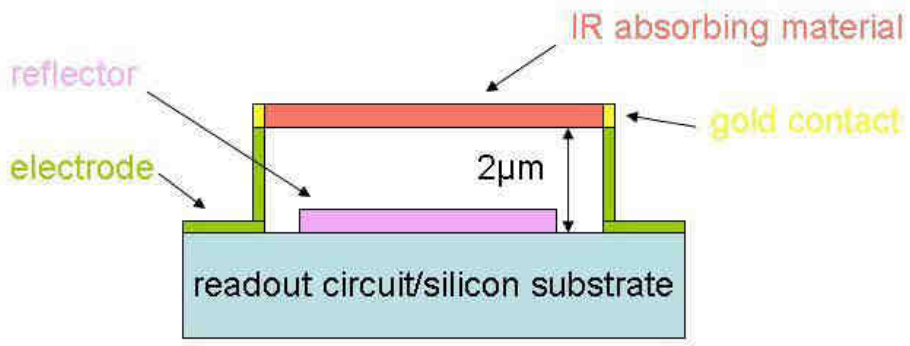

Figure 2.10: *The general layout of a microbolometer* [33].

2.4 Digital images

Digital images are made of picture elements called pixels. Typically, pixels are organized in an ordered rectangular array. The size of an image is determined by the dimensions of this pixel array. The image width is the number of columns, and the image height is the number of rows in the array. Thus the pixel array is a matrix of M columns x N rows and is usually referred to as a bitmap [34].

Image size is not to be confused with the size of the real world representation of an image. Image size specifically describes the number of pixels within a digital image. The real world representation of a digital image requires one additional factor called resolution. Resolution is the spatial scale of the image pixels. For example, an image of 3300 x 2550 pixels with a resolution of 300 pixels per inch (ppi) would be a real world image size of 11" x 8.5" [34].

Having defined the number of pixels, M x N, only provides a rectangular shape for the image. One more parameter, intensity, is needed to truly define an image. Each pixel has its own intensity value, or brightness. If all the pixels have the same value, the image will be a uniform shade; all black, white, grey, or some other shade. It is in the type of intensity used for each pixel that image types vary. Black and white images only have intensity from the darkest grey (black) to lightest grey (white). Colour images, on the other hand, have intensity from the darkest and lightest of three different colours, Red, Green, and Blue. The various mixtures of these colour intensities produces a colour image. Thus the two most basic types of digital images, B and W and Colour, are known as grey-scale and RGB images. In addition to the intensity type of each pixel, the range of intensity values also varies [34].

Intensity values in digital images are defined by bits, hence the name, bitmap. A bit is binary and only has two possible values, 0 or 1. An 8-bit intensity range has 256 possible values, 0 to 255. For a 1-bit, or binary, image, $2^1 = 2$ possible values and for an

8-bit image, $2^8 = 256$ possible values. The standard digital photo uses an 8-bit range of values; RGB images use 8-bit intensity ranges for each colour and B and W images have a single 8-bit intensity range. Since RGB images contain 3 x 8-bit intensities they are also referred to as 24-bit colour images [34].

Each pixel in a bitmap contains certain information, usually interpreted as colour information. The information content is always the same for all the pixels in a particular bitmap. The amount of colour information could be whatever the application requires but there are some standards, the main ones are described below:

1 bit (black and white)

This is the smallest possible information content that can be held for each pixel. The resulting bitmap is referred to as monochrome or black and white. The pixels with a 0 are referred to as black, pixels with a 1 are referred to as white. Note that while only two states are possible they could be interpreted as any two colours, 0 is mapped to one colour, 1 is mapped to another colour.

8 bit greys

In this case each pixel takes 1 byte (8 bits) of storage resulting in 256 different states. If these states are mapped onto a ramp of greys from black to white the bitmap is refereed to as a grey-scale image. By convention 0 is normally black and 255 white. The grey levels are the numbers in between, for example, in a linear scale 127 would be a 50% grey level. Figure 2.11 below shows the scale of grey represented by 8 bits.

Figure 2.11: *Indication of the levels of grey in an 8-bit scale* [34].

24 bit RGB

There are 8 bits allocated to each red, green, and blue component. In each component the value of 0 refers to no contribution of that colour, 255 refers to fully saturated contribution of that colour. Since each component has 256 different states there are a total of 16777216 possible colours. This ideology can be seen in Figure 2.12 below.

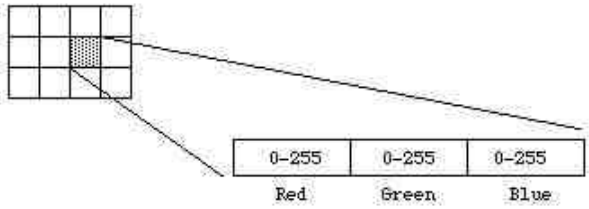

Figure 2.12: *Indication of the 24-bit RGB ideology.* [34].

2.5 Image Segmentation Techniques

There are a multiple of image segmentation techniques available which help one to analyse and extract particular information from digital images. These methods can also help to improve the quality of images.

Image segmentation refers to the partitioning of an image into particular parts that are of interest to an application because of their similarities in features or properties. The main applications of segmentation are: Medical imaging, Content-based image retrieval and automatic control systems among others. Image segmentation can be classified into three basic approaches: [35].

Structural Segmentation Techniques

This technique is based upon knowledge about the structure of the image for example, where certain pixels of interest may be located in an image. [35].

Stochastic Segmentation Techniques

This technique is based on the value of pixels within the image or more specifically, the intensity values of each pixel within an image. [35].

Hybrid Techniques

This technique makes use of both structural and stochastic techniques [35].

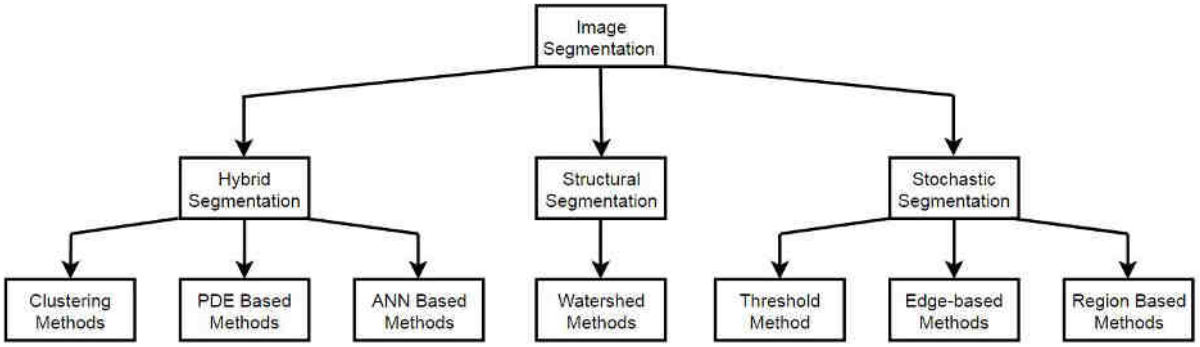

Figure 2.13: *Image Segmentation Techniques Adapted from:* [35].

Figure 2.13 above indicates 7 methods used for image segmentation where PDE refers to Partial Differential Equations and ANN, Artificial Neural Networks. Among the methods available, this paper will focus on 4 main methods used to extrapolate data, namely:

- Histogram Optimization using Global Thresholding
- Local or Adaptive Thresholding
- Edge-based Segmentation
- Region-based Segmentation using the Canny edge detector

Histogram Optimization

Histogram-based image segmentation is one of the simplest and most often used segmentation techniques. It uses the histogram to display the number of pixels of specific intensities, hence, this technique works best when used on grey-scaled images. In a simple image there are two entities, that one would be interested in: the background and the object. The background is generally one grey level and occupies most of the image. Therefore, its grey level is a large peak in the histogram. The object or subject of the image is another grey level, and its grey level is another, smaller peak in the histogram [36].

In addition to histogram-based segmentation, the technique of thresholding is used in order to display and discard certain information on an image. This is done by placing a particular threshold value on the image histogram and setting values above the threshold to either a 1 or a 0 and values below that threshold to the opposite. This will result in in the features of interest being visible and those of no interest being set to a default colour, usually white.

In Figure 2.14 above, the red line indicates the threshold. All values above the threshold were decided to be the background of the image as the background will generally consist

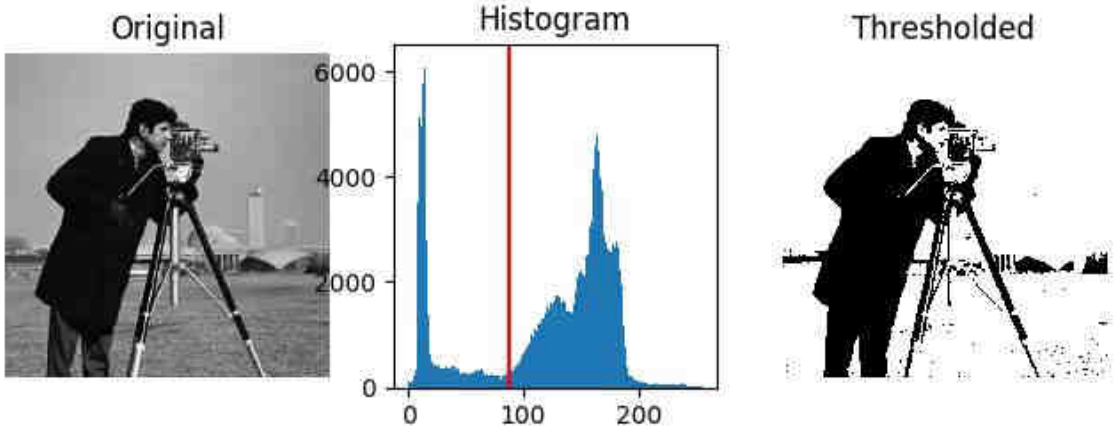

Figure 2.14: *The process of histogram - based segmentation via thresholding* [37].

of more pixels as it will take up more space on the image. In addition, the background will have a wider range of intensities than the foreground of the image which, in the case above, is the photographer. Thus, the background was set to be a binary 0 and the foreground was set to be a binary 1.

The type of thresholding above is referred to as Simple or Global thresholding - whilst it is rather easy to implement, the process of selecting the thresehold is rather primitive and as seen in the threshold part of Figure 2.14 above, does not completely clear the background due to parts of the background having high intensities. There are other thresholding methods which try to handle this problem, they are referred to as local thresholds or adaptive thresholds, bimodal histograms and minimum thresholds [38].

In general, a picture will have two parts as explained above: the background and foreground. The Bimodal histogram method will continuously smooth out the histogram of an image until there are two peaks, these will usually indicate the foreground and background of this image. A threshold will then be placed in between these peaks - this will eliminate either the background or foreground, depending on what is of interest to the user. The threshold can be calculated using the mean of the intensities or via Otsu's Method by maximizing the variance between two classes of pixels, which are separated by the threshold. Equivalently, this threshold minimizes the intra-class variance [37].

Local thresholding refers to the calculating of thresholds in a characteristic region, around a pixel. Each threshold value is the weighted mean of the local neighbourhood subtract a specific value [37].

Edge-based Segmentation

For edge detection the Canny edge detector is used. This detector has 5 steps that are used in order for it's implementation:

1. Apply a Gaussian Filter to blur and take out noise.
2. Find the intensity gradients of the image by applying a filter.
3. Apply non-maximum suppression.
4. Apply a double threshold
5. Track edges by hysteresis.

Gaussian Filter

For the Gaussian Filter, the following formula is applied to create a Gaussian kernel:

$$G(x,y) = \frac{1}{2\pi\sigma^2} e^{-} \frac{x^2+y^2}{2\sigma^2} \tag{2.1}$$

Where:

x - Value of the matrix row

y - Value of the matrix column

σ^2 - The Variance

The Gaussian kernel is then convoluted with the original image in order to blur it and take away noise and soft edges whilst still preserving big edges. It should be noted that the standard deviation, which is given as σ is chosen. In general, the larger the value of σ, the wider the Gaussian bell becomes and thus the more blur the image receives [39] [40].

Finding the Intensity Gradients

In order to find the intensity gradients, an edge detection filter is usually used. In this thesis, the Sobel filter will be used. This filter emphasizes edges from a grey-scale image in both the x and y directions and then combines them into one image. In order to apply these filters, one must use the filter kernels shown below:

$$G_m = \begin{pmatrix} -1 & 0 & +1 \\ -2 & 0 & +2 \\ -1 & 0 & +1 \end{pmatrix} * A \quad G_n = \begin{pmatrix} -1 & -2 & -1 \\ 0 & 0 & 0 \\ +1 & +2 & +1 \end{pmatrix} * A$$

Where A represents the original image.

The two filtered images are then combined to create an edge-defined image by applying the formula below:

$$M(x, y) = \sqrt{G_x^2 + G_y^2} \tag{2.2}$$

The angle of the specific edge can also be calculated via the following formula:

$$\theta(x, y) = \arctan(\frac{G_y}{G_x}) \tag{2.3}$$

Applying non-maximum Suppression

Non-maximum suppression is an edge thinning technique. This step is usually done in code using if statements whilst iterating through each pixel in the matrix of the image. A simple check is done to see the strength of the current pixel in relation to the neighbouring pixels in the θ direction. If the current value is stronger than that of the compared pixel, it's value will be preserved, if not, it will be set to 0.

Applying a double threshold

After application of non-maximum suppression, remaining edge pixels provide a more accurate representation of real edges in an image. However, some edge pixels that remain are caused by noise and colour variation. In order to account for this, it is essential to filter out edge pixels with a weak gradient value and preserve edge pixels with a high gradient value. This is accomplished by selecting high and low threshold values. If an edge pixel's gradient value is higher than the high threshold value, it is marked as a strong edge pixel. If an edge pixel's gradient value is smaller than the high threshold value and larger than the low threshold value, it is marked as a weak edge pixel. If an edge pixel's value is smaller than the low threshold value, it will be suppressed. The two threshold values are empirically determined and their definition will depend on the content of a given input image[41].

Edge-Tracking by Hysteresis

Sometimes weak edge pixels as a result of colour variations pass through the filters. In order to remove these, it is assumed that weak edge pixels are connected to strong edge pixels whilst noise responses are unconnected. To track the strong edge pixels Blob analysis is used[41]. This involves iterating through the pixels and comparing neighbours to see for their intensities. These are then grouped according to their intensities and weak groups removed.

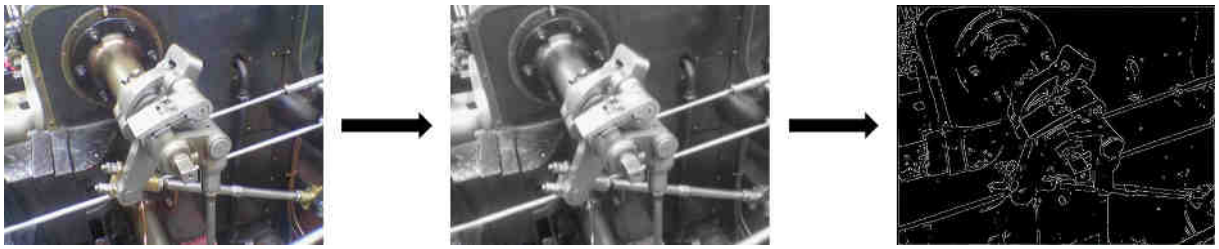

Figure 2.15: *The process of Canny filtering used for Edge detection* [41].

Figure 2.15 above shows the basic process of canny filtering with the first picture indicating the original colour image, the second picture indicating the grey-scaled Gaussian blurred image and the last picture indicating the edge defined image.

After the edge-tracking is complete, any holes in the image are filled using a mathematical morphological function; in this case, binary dilation, which will fill edges of the target object that one is interested in. Small spurious objects are then later removed by applying a minimum size for valid objects [42].

Region-based Segmentation

For region based segmentation, generally, step 1 and 2 from edge-based segmentation are applied. The Sobel operator is used to determine the gradient of the image. The next step is to apply markers to the foreground and background of the image. Lastly, in this case, a watershed transform is applied to the image to fill the regions on the elevation map that were created by the gradients of the image.

The watershed transform treats the image that it is applied to as a topographical map with the brightness of each point represented as a height, it then tries to identify the ridge lines that run along the top of these basins and by doing that, segments the image. This idea is understood by the images below:

Figure 2.16, shows a basic optical image of 4 dots with the 2 in the middle, slightly overlapping. When the watershed transform is applied, these dots are viewed as valleys

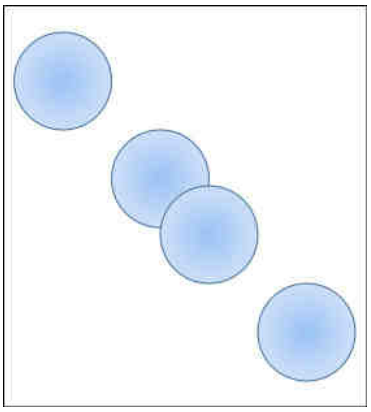

Figure 2.16: *A basic optical image used to explain the watershed algorithm.*

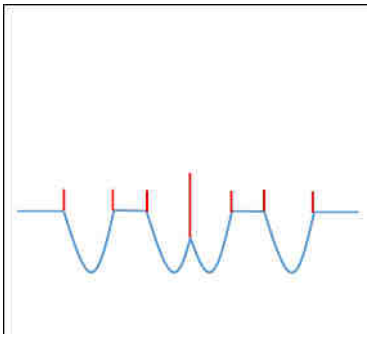

Figure 2.17: *The side view of the optical image above if transformed to basins.*

or basins as seen in blue in Figure 2.17. If one were to fill water in these basins, when taking the middle 2, the water would reach a stage where if one drop more was applied, it would flow over into the third basin from the left, thus a dam wall or ridge is built. The ridge will run around the basin and will be used to cluster the pixels of a region in the image whilst the basin/region is filled [43].The algorithm is implemented in 4 parts [44]:

1. Markers will be chosen where the flooding will start and will be given a different label.
2. Neighbouring pixels of each marked are will be inserted into a priority queue with a priority level corresponding to the gradient magnitude of the pixel.
3. The pixel with the lowest priority is extracted from the queue. If the neighbours of the extracted pixel that have already been labelled all have the same label, then the pixel is labelled with their label. All non-marked neighbours that are not yet in the priority queue are put into the priority queue.
4. Redo step 3 until the priority queue is empty.

The non-labelled pixels then become the watershed lines.

Chapter 3

Requirement Analysis

This chapter includes a basic description of the system to be used as a prototype for the IR camera and UAV set-up. It then goes on to give a Requirement Baseline Section which is describes the basic, high-level requirements for the project. The Functional, Performance and Design Requirements are then formally listed. The Acceptance Test Procedures (ATP's) are then discussed and related to the requirements. In addition, the constraints for this project are listed.

The main requirement of this work is to create a device that can remotely survey a building of any shape and size by detecting anomalies in it's structure from which thermal energy can escape, using Infra-Red thermography.

As a minimum requirement, the IR-UAV should be able to survey a building of choice within the battery life of the drone and given a specific flight plan. The time of flight should be considered as well as the weather conditions when flying the drone. Due to the time constraint in which this project must be completed, the system set-up including the IR camera and drone might not be completed to the final desired result but will instead be completed to a point of proof-of-concept that has validated the ATP's.

Once the drone has reached the area of interest on the building of choice, it should be able to capture IR images in a manner that does not lead to the distortion of the image. Furthermore, the drone itself should be able to handle the weight of the attached IR camera and any other necessary attachments that will be involved for the successful meeting of the user requirements.

The operator should be able to control the device via a control panel or smart device from the base of the building and all national regulations should be accounted for when

operating the drone. the IR camera should be used in such a way so that images of high quality may be produced for processing purposes. The images should be processed so as to indicate a general temperature of the area of the building being surveyed. Results from the processing should also indicate any structural weaknesses such as cracks or leaks in the building structure. Lastly, the processed images should also indicate a difference in insulation between newer and older insulations. The processed images maybe presented immediately during an immediate maintenance session or after the survey has been completed in order to determine the required maintenance issues to be handled.

3.1 Requirement Baseline

These requirements outline a basic set-up for the system and follow a high-level discussion approach.

- Develop a low-cost IR-UAV that can be used to survey a building envelope.

  This need has risen from the fact that current IR-UAV technologies are very expensive and require exclusive expertise to process [45], [46].
- The device should be able to give accurate temperature readings.

  This in accordance to the accuracy of a mercury thermometer which is which has a least count of 0.2°C .
- The device should have live video streaming and save the video or data in a database.

  The live video stream will help the pilot to accurately fly the UAV as well. The stored data will be used for future processing.
- The entire system should cost less than R10 000.

  In order for the system to be affordable to the general user. R10 000 was decided as the appropriate figure of cost as in South Africa, this would be sufficient to acquire a UAV of decent quality defined in terms of the requirements for this experiment as well as insure that the general user in the construction industry can afford it.
- The UAV must be able to maintain its height with the additional IR device attached.
- The IR device should have some form of stability control when attached to the UAV.

  This to ensure that it provides stable images that can be thoroughly analysed.
- The system shall be simple to use and should require little to no expertise in the

field.

- Smart algorithms should be developed that can detect, thermal bridges, cracks and leaks.
- The system shall be able to be controlled between a within a visible range.

  Generally, a figure of 100m is used as this will ensure that the UAV is far enough to survey a high rise building and general local buildings, given that the tallest building in South Africa is 172m high, and close enough that it is still visible to the user.

- The system shall be able to transfer data wirelessly within the afore mentioned visible range.

  This is to ensure that the pilot can accurately see what is being surveyed and if there are any obstructions in the flight path.
- The UAV shall be able to fly for at least 10 minutes.

  The time of 10 minutes was chosen. The general, reasonably priced drone within the budget has be found to have a battery life up to 18minutes when brand new. Given the fact that batteries do lose their capacity over time and the fact that the initial stages of the flight might be a bit shaky for the inexperienced pilot as well as the fact that with the IR camera, there will be added mass on the drone, a figure of 10 minutes was chosen as this can still ensure a decent survey of a standard South African building.
- The resolution of the IR camera shall allow for objects to be seen and identified from at least 10m away.
- The temperature range of the IR camera shall be between -10°C to 60°C.

  This temperature range was chosen due to weather conditions in SouthAfrica which boasts an ambient air temperature that generally ranges between -8°C and 45°C. An increase of 60°C was chosen due to hot water pipes in buildings that exhibit temperatures of 50°C and upwards [47]. In addition, analysis will be done on buildings that are cooler inside than outside and vice versa. The analysis should therefore take into account the time of day at which the survey is being done.
- The UAV and it's load shall weigh no more than 1.5kg.
- The processing of the data shall be done in real time after the survey has been completed.

3.2 Functional Requirements

These requirements dictate how the system will be able to accomplish its functions.

Table 3.1: *Table showing the Functional requirements for the proposed IR-UAV set-up.*

Index	Requirement
F1	The system shall be portable and ready to use.
F2	The system shall be able to survey buildings of all shapes and sizes.
F3	The system shall be usable for a finite amount of time.
F4	The system shall be able to take an optical and a thermal image.
F5	The system shall be controllable by an operator.
F6	The system shall be capable of detecting cracks and heat-bridges.
F7	The system shall be relied upon for temperature measurement.
F8	The system shall store all data on board.
F9	All data shall be processed in real-time after the survey has been completed.
F10	The system shall be able to indicate distance from the observed structure.
F11	The system must be able to take clear and stable images.
F12	The system must support it's weight and additional components.
F13	The system shall not be operated in cloudy or rainy weather as well as windy conditions.

3.3 Performance Requirements

These requirements dictate how well the system will be able to accomplish its functions.

Table 3.2: *Table showing the Performance requirements for the proposed IR-UAV set-up.*

Index	Requirement	Mapping
P1	The system shall be usable for at least 10min at a time.	F3, F12
P2	The resolution of the IR camera shall be, at a minimum, 320 x 240.	F4, F11
P3	The system shall be controlled wirelessly, by an operator, up to at least 100m.	F1, F2, F5
P4	The IR camera shall have a temperature range between -10°C and 60°C.	F4, F11
P5	The data processing shall be done within a frame of 30min after the survey is completed.	F9

3.4 Design Requirements

These requirements indicate how the system will be designed so as to meet its requirements.

Table 3.3: *Table showing the Design requirements for the proposed IR-UAV set-up.*

Index	Requirement	Mapping
D1	The system should require little to no technical expertise.	F1, P3
D2	The system shall weigh less than 1.5kg.	F12
D3	The design shall contain two cameras.	F4, F6, F7
D4	The system shall have a gimbal for stabilization.	F11
D5	The system shall contain a distance sensor.	F10
D6	The system shall have an on board microprocessor.	F4, F8, F10
D7	All processing shall be done on PC via image processing algorithms.	P5

3.5 Acceptance Test Procedures (ATP)

The ATP's will be the final point of call in the design process. The completion of these tests will indicate if the prototype is to be successful or not.

Table 3.4: *Table indicating the Acceptance Test Procedures for the proposed IR-UAV set-up.*

Index	Test Procedure	Mapping
A1	The system will we weighed after it is assembly.	D2, F12
A2	A range test for operability shall be conducted.	P3
A3	A flight test shall occur to monitor the time the drone can be tested for.	P1
A4	Specifications shall be checked when deciding on the thermal camera for use.	P3, P4
A5	Images shall be processed to determine the area of a known anomaly.	F6
A6	Images shall be processed to determine the number of anomalies present in a known environment.	F6, D7
A7	The IR camera shall be validated against a thermometer as a means for accurate temperature measurement.	F7
A8	Images shall be processed to determine the average temperature of a surveyed environment.	F7

3.6 Constraints

This section indicates the boundaries in which the project was to made plausible.

- Cost: R10 000.
- Time for project completion: 10 - 14 months.
- Procurement time, given the unreliability of the South African Postal system.
- Time available for system testing. Considering weather and daylight.
- Exchange rates for procurement.
- Export regulations on certain equipment.

Chapter 4

Engineering Design

This section contains 3 subsections, namely: Conceptual Design, Device selection and Segmentation Algorithm Selection. The first deals with a general design philosophy of the system to be used for this project as well as the integration of the different systems. The second section focuses on the selection process of the components needed to meet the user requirements and the third section focuses on a comparison of the different algorithms to be used for the image processing of this project.

4.1 Conceptual Design

This section provides the general philosophy for the prototype that will be operated in order to meet the user requirements. It provides a basic block diagram outlook at the system of operation as well as an explanation for the blocks.

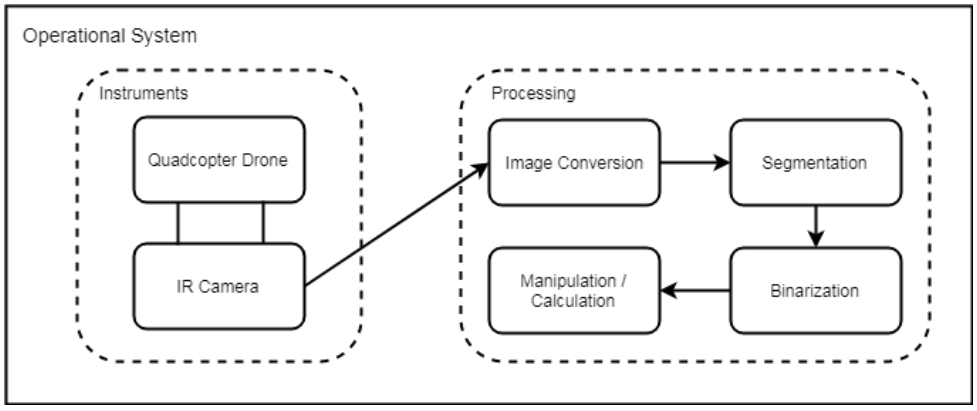

Figure 4.1: *General design philosophy of the Quadcopter and IR camera used for the prototype of this project.*

As seen in Figure 4.1, the operational system is made of two main blocks, namely: Instruments and Processing. The instrument block consists of two parts: The quadcopter drone and the IR camera. The drone will be used to move the camera around so that the surveying can take place.

The processing block contains four blocks. This block represents a computational body that is capable of processing the images. For this project, the processing will be done on a PC, but for future cases, it is possible for the processing to be done on board the drone on a microntroller with a highly reliable GPU. Currently, the four blocks in the processing block are:

Image Conversion - This takes the current image and converts it to a form that makes the processing simpler or ensure that specific features are brought out in the image so that processing can be simpler or produce better results. Examples of this can be changing a colour map or blurring to a certain extent.

Segmentation - This takes place on the image after it has been converted to a form that emphasize specific features. The main focus of segmentation is to extract particular information from an image via a number of different techniques that are discussed in detail further in.

Binarization - This is the process of converting the intensities of the image to either a 1 or a 0 so that certain features stand out with maximum contrast and further processing becomes simpler.

Manipulation / Calculation - This is generally the last step in the image processing process. It generally involves a calculation based on the number of bits in a specific region so as to physically extract data from an image or it involves a manipulation of the number of bits in the image so that a desired result may be reached.

4.2 Device Selection

In this section an in-depth comparison is given to support the selection of the hardware blocks used in order to meet the user requirements. Firstly, a comparison will be given between the different IR cameras available and then a comparison between them so as to ensure that the user requirements are met.

Secondly, the different drones that are currently available on the market and within the

cost constrained will be compared before looking at the differences between their points of operation and weighing up the differences so that the optimal drone may be selected and used for the meeting of the user requirements.

4.2.1 Infra-red Cameras

In order to design a system that will meet the general user requirements, a thorough investigation needs to be carried out with regards to determining the correct sensors, processors and drones for this project.

Table 4.1: *Table indicating the specifications of various thermal cameras.*

Name	Res	Temp Range	Conn.	FOV	Price
Seek thermal [48]	206x156	-40 : 330	μ-USB	36^o x 36^o	R2500
AMG8833 [49]	8x8	0 : 80	I2C	60^o x 60^o	R500
FLIR Lepton3 (chip)[50]	160x120	-10 : 65	SPi	56^o x 71^o	R2900
FLIR 1 [51]	80x60	-20 : 120	μ-USB	50^o x 38^o	R4200
FLIR 1 pro [52]	160x120	-20 : 400	μ-USB	50^o x 38^o	R7100
HT-02 (hand-held) [53]	60x60	-20 : 300	SD card	20^o x 20^o	R2250
FLIR DUO [54]	160x120	-20 : 60	HDMI	57^o x 44^o	R14 000
FLIR VUE [55]	336x256	-20 : 50	-	25^o x 19^o	R25 000
Yuneec Typhoon [56]	198x128	-10 : 180	USB	115^o x 115^o	R21 650
Zenmuse XT [57]	640x512	-10 : 40	μ-SD	90^o x 69^o	R122 560

As seen in Table 4.1 above, the specifications of the different thermal cameras can be seen, however, these do not give one an intuitive feel for what the actual size that is represented by the image that is seen. In order to get this understanding, one chooses a defined distance from the target, in this case it is called the operational diameter. Using the field of view angle, together with the pixel resolution, the Formula (4.1) below can be obtained to calculate the actual image that will be represented by one pixel of the chosen thermal camera. This helps one to get a feel for the type of detail that can be seen from an image. A depiction of this formulation is indicated in Figure 4.2 below.

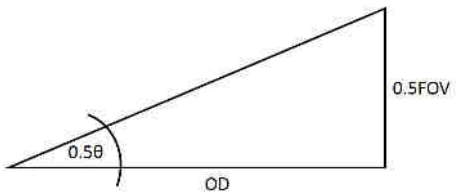

Figure 4.2: *A geometrical interpretation of equation 1.*

$$Area\ per\ pixel = \frac{4OD^2(\tan(0.5HFOV^o) \times \tan(0.5VFOV^o))}{Number\ of\ pixels} \tag{4.1}$$

where:

OD = Operational Diameter [m]

HFOV = Horizontal Field of View [°]

VFOV = Vertical Field of View [°]

number of pixels = pixel length x pixel height

Given the formula above, the area per pixel can be determined for all IR cameras as seen in Table 4.2 below:

Table 4.2: *Table indicating the specifications and area per pixel of various thermal cameras.*

Thermal Camera	**Operational Diameter**					
Name	**0.5m**		**2m**		**5m**	
	A [m^2]	A/p [$\frac{mm^2}{p}$]	A [m^2]	A/p [$\frac{cm^2}{p}$]	A [m^2]	A/p [$\frac{cm^2}{p}$]
Seek thermal	0.10	3.1	1.6	0.5	10	3.1
AMG8833	0.32	5000	5.12	800	32	5000
FLIR Lepton3 (chip)	0.38	19	6.08	3.16	38	19
FLIR 1	0.16	33	2.56	5.3	16	33
FLIR 1 pro	0.16	8.3	2.56	1.3	16	8.3
HT-02 (hand-held)	0.03	8.3	0.48	1.3	3	8.3
FLIR DUO	0.17	8.9	2.72	1.4	17	8.9
FLIR VUE	0.04	0.4	0.64	7.44	4	0.4
Yuneec Typhoon	2.46	9.7	39.36	15	246	9.7
Zenmuse XT	0.69	2	11.04	0.33	69	2

It should be noted that the camera with the smallest area per pixel will indicate the most detail per pixel. Whilst the FLIR VUE has the smallest value of 0.4 at 5m, it exceeds the budget constraints. The Zenmuse XT with a value of 2 at 5m is second, however, this also exceeds the budget constraints. The final decision was to choose between the Seek Thermal, FLIR Lepton 3 and FLIR 1 as these were in budget constraints. It was later found that the FLIR 1 pro utilized the Lepton 3 chip together with it's proprietary software, thus resulting in the high price. The FLIR 1 utilized the Lepton 2 as well as filtering software which helps to provide a clear IR image.

On doing further research, although the FLIR 1 had a larger pixel per area value than the Seek Thermal, it utilizes as particular filtering software that enhances the infra-red resolution and contrast with fusion that takes the IR image and an optical image of the same object. It passes the IR image through a low pass filter in order to smoothen the image and remove noise. It then passes the optical image through high pass filter in order to get outlines and contours of the target object to present themselves. These two images

are then fused to provide a more defined object. The process flow of these images is seen in the Figure 4.3 below[58]:

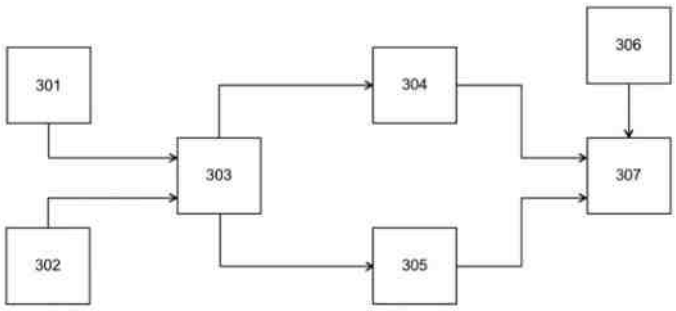

Figure 4.3: *Process flow of the infra-red resolution and contrast enhancement with fusion.* [58]

Where:

301 = Visual image

302 = Infra-red image

303 = Sampling Process

304 = High pass filtered optical image

305 = Low pass filtered IR image

306 = High resolution noise

307 = Fused image

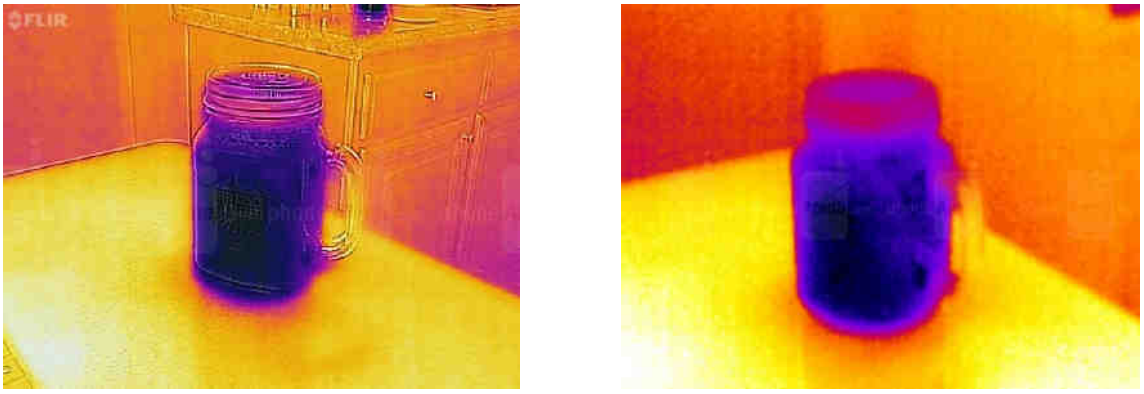

(a) FLIR 1 IR image. (b) SEEK Thermal IR image.

Figure 4.4: *FLIR 1 (a) and SEEK Thermal (b) IR images of a target object.* [59]

As seen in Figure 4.4, the FLIR image clearly indicates a much better defined object where the contours of the target object are clearly seen in comparison to the SEEK Thermal image.

It was therefore decided to purchase the FLIR 1 IR camera for the completion of the experiments, however, due to export regulations, this could not be possible. The FLIR cameras were only exportable to a particular group of countries under U.S. export regulations, this was due to the fact that the FLIR Lepton integrated circuit used in the FLIR 1, was also used in military equipment. The only option left was to purchase the SEEK Thermal, with a value of 3.1 for the 5m operational diameter as it is within the budget constraints, however, only the Compact version was shipped to South Africa.

4.2.2 Drone selection

Drones were decided upon above fixed wings due to the fact that the drone can be kept stationery and offers a lot more control in terms of the application of thermography. There are also many supporting technologies available with drones which will be useful for the purpose of this project. Table 4.3 below shows the specifications of the various chosen drones to decide from, where the price is given is South African Rand, “Res” is the optical resolution “ft” is flight time, “S” is the speed, “R” is the operational range and “M” is the mass of the drone. The drones in Table 4.3 below have already been through a filtering process whereby those within budget and with gimbals for image stabilisation have been selected.

Table 4.1 indicates the specifications of the selected drone batteries for the Ir-Drone set-up where “C” is Capacity in milliamp hours and whilst these batteries are fixed to the above described drones, one can change the battery of the drone in order to meet the desired specifications.

Figure 4.5: *An image of the DJI Phantom Drone, which could be used for the purpose of surveying [60].*

Figure 4.6: *An image of the DJI Spark Drone, which could be used for the purpose of surveying [61].*

Figure 4.7: *An image of the Up Air One Drone, which could be used for the purpose of surveying [62].*

Table 4.3: *Table indicating the specifications of selected drones for the IR-Drone set-up.*

Name	**Price**	**Res**	**R (m)**	**ft(m)**	**Gimbal**	**S (kph)**	**M (g)**
DJI Phantom [60]	5000	4000x3000	1000	25	Y	56	1216
DJI Spark [61]	6000	3968x2976	100	16	Y	36	300
Up Air One [62]	3800	4896x3264	1000	19	Y	50	1350

Table 4.4: *Table indicating the specifications of selected drone batteries for the IR-Drone setup.*

Name	**C(mAh)**	**Volts**	**Type**	**Energy(Wh)**	**Mass(g)**	**temp(°)**
DJI Phantom [60]	4480	15.2	LiPo4S	68	365	5 - 40
DJI Spark [61]	1480	11.4	LiPo3S	16.87	95	5 - 40
Up Air One [63]	5400	11.1	LiPo	59.94	326	-

In addition to the Tables 4.3 and 4.4 above, there are various parameters that need to be taken into account which will aid in the process of drone selection. Such parameters

include upward thrust, blade pitch, blade revolution, amp discharge of the battery and battery capacity. These parameters are represented in the formulas below and will be read off the plots to provide a solution to the selection of the drone.

As per [64], the flight time of a drone can be approximated as follows:

$$FT = (BC \times \frac{BD}{AAD}) \times 60 \tag{4.2}$$

Where:

FT = Flight time [m]

BC = Battery Capacity [mAh] - Defined as the maximum amount of energy that can be extracted from a battery.

BD = Battery Discharge [h] - A phenomenon whereby energy is discharged from a battery without any physical connection and is typically valued at 80%

AAD = Average Amp Discharge [A] - Dependant on motor and load specifications.

If this formula is arranged so that a chosen AAD is decided upon by using the value the general value of available drone motors , we see that BC becomes the independent variable and that FT becomes the dependant variable. It will appear that the relationship is linear as seen It can be seen that the relationship between flight time and battery capacity starts of linear, however due to the finite capacity of the battery and the increased weight associated with increasing the capacity of the battery, the linear relationship tends to taper off and in turn form a curve that settles.

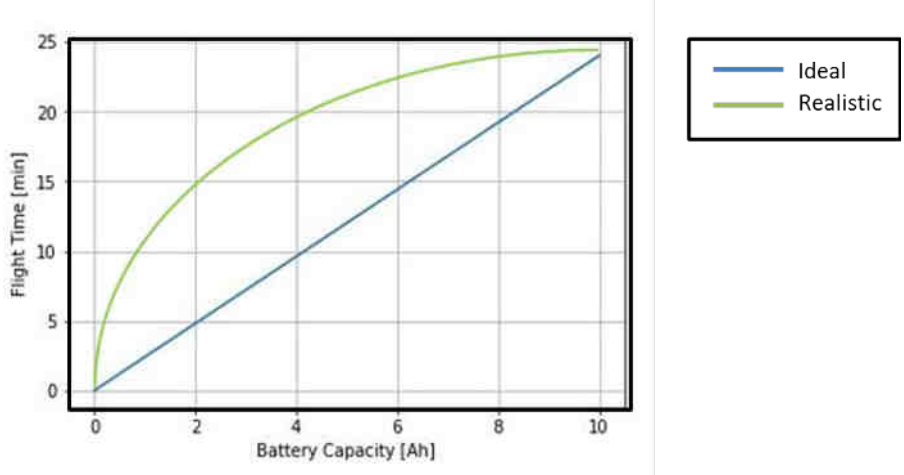

Figure 4.8: *A plot showing the relationship between battery capacity and flight time.*

Due to the fact that the battery capacity generally ranges from 2200mAh to 5400mAh for medium sized drones such as the chosen one for this project, an average battery capacity of 3800mAh was used for the purpose of getting a singular plot and allowing one an intuitive feel for the relationship between flight time and average amp draw.

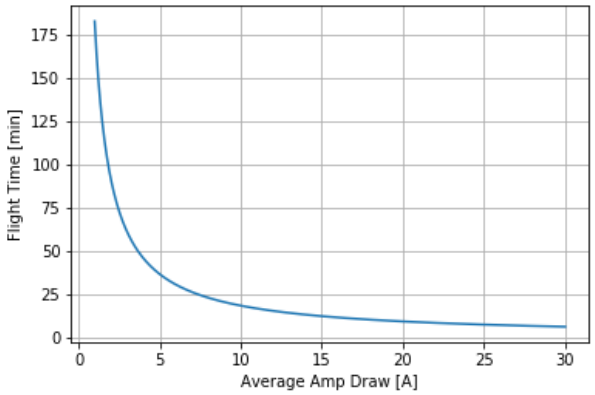

Figure 4.9: *A plot showing the relationship between Average Amp Draw and flight time.*

As seen in Figure 4.8, the formula will dictate a linear relationship as shown in blue, whilst the realistic relationship between flight time and battery capacity will be indicated by the green line and tapers. Figure 4.9 dictates a more hyperbolic relationship between flight time and average amp draw. As a sanity check, if one has a a battery that can supply an infinite amount of power and has no draw, one can expect the drone to an infinite amount of flight time, however, as the draw increases, the flight time will decrease given the finite power of the battery.

It is worth noting that the plot shown in Figure 4.10 above can be used to explain the relationship between flight time, average amp draw and battery capacity. The plot is also related to those in Figures 4.8 and 4.9 above.

The Github link provided indicates how the plot were drawn `https://github.com/NaadirV/IR_DRONE_WORK/blob/master/Codes/Drone_Plots.ipynb`

4.3 Segmentation Algorithm Selection

In this Section, we explore and select the algorithm that will be used for the automatic segmentation of the images during the image processing of the target Infra Red images. The segmentation will be tested against a hole of known size and distance from the camera.

The infra-red images will be taken of the hole from 750mm and 3750mm respectively.

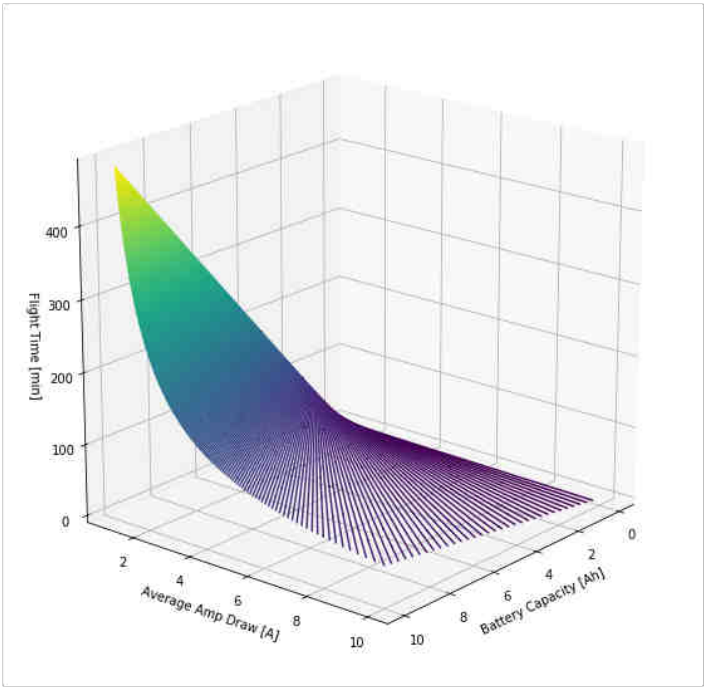

Figure 4.10: *A 3-Dimensional plot indication the plot of Flight time in minutes with respect to Average Amp Draw in amps and Battery Capacity in Amp Hours.*

The area will then be calculated from the number of pixels after the segmentation is completed, in combination with Formula 4.1. An error will then be calculated between the actual size and the calculated size in question. The segmentation that results in the lowest combined error of the images taken from the two distances will then be chosen as the method for segmentation.

All the algorithms were implemented using Python on the Jupyter Notebook as well as many libraries such as OpenCV, Sci-kit learn, Numpy, Scipy and Pyteseract. All codes used can be accessed via the Github links attached in Appendix A. The discussed algorithms based on available subroutines will be:

- Global Thresholding.
- Adaptive Thresholding using Otsu's Method.
- Edge-Based Segmentation.
- Region-Based Segmentation.

To see the code used to execute these algorithms, please click on the url provided `https://github.com/NaadirV/IR_DRONE_WORK/blob/master/Codes/Segmentation_Methods.ipynb`

4.3.1 Global Thresholding

A flow chart diagram for the Global Thresholding algorithm is shown in Figure 4.11. Parts of the code that was used for this algorithm were adapted from [65]

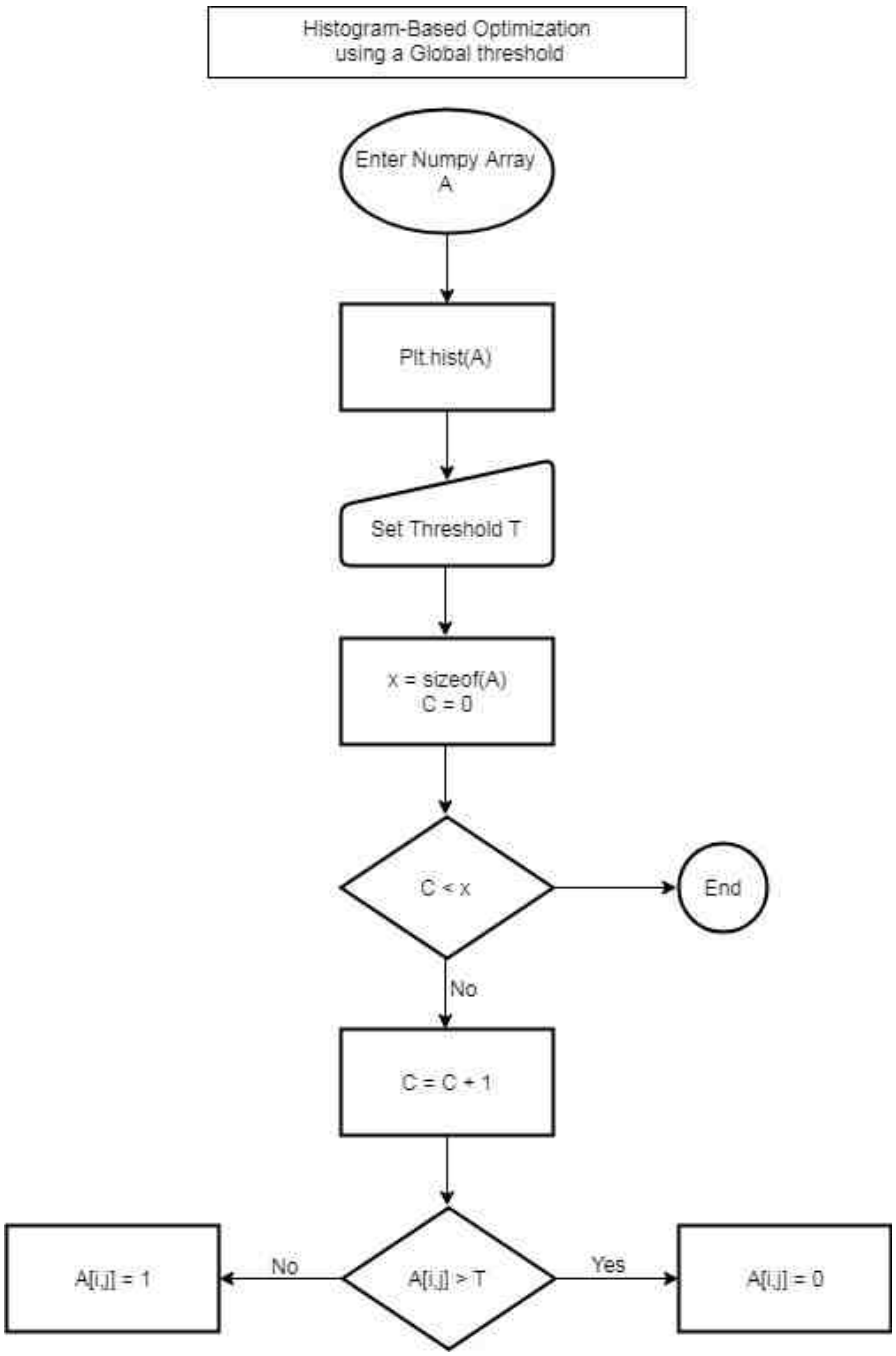

Figure 4.11: *Figure showing a flow chart of the Global thresholding algorithm used for image segmentation.*

Whilst the algorithm can be used to achieve good results based on user requirements, it requires the input of a threshold value which will differ between images depending on the desired results.

4.3.2 Adaptive Thresholding using Otsu's Method

A flow chart diagram for the Adaptive Thresholding algorithm is shown in Figure 4.12. Parts of the code that was used for this algorithm were adapted from [66]

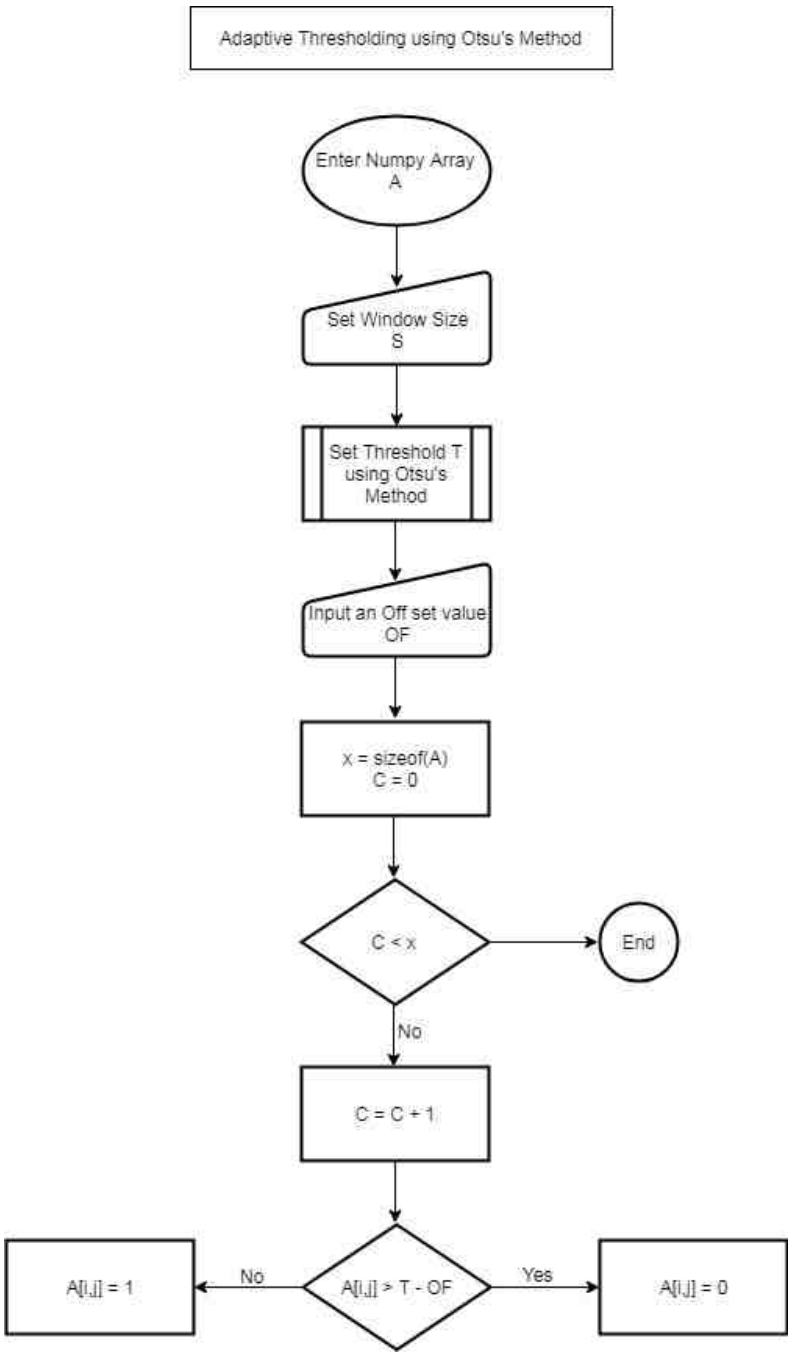

Figure 4.12: *Figure showing a flow chart of the Adaptive thresholding algorithm using Otsu's Method used for image segmentation.*

As in the case of the Global thresholding algorithm, this algorithm can produce great results, however, unlike the Global thresholding algorithm that has one degree of freedom, this algorithm has two degrees of freedom, namely the window size and the offset value. In addition, given large window sizes, the algorithm tends to take more time to process.

4.3.3 Edge-Based Segmentation

A flow chart diagram for the Edge-Based Segmentation algorithm is shown in Figure 4.13. Parts of the code that was used for this algorithm were adapted from [67]

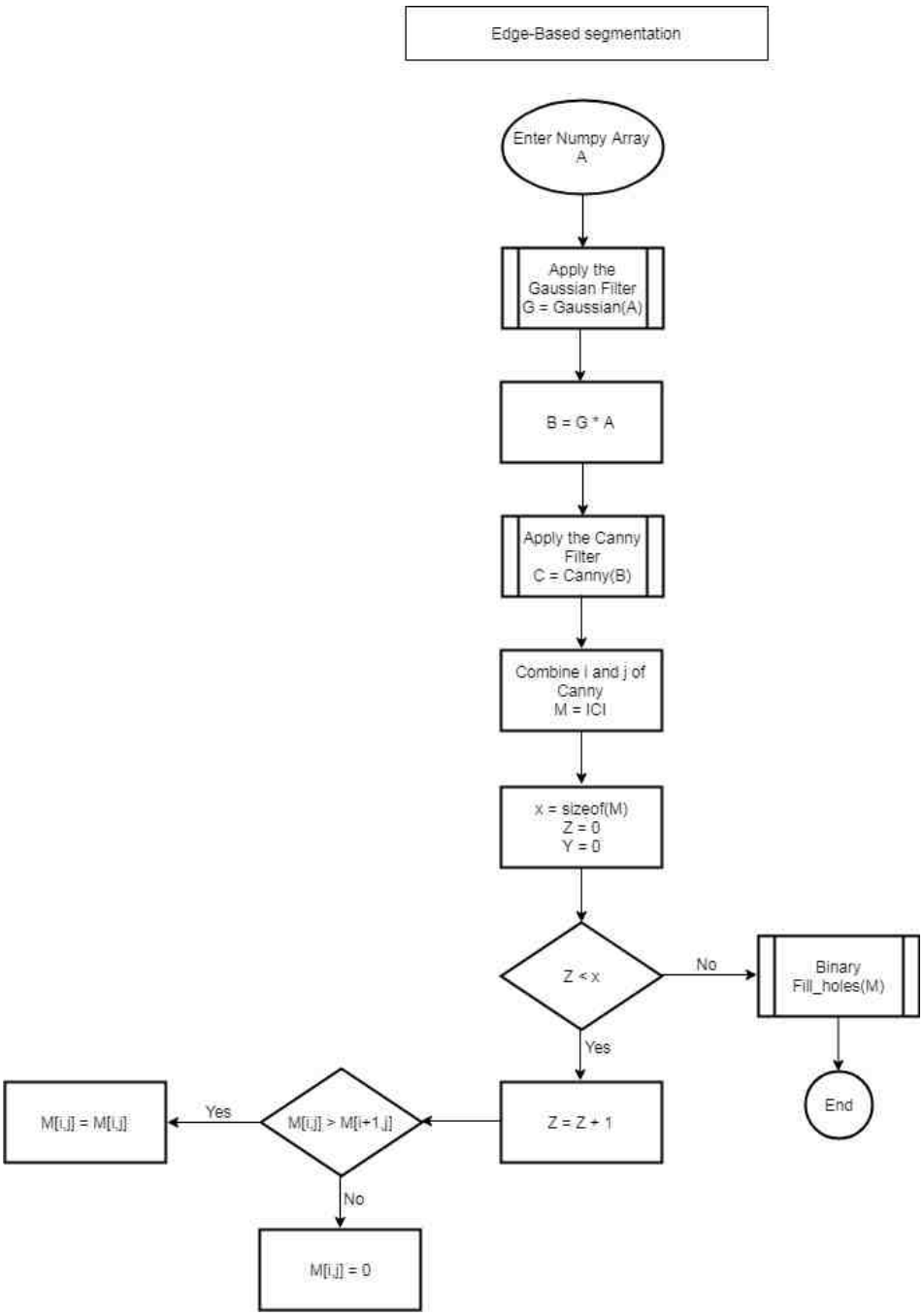

Figure 4.13: *Figure showing a flow chart of the Edge-Based Segmentation algorithm used for image segmentation.*

The advantage of the algorithm is that it has no degrees of freedom, thus using it for automatic segmentation is ideal. However, it has been known to not be very robust and fill in the incorrect holes.

4.3.4 Region-Based Segmentation

A flow chart diagram for the Region-Based Segmentation algorithm is shown in Figure 4.14. Parts of the code that was used for this algorithm were adapted from [67]

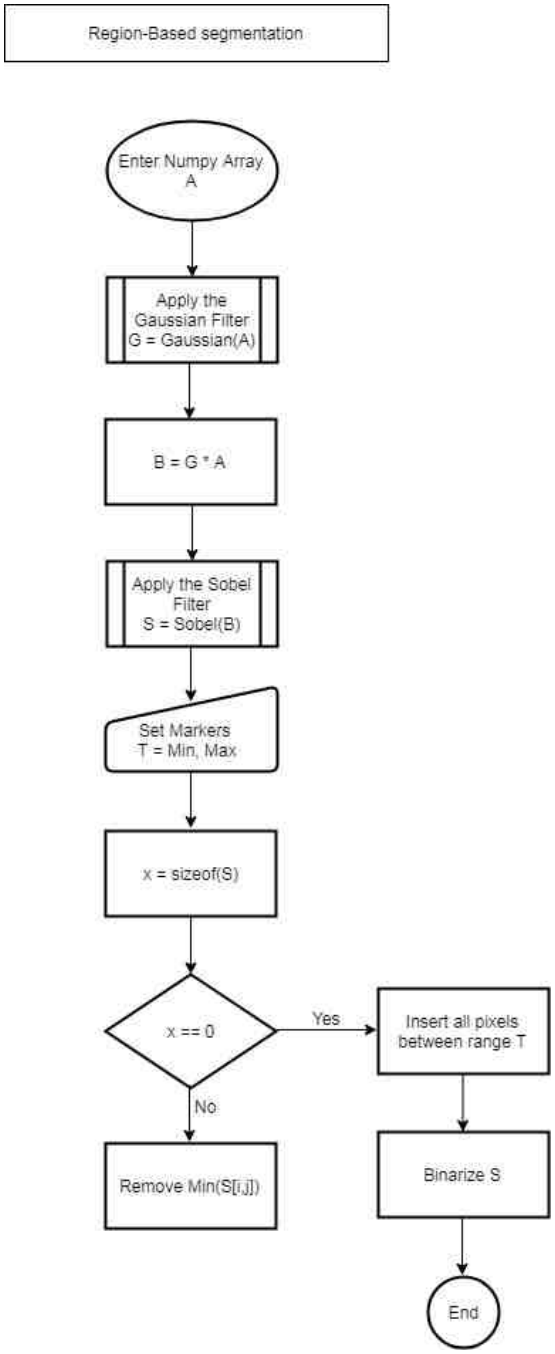

Figure 4.14: *Figure showing a flow chart of the Region-Based Segmentation algorithm used for image segmentation.*

This method can result in excellent segmentation of the image and is fairly robust, however, it requires an input from the user for the markers to be used as a threshold.

4.3.5 Segmentation Results

The images were captured, compared and processed. The areas were calculated and compared to a hole of 60mm diameter with a calculated area at known distances of 750mm and 3750mm respectively. The Tables and Figures below indicate the results of the test.

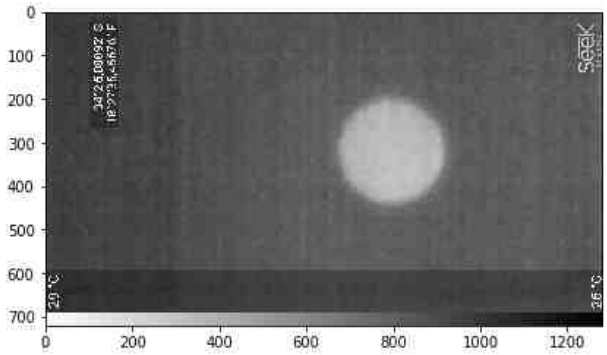

Figure 4.15: *Figure showing the original IR image taken of the 60mm diameter hole taken at 750mm away.*

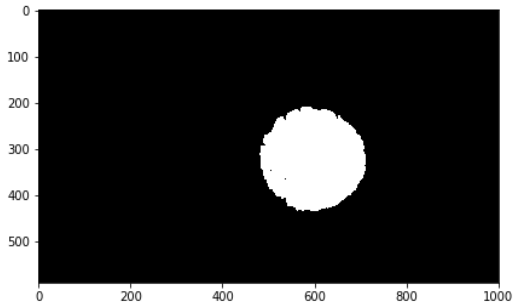

(a) Global Thresholding.

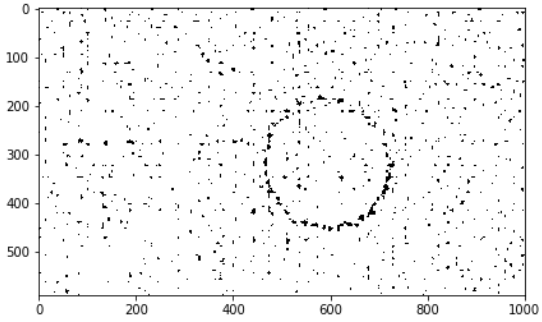

(b) Adaptive Thresholding.

Figure 4.16: *Images of (a) Global and (b) Adaptive Thresholding applied to the IR image of the 60mm diameter hole taken at 750mm away.*

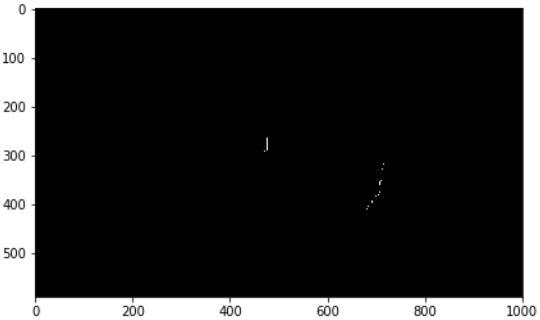

(a) Edge-Based Segmentation.

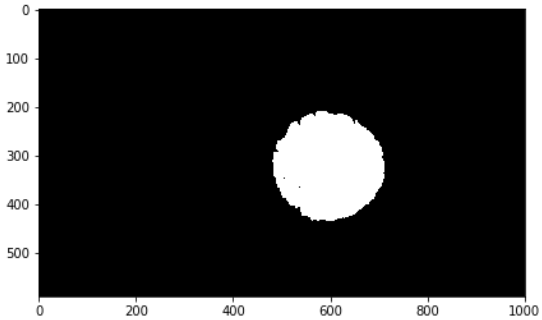

(b) Region-Based Segmentation.

Figure 4.17: *Images of (a) Edge-Based and (b) Region-Based Segmentation applied to the IR image of the 60mm diameter hole taken at 750mm away.*

Table 4.5: *Table indicating the results of image segmentation methods after taking thermal images with the Seek thermal Compact of an illuminated hole of 60mm diameter size taken at 750mm away.*

Param	**Actual**	**Global**	**Local**	**Edge**	**Region**
Area $[mm^2]$	2827.43	4076.43	59152.62	18.41	4076.43
Error [%]	0	44.17	1992.10	99.34	44.17
Radius [mm]	30	36.02	137	2.42	36.02

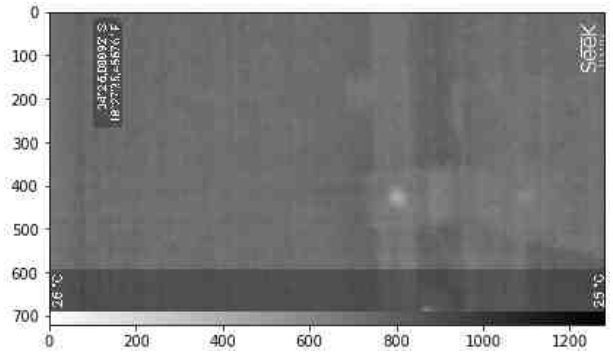

Figure 4.18: *Figure showing the original IR image taken of the 60mm diameter hole taken at 3750mm away.*

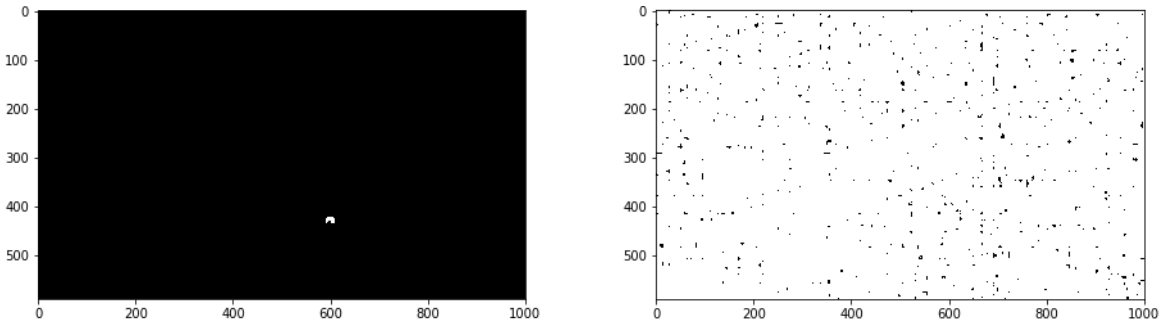

(a) Global Thresholding. (b) Adaptive Thresholding.

Figure 4.19: *Images of (a) Global and (b) Adaptive Thresholding applied to the IR image of the 60mm diameter hole taken at 3750mm away.*

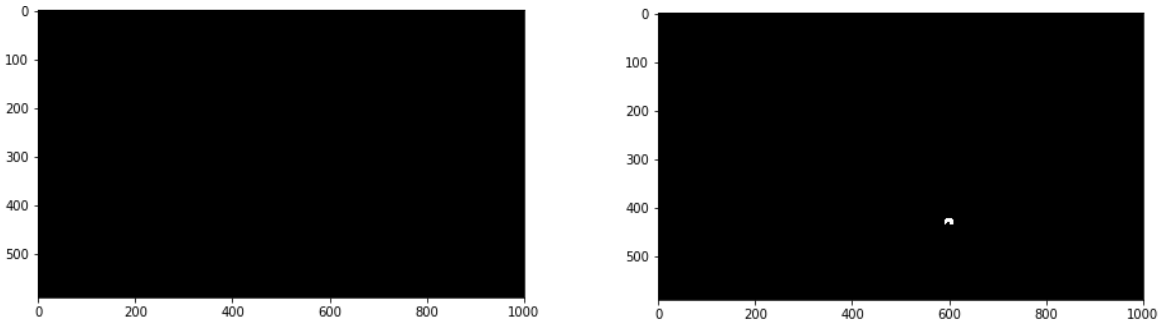

(a) Edge-Based Segmentation. (b) Region-Based Segmentation.

Figure 4.20: *Images of (a) Edge-Based and (b) Region-Based Segmentation applied to the IR image of the 60mm diameter hole taken at 3750mm away.*

Given the results as seen in Tables 4.5 and 4.6, it can be noted that the smallest errors were seen with the Global thresholding and the Region segmentation methods for the im-

Table 4.6: *Table indicating the results of image segmentation methods after taking thermal images with the Seek thermal Compact of an illuminated hole of 60mm diameter size taken at 3750mm away.*

Param	**Actual**	**Global**	**Local**	**Edge**	**Region**
Area $[mm^2]$	2827.43	465.19	1504378.97	0	465.19
Error [%]	0	83.54	531.07	100	83.54
Radius [mm]	30	12.17	2173.97	0	12.17

age processing. The reasons for the errors being the same in both described methods was due to the fact that the values of intensity in the image ranged from 0 to 1. A threshold of 0.65 was then chosen as it could be seen on the histogram to produce the best results. this value was then also used of the Region-Based Segmentation algorithm as a value for the markers. Hence the same value for a threshold was used in the Region-Based algorithm, resulting in the same pixels being segmented.

Given the results, it further added to produce a segmented radius which indicates the size of the radius as calculated from the segmented image. An error of 6.02mm is not excessively big, (only a 20.67%) when focusing on a radius of 30mm. In addition, given the fact that the system will be focusing on inefficiency in a building structure, the size of the error, being larger than the original, will cause for a warning flag to be raised in the structure, hence it will add cause for concern on the anomaly.

The accuracy of the algorithm appears to decrease as the image is taken from further away, but this can only be validated when more images are taken as well as images taken of different size anomalies. The main focus at this point would be to find an algorithm that can dictate a value that can be used as the threshold so that one can make the area detection algorithm automatic.

A possible look into this started with optimization algorithms as the idea was that one could use such an optimization algorithm to produce a figure that could be used as a threshold, given a function that needed to be optimized. The function that was looked into was that of Shannon Entropy which will be discussed in the Automatic Segmentation Algorithms Section in Chapter 5 in the Experiment Designs.

Chapter 5

Experiment Designs

The experiment design section focuses on the design of the experiments that will be used to validate the project and serve to an extent as the Acceptance Test Procedures (ATPs) for the validation of the possible prototype and project.

5.1 Sensor Validation

The experiments in this section provide one with the Acceptance Test Procedures used to validate the IR camera as a sensor that can be used for accurate temperature measurement.

5.1.1 The temperature accuracy test

The aim of this experiment is to ensure the accuracy of the used thermal camera and its reliability in its temperature readings with at worst, a correspondence that falls within the limits of the devices accuracy and tolerance as per its datasheet.

Apparatus:

This experiment requires the use of an IR camera, a calibrated mercury thermometer with a least count of 0.2°C and a temperature controlled environment. The Seek Thermal Compact Infra Red camera was the camera used of this experiment. As mentioned previously, it was not the ideal camera of choice, but it was acquired within the limitations previously mentioned.

Procedure:

The thermometer will be placed in an environment and a reading of the temperature will be taken. It will be used as the control as has been found to be extremely accurate.[68] [69] Simultaneously, a picture will be taken using the IR camera and the temperature will be recorded. The experiment shall be completed by measuring one hundred points of the temperature of:

- Ice.
- Water allowed to stand at room temperature.
- Hot water.
- A corner of a personalized computer monitor.

The temperature reading from the IR camera and temperature from the thermometer shall then be compared using statistical methods with Python on The Jupyter Notebook whilst using the SCIPY and Pandas libraries.

(a) Optical image. (b) Thermal image.

Figure 5.1: *Optical (a) and Thermal (b) images of the mercury thermometer tested in a cup of ice.*

Controlled Variables:

- The item from which the temperature to be measured.
- The number of samples to be measured.
- The environment in which the measured samples are placed.

General Assumptions:

It will be assumed that the datasheets of the thermal IR camera and mercury thermometer are reliable.

(a) Optical image. (b) Thermal image.

Figure 5.2: *Optical (a) and Thermal (b) images of the mercury thermometer in water at room temperature which was kept constant at 21˚(C)*

(a) Optical image. (b) Thermal image.

Figure 5.3: *Optical (a) and Thermal (b) images of the mercury thermometer in previously boiling water in a cooling stage*

(a) Optical image. (b) Thermal image.

Figure 5.4: *Optical (a) and Thermal (b) images of the mercury thermometer placed against a PC screen at 35˚(C).*

Expected Results:

If the general assumptions above are true, it should be found that the temperature reading from the thermometer and the IR camera are very similar, if not the same: They should

be within the bounds of accuracy as stated by their respective datasheets.

Actual Results:

As seen on the Seek Thermal Compact datasheet [48], the thermal accuracy was specified to be 0.5°C within range of the measured temperature on the IR camera. Out of a total of 400 points, 19 were not in the 0.5°C as described by the datasheet.

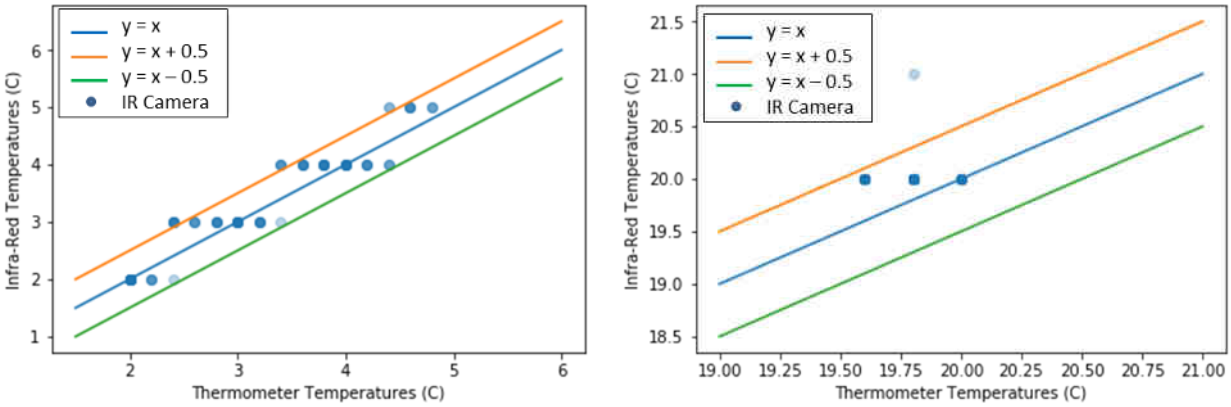

(a) Scatter plot of the Ice test. (b) Scatter plot of the Room temperature test.

Figure 5.5: *Scatter plots showing the temperatures recorded from the mercury thermometer and IR camera of the (a) Ice test and (b) Room temperature tests respectively.*

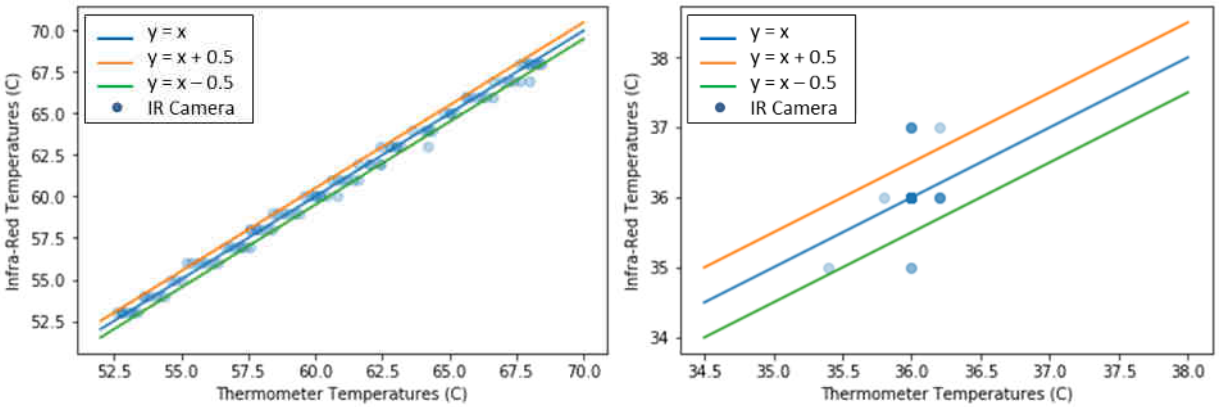

(a) Scatter plot of the Hot water test. (b) Scatter plot of the PC screen test.

Figure 5.6: *Scatter plots showing the temperatures recorded from the mercury thermometer and IR camera of the (a) Boiling water test and (b) PC screen tests respectively.*

As seen in the Figures 5.5 and 5.6 above, there are three linear curves on each plot. The middle curve (blue) indicates the ideal correlation of y = x whilst the upper curve (orange) indicates the upper bound of y = x + 0.5 and the lower curve (green) indicates the lower bound of y = x - 0.5. This will give one a better idea of the errors in each test. One should also take note that each dot signifies one data point and in most of the figures, the dots overlap, thus indicating a more condensed blue colour for overlapping of points.

In order to prove that the IR camera is accurate and can be relied upon for temperature readings, one has to look at statistical measures between the means of the data recorded from the thermometer and that recorded from the IR camera.The data was split into two sets: that of the temperature recorded from the thermometer and that of the temperature recorded from the IR camera.

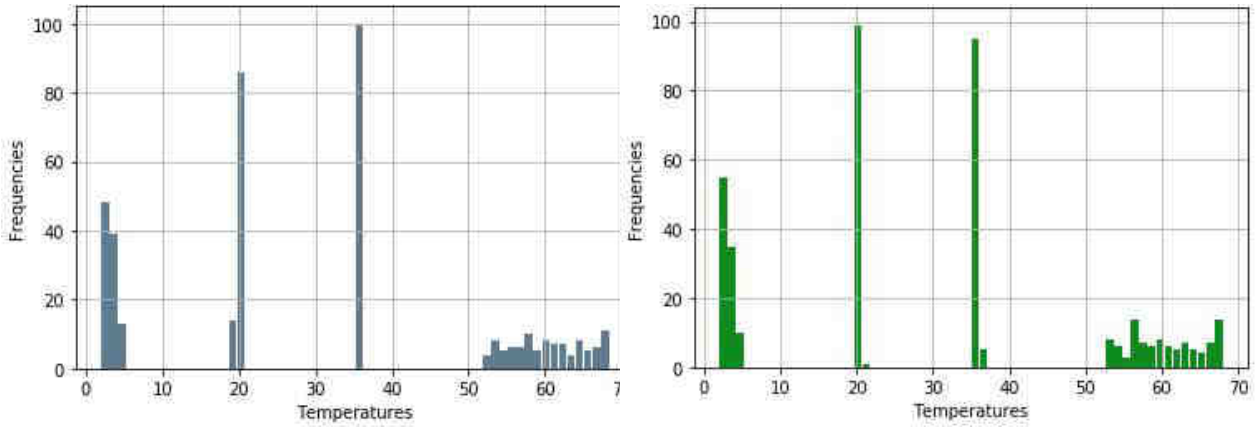

(a) Histogram of thermometer temperatures. (b) Histogram of IR camera temperatures.

Figure 5.7: *Histograms showing the frequency of temperatures recorded from the mercury thermometer (a) and IR camera (b) respectively.*

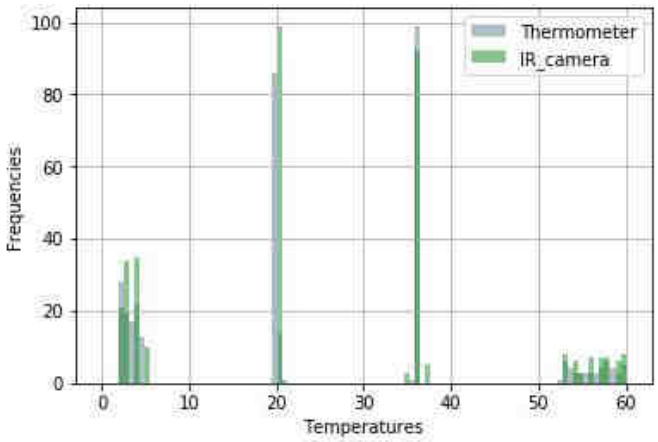

Figure 5.8: *Histogram plot showing the overlay of data from (a) and (b) of figure 5.7 above.*

The paired T-test would be used to determine if the means of the data come from the same or similar sample set and would indicate the difference between them. The relatedness of the means of the data would therefore indicate whether or not the data from the IR camera can be used as a suitable measure for temperature. The paired T-test was chosen due to the fact that both the samples came from the same temperature source.

The Wilcoxon rank test is very similar to the T-test in that it measures if the difference between statistical measures of two sets are zero. However, unlike the mean in the

T-test, the Wilcoxon rank test looks at the medians of the two samples.

The test works on data with at least more than 30 samples where normal distribution is not assumed. It commence by finding the difference between the two data sets and then the absolute difference between them. These are then ranked from smallest to largest. Both the ranks of the negative differences and the positive differences are summed separately. The lowest sum is then taken to be your W-statistic.

The W statistic is compared with W statistic critical values from standard tables. however, for a large number of samples, the Z distribution is used and followed.

For a 2 sided distribution, with an alpha level of 0.05, the corresponding Z scores as per a standard table will be -1.96 on the left and 1.96 on the right. Thus, if the calculated Z score is less than -1.96 or greater than 1.96, the null hypothesis is rejected.

In order to conduct the paired T-test, the data needed to be normally distributed, this was to be confirmed using the Shapiro-Wilk normality test. The test returns a W value and a P value where W is the W statistic and P is the the probability that the data would have been generated by a normal distribution.[70].If the p-value is less than the chosen alpha value which is equal to 0.05, one can reject the null hypothesis of normality of the data with a 95% confidence. If the test is passed, one can conclude that there was no significant departure from normality.

For the Shapiro-wilk test:

$$W = \frac{(\sum_{i=1}^{n} a_i x_i)^2}{\sum_{i=1}^{n}(x_i - \overline{x})^2} \tag{5.1}$$

Where:

n - sample size

x - individual sample points

$\overline{x}$ - mean of the sample

a_i - Shapiro-Wilk constant

The results of the test were as follows:

The paired T-test returns two results, a t statistic and a p-value. The t statistic is a

Table 5.1: *Table indicating the results of the Shapiro-Wilk test for the mercury thermometer and IR camera temperature readings.*

Measure	**Thermometer (Control)**	**IR Camera**
W	0.89789	0.89806
P	$1.02567 \times 10^{-}15$	$1.05775 \times 10^{-}15$

ratio between the difference between the groups and the difference within the groups, therefore, if the t - value is small, it would suggest that two groups of data are similar and if the t-values are large then the groups of data are different. The p-values represent the probability that the results from the sample occurred by chance [71].

For the Paired T-test:

$$t = \frac{(\sum D)/N}{\sqrt{\frac{\sum D^2 - (\frac{(\sum D)^2}{N})}{(N-1)(N)}}} \tag{5.2}$$

where:

$\sum D$ - Sum of differences between thermometer and IR camera readings.

N - Sample size.

The results of the test were as follows:

T-statistic = -5.68309
p-value = $2.55624 \times 10^{-}8$

The effect size is simply a method of quantifying the size of the difference between groups of data [72].

For the effect size:

$$Effect\ size = \frac{[Mean\ of\ IR\ camera\ data] - [Mean\ of\ Thermometer\ data]}{Standard\ Deviation\ of\ Thermometer\ data} \tag{5.3}$$

Effect Size = 0.00383

For the Wilcoxon-Rank Test:

$$W = \sum_{i=1}^{N_r} [sgn(x_{2,i} - x_{1,i}) \cdot R_i] \tag{5.4}$$

Where:

W - W statistic

N_r - Reduced sample (excluding $|x_{2,i} - x_{1,i}|$)

R_i - The rank

sgn - The sign function

The test was carried out on each of the 4 sets of data and then on all the data points together. The results were as follows:

Table 5.2: *Table indicating the Wilcoxon Rank statistics calculated from each of the temperature validation experiments as well as all the experiments combined.*

Test name	**Rank Statistic**
Ice	-0.834
Room Temperature	-10.524
Hot Water	0.051
PC screen	0.093
Combination	-1.405

Conclusions:

As seen from Table 5.1 above, the p-values are many magnitudes smaller than 0.05, thus rejecting the null hypothesis of normally distributed data. However, due to the fact that it is known that temperature is a continuous quantity, the data can be assumed to be normally distributed. This assumption allows one to use the paired T-test.

The results from the T-test above indicate that the data recorded from the IR camera and thermometer are quite different. This is seen by the relatively large t-scores which dictate that the samples are 5.68309 times different from each other. If one compares the calculated t-value to that of a t-value in the standard t-value table at an alpha level of 0.001 with degrees of freedom being 399 [73]. The calculated value of 5.68309 is greater than 3.111 and the p-value is much smaller than the alpha value.This in turn suggests

that there is less than 0.001% chance that the two distributions belong to the same sample population.

Looking at the effect size, one can conclude that the average value of the IR camera temperatures is 0.00383 standard deviations above the average temperature in the thermometer sample. This value is very small, indicating the closeness of the means of the two samples, thus suggesting that the IR camera can be trusted for temperature measurement.

Since the above tests have a large number of samples where n < 30 (n = 100) we will still use the Z-distribution, thus our critical value will still remain -1.96 on the left and 1.96 on the right.

- For the Ice test $Z_{calc} > Z_{standard}$, -0.837 > -1.96 thus the null hypothesis is not rejected and the difference between medians is indeed 0.
- For the Room test $Z_{calc} < Z_{standard}$, -10.52 < -1.96 thus the null hypothesis is rejected, suggesting a difference between the medians.
- For the PC test $Z_{calc} < Z_{standard}$, 0.093 < 1.96 thus the null hypothesis is not rejected and the difference between medians is indeed 0.
- For the Boiling test $Z_{calc} < Z_{standard}$, 0.051 < 1.96 thus the null hypothesis is rejected and the difference between medians is indeed 0.
- For the overall combination of data $Z_{calc} > Z_{standard}$, -1.405 > -1.96 thus the null hypothesis is rejected and the difference between medians is indeed 0.

This then causes one to question why there were 19 measurements not within the specified 0.5°(C) tolerance as stated on the Seek Thermal datasheet - A possible explanation for this could be due to the fact that the IR camera uses a colour calibration method to detect the temperature of the object it is pointed at. Seeing as the effect size between the IR camera data and the thermometer data were very small, one can conclude that the IR camera might not have been correctly pointed at the surface point at which the thermometer was measuring. Thus suggesting that the error in temperature readings was due to human error and not and error in calibration.

5.2 Infra-Red Camera Testing

The tests compiled in this section enable one to understand the limitations as well as capabilities of the IR camera used. The first experiment focuses on using the thermal images to detect anomalies. The second test looks at the ability to use IR images to detect the size of an anomaly and the third test is directed towards using the IR images to detect temperature and validate insulating in newer buildings as being more efficient than those in older ones.

5.2.1 The detection test

The aim of this experiment is to understand the limitations of thermal imaging in crack detection and to develop an algorithm that can detect anomalies and if so, state the number of anomalies. This experiment will also serve as a justification to show that one can use a low cost camera with a lower resolution to extract similar data to a high cost camera with a higher resolution.

Apparatus:

This experiment requires the use of 2 IR cameras and an insulating material placed in front of a heat source. The Seek thermal Compact and Testo 882 with resolutions of 206 x 156 and 640 x 480 respectively will be used. The insulating material, which in this case is a glazed ceramic tile will have holes of varying diameter drilled through it. The holes range in diameter from 3mm, 5mm and 8mm on 1 tile, to 10mm, 14mm and 16mm on the other tile. The tile will be faced with the glazed side facing inward so as to reflect the light and only allow heat through the holes in order to give the best possible result.

Procedure:

Thermal images will be taken with both thermal cameras as seen in Figure 5.9 at distances of 750mm, 1750mm, 2750mm, 3750mm and 4750mm from the insulated box as seen in Figure 5.10, of the holes whilst the interior temperature will remain constant. distance of 750mm was chosen as the initial starting point as it is found that most cameras on drones can focus on object as close as 500mm [74]. Thus 750mm was chosen to ensure that a general drone could focus on the object whilst still not bumping into it if control is not optimal. The thermal images of the Seek Thermal Compact will then be processed using the selected image segmentation algorithm and a comparison of the processed images and

(a) Seek Thermal Compact. (b) Testo 882 Thermal imager.

Figure 5.9: *The two thermal cameras, not to scale, used for this experiment (a) Seek Thermal compact 206x156 and (b) Testo 882 thermal imager (640x480).*

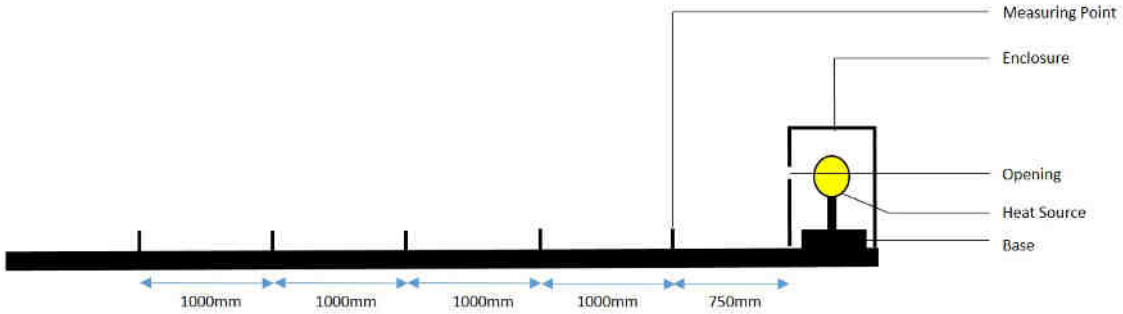

Figure 5.10: *The physical setup for experiment 2.*

the images of the Testo 882 will be conducted in order to reach a conclusion of whether a thermal camera with a lower resolution can be used to acquire the same or similar results.

Controlled Variables:

- Interior temperature of the controlled environment.
- Distance at which the image is taken.

General Assumptions:

The external temperature will be uniform and constant.

Expected Results:

It is expected that on a colour thermal image, the holes will appear brighter than the surrounding material as these would indicate the release and escape of thermal energy.

Actual Results:

(a) Tile with larger holes from 750mm.

(b) Tile with smaller holes from 750mm.

Figure 5.11: *Optical images showing the tiles used for experiment 2 with (a) 16mm, 14mm and 10mm and(b) 8mm, 5mm and 3mm respectively.*

As seen in Figure 5.11, The insulating material used was a 5mm thick ceramic tile with glazing. A tungsten light bulb was placed inside the box and used as the heat source. The sides of the box were sealed off with silicone so as to maximize the heat exiting through the holes.

Table 5.3: *Table indicating the thermal images taken with both the Testo and Seek thermal cameras at various distances of a tile with holes of 16mm, 14mm and 10mm diameters respectively.*

OD (mm)	Testo Image	Seek Image	Processed Image
750	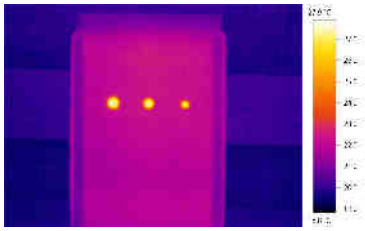	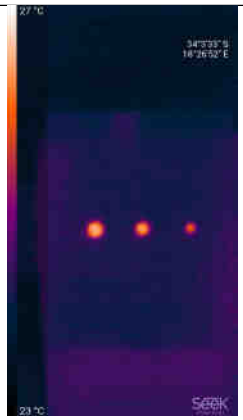	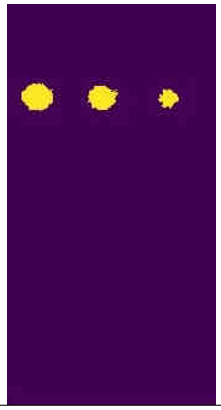

OD (mm)	Testo Image	Seek Image	Processed Image
1750	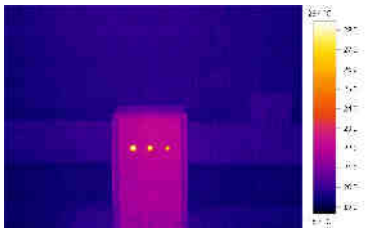	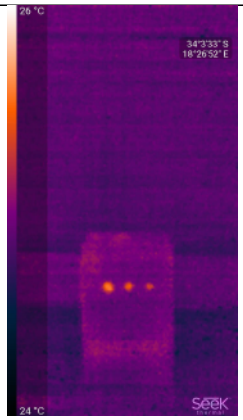	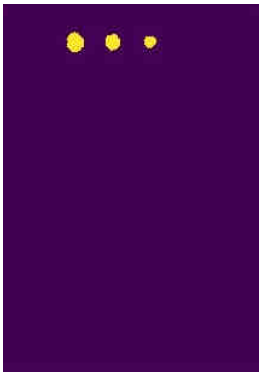
2750			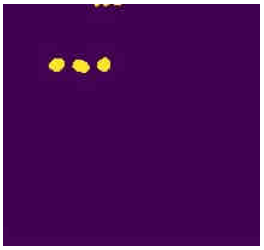
3750	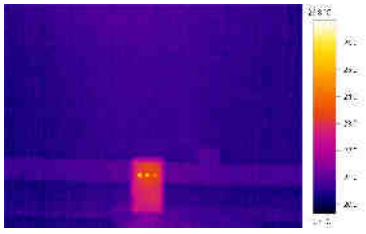	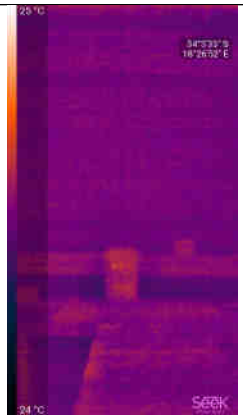	
4750	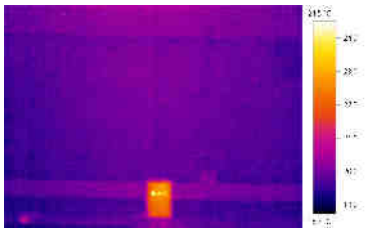	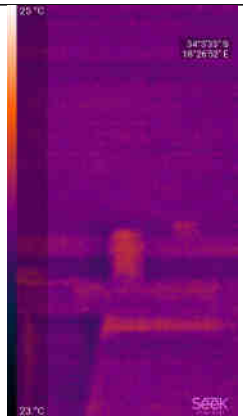	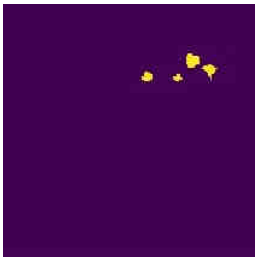

It should be noted that a number of the processed images appear to be differently sized as they have been cropped to remove unnecessary noise from the unfavourable surrounding environments.

Table 5.4: *Table indicating the thermal images taken with both the Testo and Seek thermal cameras at various distances of a tile with holes of 16mm, 14mm and 20mm diameters respectively.*

OD (mm)	Testo Image	Seek Image	Processed Image
750	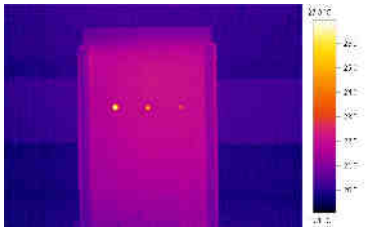	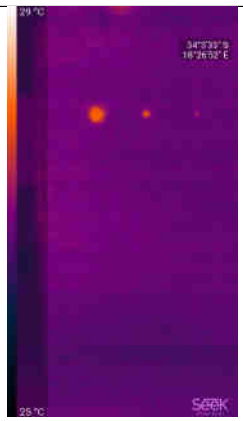	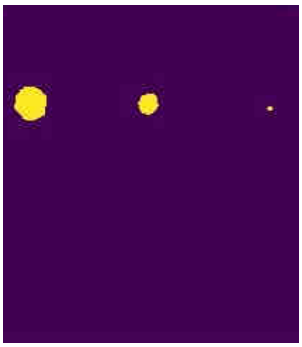
1750	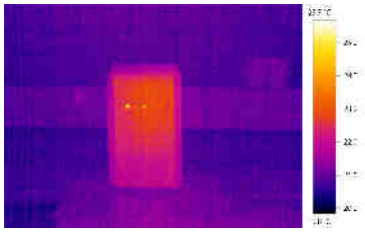	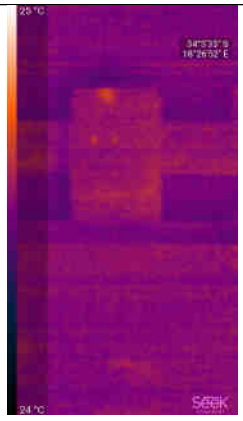	
2750	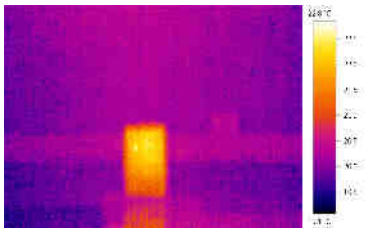	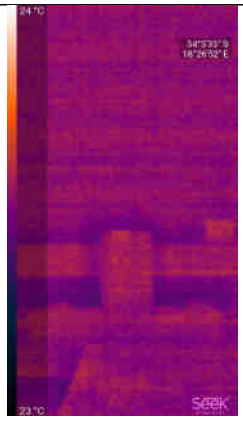	

OD (mm)	Testo Image	Seek Image	Processed Image
3750	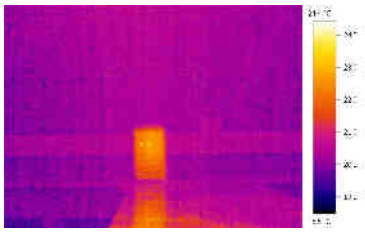	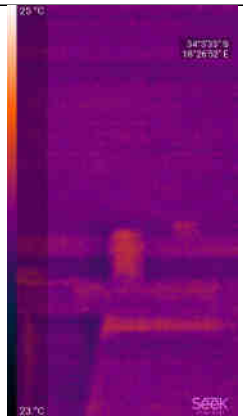	

Conclusions:

It can be concluded from Tables 5.3 and 5.4 above that at specific distances, the anomalies are visible with both cameras and can be seen on the processed images, this is more detailed in the Tables 5.5 and 5.6 below where:

- **Clearly Visible** - 3 separate, well defined holes can be seem
- **Visible** - 3 holes can be seen, but appear distorted.
- **Partially Visible** - Not all holes are well defined or detected, but there is evidence of a hole being visible.
- **Not Visible** - There is no evidence of holes present.
- **Good Detection** - 3 well defined holes are seen in the processed image.
- **Detection** - 3 holes are seen in the processed image, but are subjected to some deformity or noise.
- **Partially Detected** - Not all holes are well defined or detected, but there is evidence of a hole being detected.
- **Not Detected** - There is no clear evidence of any holes being detected.

Table 5.5: *Table indicating the results after taking thermal images with the Testo 882 Thermal imager and the Seek Thermal Compact and processing of the Seek Thermal Compact images of a tile with holes of 16mm, 14mm and 10mm holes drilled from left to right.*

OD (mm)	**Testo**	**Seek**	**Processed**
750	Clearly Visible	Clearly Visible	Good Detection
1750	Clearly Visible	Clearly Visible	Good Detection
2750	Clearly Visible	Clearly Visible	Detection
3750	Clearly Visible	Visible	Partially Detected
4750	Visible	Not Visible	Partially Detected

Table 5.6: *Table indicating the results after taking thermal images with the Testo 882 Thermal imager and the Seek Thermal Compact and processing of the Seek Thermal Compact images of a tile with holes of 8mm, 5mm and 3mm holes drilled from left to right.*

OD (mm)	**Testo**	**Seek**	**Processed**
750	Clearly Visible	Clearly Visible	Good Detection
1750	Clearly Visible	Clearly Visible	Partially Detected
2750	Clearly Visible	Visible	Not Detected
3750	Partially Visible	Not Visible	Not Detected

In the greater aim of the project, when using a thermal camera on a drone, it is very unlikely that one will be flying the drone further than 2m away from the target structure being surveyed given the resolution of the camera and the detailed area that can be represented in one pixel at a distance of 2m , therefore the results are rather promising. It should also be noted that the enclosure used in this experiment was made from 5mm wood. During the course of the experiment, the structure would heat up and cause noise to the image. In a more contextual situation of thick concrete being used, this might result in better insulation, which should result in the anomaly standing out more.

All codes used ti generate plots in this section can be found here: `https://github.com/NaadirV/IR_DRONE_WORK/blob/master/Codes/Temperature_Results.ipynb`

5.2.2 The Area Test

The aim of this experiment is to understand the limitations of thermal imaging in crack detection and to develop an algorithm that can calculate the area of a thermal anomaly such as a hole with a maximum error 10%.

Apparatus:

This experiment requires the use of an IR camera and an insulating material placed in front of a heat source. The Seek thermal Compact with a resolution of 206 x 156 and will be used. The insulating material, which in this case is cardboard with holes laser cut into it for accurate measurements. Each piece of cardboard will have 1 hole. The holes on each piece of cardboard range in diameter from 10mm, 20mm, 30mm, 40mm and 60mm.

Procedure:

Thermal images will be taken with the Seek Thermal Compact at distances of 750mm, 1750mm, 2750mm, 3750mm and 4750mm from the insulated box as seen in Figure 5.10, with the hole whilst the interior temperature or the setting will remain constant. The thermal images of the Seek Thermal Compact will then be processed using the selected image segmentation algorithm and the area of the selected hole will then be calculated and compared to the area of the hole of the originally laser cut anomaly.

Controlled Variables:

- Interior temperature of the controlled environment.
- Distance at which the image is taken.

General Assumptions:

The external temperature will be uniform and constant.

Expected Results:

It is expected that on a colour thermal image, the holes will appear brighter than the surrounding insulating material as these would indicate the release and escape of thermal energy. It is also expected that calculated area will not be extremely accurate due to the heating of the surrounding edges of the material which will distort the results as well as due to the diffusion of heat from the hole being measured.

Actual Results:

The Tables 5.7, 5.8, 5.9, 5.10 and 5.11 indicate the results of the experiment. They show the original greyscale images and processed images after manual segmentation using the Region-Based segmentation approach. The tables also indicate the calculated area for the particular anomaly in question at the specified distances.

Table 5.7: *Table indicating the thermal images and processed images taken with the Seek Thermal camera at various distances of 750mm, 1750mm, 2750mm, 3750mm, 4750mm of a 60mm diameter anomaly.*

60mm Diameter Anomaly			
OD $[mm]$	**Seek Image**	**Processed Image**	**Area** $[mm^2]$
750	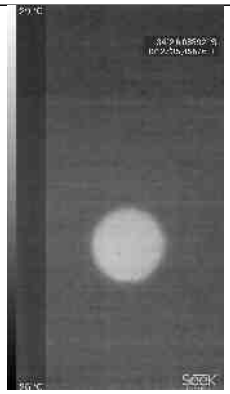	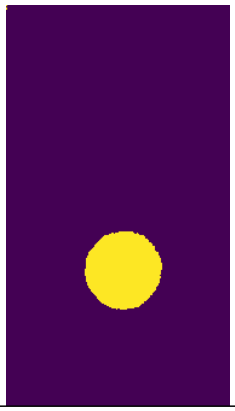	4267.37
1750	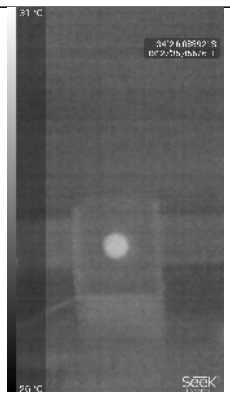	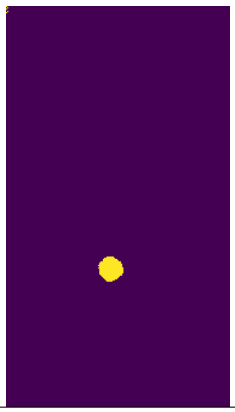	2363.31

60mm Diameter Anomaly			
OD $[mm]$	**Seek Image**	**Processed Image**	**Area** $[mm^2]$
2750	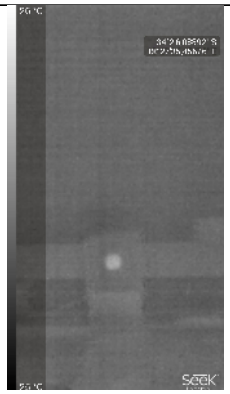	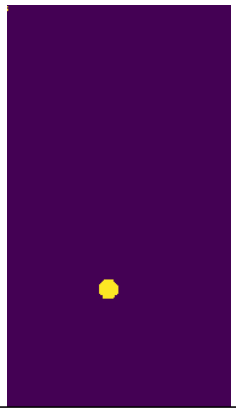	3784.52
3750	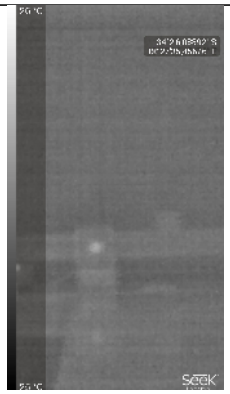	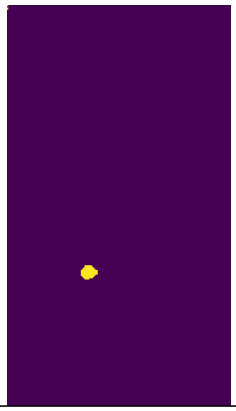	4140.22
4750		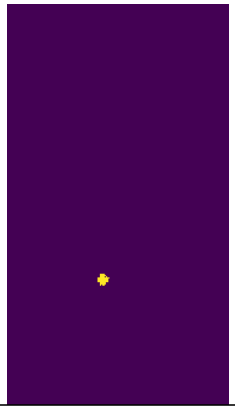	3881.15

Table 5.8: *Table indicating the thermal images and processed images taken with the Seek Thermal camera at various distances of 750mm, 1750mm, 2750mm, 3750mm and 4750mm of a 40mm diameter anomaly.*

40mm Diameter Anomaly			
OD $[mm]$	**Seek Image**	**Processed Image**	**Area** $[mm^2]$
750		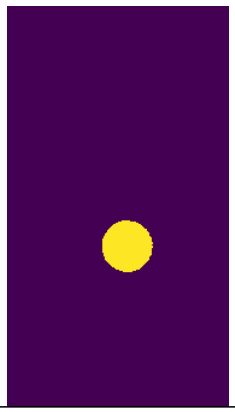	1860.98
1750	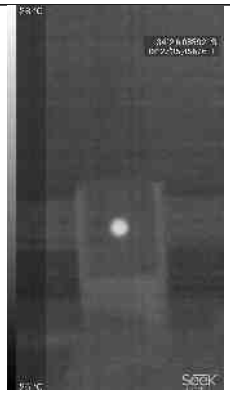	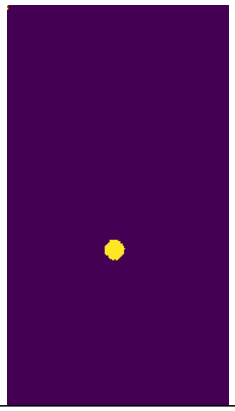	1529.20
2750	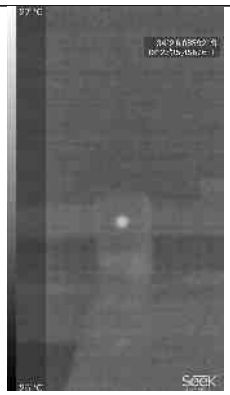	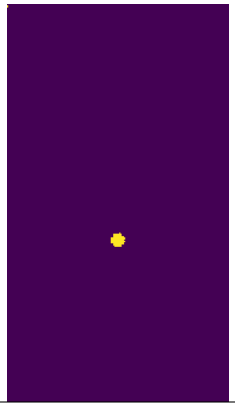	1934.65

40mm Diameter Anomaly			
OD $[mm]$	**Seek Image**	**Processed Image**	**Area** $[mm^2]$
3750	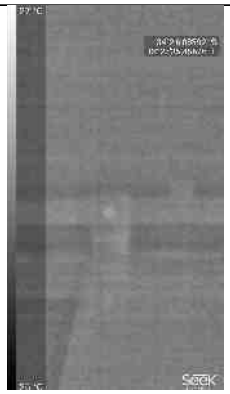	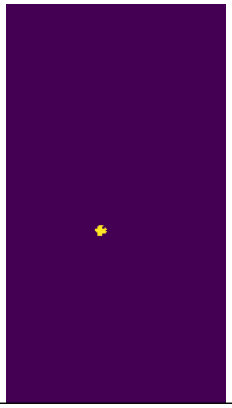	2083.03
4750		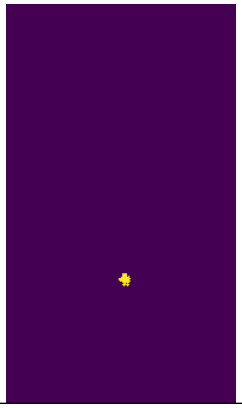	3308.93

Table 5.9: *Table indicating the thermal images and processed images taken with the Seek Thermal camera at various distances of 750mm, 1750mm, 2750mm, 3750mm and 4750mm of a 30mm diameter anomaly.*

30mm Diameter Anomaly			
OD $[mm]$	**Seek Image**	**Processed Image**	**Area** $[mm^2]$
750	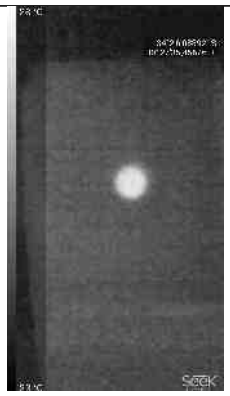	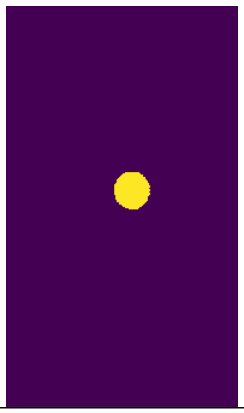	895.13
1750		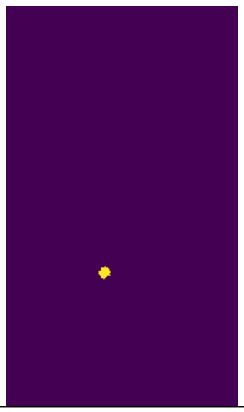	938.23
2750		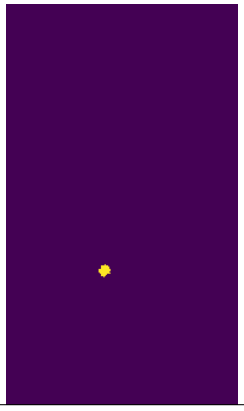	1114.65

30mm Diameter Anomaly			
OD $[mm]$	**Seek Image**	**Processed Image**	**Area** $[mm^2]$
3750	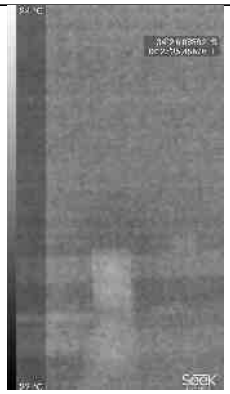	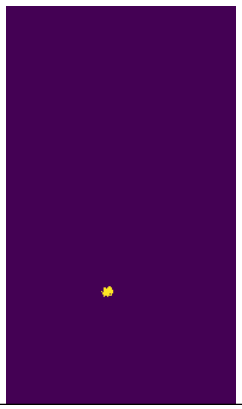	1788.41
4750		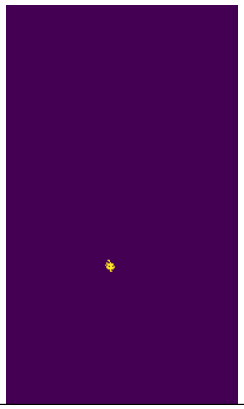	2056.68

Table 5.10: *Table indicating the thermal images and processed images taken with the Seek Thermal camera at various distances of 750mm, 1750mm, 2750mm, 3750mm and 4750mm of a 20mm diameter anomaly.*

20mm Diameter Anomaly			
OD $[mm]$	**Seek Image**	**Processed Image**	**Area** $[mm^2]$
750	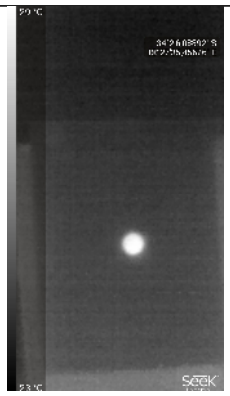	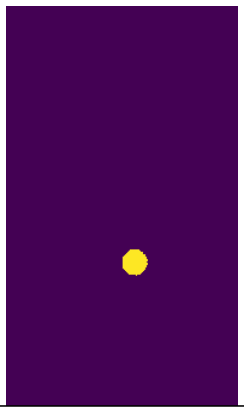	433.25
1750		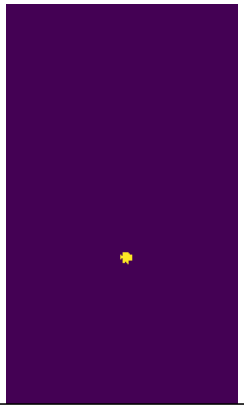	466.58
2750		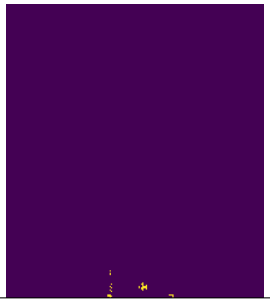	599.02

20mm Diameter Anomaly			
OD $[mm]$	**Seek Image**	**Processed Image**	**Area** $[mm^2]$
3750		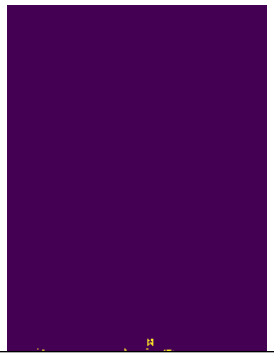	1000.16
4750		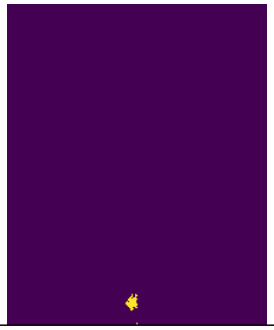	3541.14

Table 5.11: *Table indicating the thermal images and processed images taken with the Seek Thermal camera at various distances of 750mm, 1750mm, 2750mm, 3750mm and 4750mm of a 10mm diameter anomaly.*

10mm Diameter Anomaly			
OD $[mm]$	**Seek Image**	**Processed Image**	**Area** $[mm^2]$
750	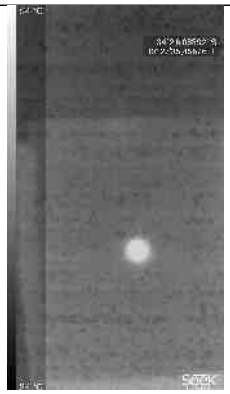	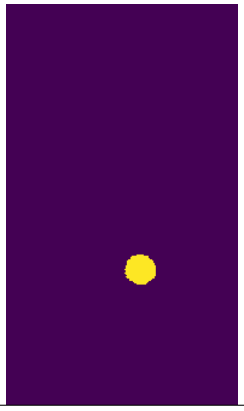	77.43

10mm Diameter Anomaly			
OD $[mm]$	**Seek Image**	**Processed Image**	**Area** $[mm^2]$
1750			437.87
2750		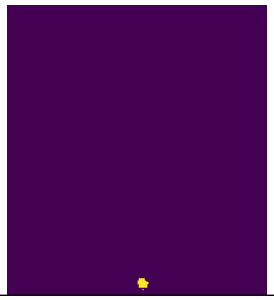	782.47
3750		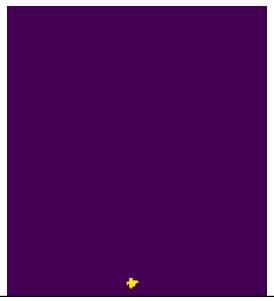	1067.36
4750		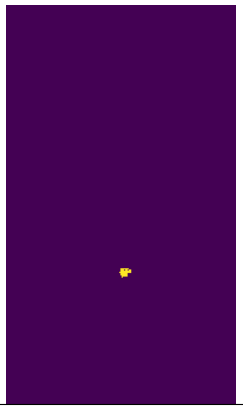	2566.70

It should be noted that a number of the processed images in the Tables 5.7, 5.8, 5.9, 5.10 and 5.11 appear to be differently sized. This is seen particularly for the images taken at further distances due to the FOV capturing a larger area and including unwanted noise in the image, therefore resulting in a cropped image which in turn, removed unnecessary noise. Seeing that the experiment was focused at area detection only, the cropping out of external noise can be seen to be within the scope of the experiment.

The tables to follow, namely Tables 5.12, 5.13, 5.14, 5.15 and 5.16 indicate the mathematical results obtained from the algorithm that calculates the area of the anomaly. In addition, the tables also contain the theoretical diameter of the anomaly from the calculated area. This value is given in order to give one a more realistic feel for what the calculated error actually represents.

Table 5.12: *Table indicating the results from the Area Test from the images in Table 5.7 taken with the Seek Thermal camera at various distances of 750mm, 1750mm, 2750mm, 3750mm and 4750mm of a 60mm diameter anomaly.*

Distance $[mm]$	**750**	**1750**	**2750**	**3750**	**4750**
Actual $[mm^2]$	2827.43	2827.43	2827.43	2827.43	2827.43
Calc $[mm^2]$	4267.37	2363.31	3784.52	4140.22	3881.15
Error $[\%]$	50.93	16.41	33.85	46.43	37.27
Diameter $[mm]$	73.71	54.85	69.42	72.60	70.30

Table 5.13: *Table indicating the results from the Area Test from the images in Table 5.8 taken with the Seek Thermal camera at various distances of 750mm, 1750mm, 2750mm, 3750mm and 4750mm of a 40mm diameter anomaly.*

Distance $[mm]$	**750**	**1750**	**2750**	**3750**	**4750**
Actual $[mm^2]$	1256.64	1256.64	1256.64	1256.64	1256.64
Calc $[mm^2]$	1860.98	1529.20	1934.64	2083.03	3308.93
Error $[\%]$	48.09	21.70	53.65	65.76	163.32
Diameter $[mm]$	48.68	44.13	49.63	51.50	64.91

The figures to follow, namely Figure 5.12, 5.13 and 5.14 represent the data in Tables 5.12, 5.13, 5.14, 5.15 and 5.16 graphically. This graphical representation allows one to find a trend in the errors obtained after the processed images area had been calculated. This error can be graphically seen as the difference between the red and blue graphs.

Table 5.14: *Table indicating the results from the Area Test from the images in Table 5.9 taken with the Seek Thermal camera at various distances of 750mm, 1750mm, 2750mm, 3750mm and 4750mm of a 30mm diameter anomaly.*

Distance $[mm]$	**750**	**1750**	**2750**	**3750**	**4750**
Actual $[mm^2]$	706.86	706.86	706.86	706.86	706.86
Calc $[mm^2]$	895.13	938.23	1114.65	1788.41	2056.68
Error $[\%]$	26.63	32.73	57.69	153.01	190.96
Diameter $[mm]$	33.76	34.56	37.67	47.72	51.17

Table 5.15: *Table indicating the results from the Area Test from the images in Table 5.10 taken with the Seek Thermal camera at various distances of 750mm, 1750mm, 2750mm, 3750mm and 4750mm of a 20mm diameter anomaly.*

Distance $[mm]$	**750**	**1750**	**2750**	**3750**	**4750**
Actual $[mm^2]$	314.16	314.16	314.16	314.16	314.16
Calc $[mm^2]$	433.25	466.58	599.02	1000.16	3541.14
Error $[\%]$	37.91	48.52	90.67	218.36	1027.18
Diameter $[mm]$	23.49	24.37	27.62	35.69	66.15

Table 5.16: *Table indicating the results from the Area Test from the images in Table 5.11 taken with the Seek Thermal camera at various distances of 750mm, 1750mm, 2750mm, 3750mm and 4750mm of a 10mm diameter anomaly.*

Distance $[mm]$	**750**	**1750**	**2750**	**3750**	**4750**
Actual $[mm^2]$	78.54	78.54	78.54	78.54	78.54
Calc $[mm^2]$	77.43	437.87	782.47	1067.36	2566.70
Error $[\%]$	1.43	457.51	896.26	1259.00	3168.02
Diameter $[mm]$	9.93	23.61	31.56	36.86	57.17

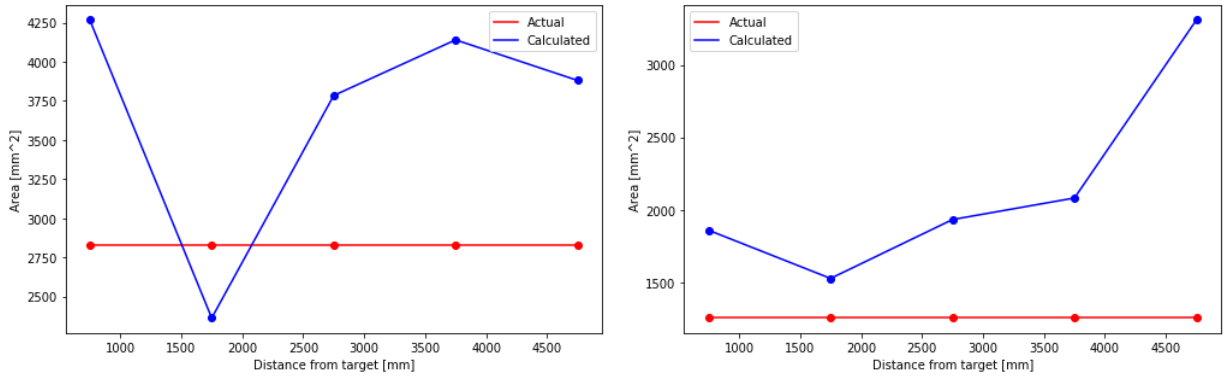

(a) Line graph of 60mm Anomaly.

(b) Line graph of 40mm anomaly.

Figure 5.12: *Line Graphs showing the Actual Area (red) and the Calculated Area (blue) for anomalies of (a) 60mm and (b) 40mm in diameter as taken from distances of 750mm, 1750mm, 2750mm, 3750mm and 4750mm respectively.*

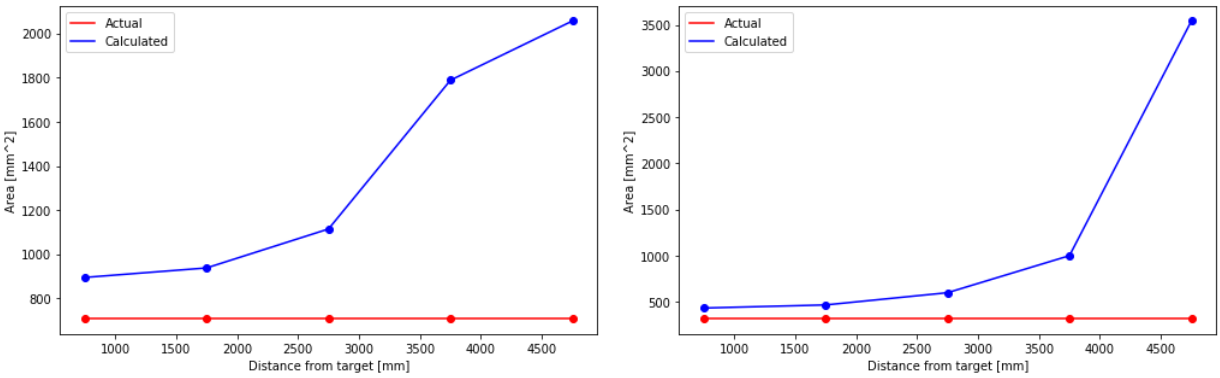

(a) Line graph of a 30mm anomaly.

(b) Line graph of 20mm anomaly.

Figure 5.13: *Line Graphs showing the Actual Area (red) and the Calculated Area (blue) for anomalies of (a) 30mm and (b) 20mm in diameter as taken from distances of 750mm, 1750mm, 2750mm, 3750mm and 4750mm respectively.*

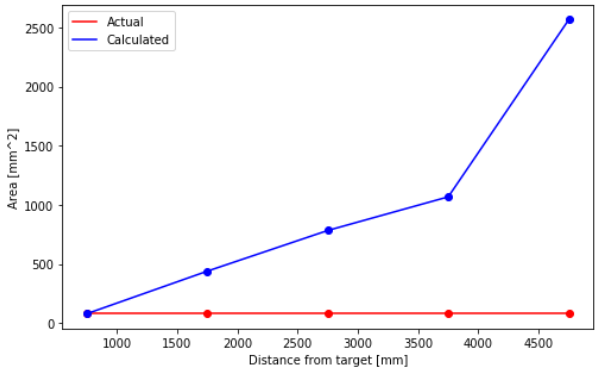

Figure 5.14: *Line Graphs showing the Actual Area (red) and the Calculated Area (blue) for anomalies of 10mm in diameter as taken from distances of 750mm, 1750mm, 2750mm, 3750mm and 4750mm respectively.*

Conclusions:

The overall experiment can be said to be successful in that segmentation was possible and the area of the images was calculated for all anomalies at all the specific, chosen distances. However, only 1 measurement, namely the tests of the 10mm diameter anomaly, measured at 750mm, proved to be within the 10% error. The rest of the anomaly results will be discussed individually below:

60mm Anomaly

When referring to Tables 5.7 and 5.12 and Figure 5.12 a, it is observed that the highest error obtained, was for the closest measurement of 750mm, with an error of 50.93%. This could possible be due to the fact that the anomaly was large and thus the diffusion of heat could have been rapid, hence spreading out across a wide area which was captured in the

image. Even though, the error was large, it resulted in a calculated diameter of 73.71mm, which is only 13.71mm larger than the actual diameter of 60mm. The smallest error of 16.41% was observed at 1750mm. The reason for this is still not completely understood, but one possible explanation might be due to the developed relationship between distance and area per pixel as assumed.

Overall, a maximum of 13.71mm error, is not extremely large in comparison to the size of the anomaly. In addition, having an overestimate will, in the greater essence of the prototype, lead to more concern for the anomaly, hence a large anomaly size is not exactly cause for concern at the moment unless one starts looking into energy loss readings, in which case a more accurate reading will be needed. When looking at the general curve in Figure 5.12 a, it appears as though the error increases with an increase in distance from the object, with an exception for the last measurement at 4750mm. This is a result of the poor resolution of the camera and possibly misunderstood distance/pixel relationships.

40mm Anomaly

When referring to Tables 5.8 and 5.13 and Figure 5.12 b, it is observed that the highest error obtained, was for the furthest measurement of 4750mm, with an error of 163.32%. This could possible be due to the fact that the anomaly was relatively large in terms of the experiment and thus the diffusion of heat could have been rapid, hence spreading out across a wide area. This, together with the poor resolution which was captured in the image, resulting in a large error. This error resulted in a calculated diameter of 64.91mm, which is only 24.91mm larger than the actual diameter of 40mm. Whilst this is big in relation to the anomaly, it is still quantitatively small with regards to the experiment. The smallest error of 44.13% was observed at 1750mm.

When looking at the general curve in Figure 5.12 b, it appears to generally follow a similar pattern to that of part a, with the exception of the last measured point and like part a, the error increases with an increase in distance from the object. This is a result of the poor resolution of the camera and possibly misunderstood camera distance/pixel relationships.

30mm Anomaly

When referring to Tables 5.9 and 5.14 and Figure 5.13 a, it is observed that the highest error obtained, was for the furthest measurement of 4750mm, with an error of 190.96%. This could possible be due to the fact that the anomaly was relatively small in terms of the experiment (half the size of the largest) and the sides of the cut out might have also been heating and thus added to the size of the anomaly detected via the segmentation

algorithm. This, together with the poor resolution which was captured in the image, resulting in a large error. This error resulted in a calculated diameter of 51.17mm, which is 21.17mm larger than the actual diameter of 30mm. Whilst this is big in relation to the anomaly, it is still quantitatively small with regards to the experiment. The smallest error of 26.163% was observed at 750mm.

When looking at the general curve in Figure 5.13 a, the error increases with an increase in distance from the object. This is a result of the poor resolution of the camera as well as a smaller anomaly being detected together with background noise influencing the gradient of the image and possibly misunderstood camera distance/pixel relationships.

20mm Anomaly

When referring to Tables 5.10 and 5.15 and Figure 5.13 b, it is observed that the highest error obtained, was for the furthest measurement of 4750mm, with an error of 1027.18%. This could possible be due to the fact that the anomaly was small in terms of the experiment and the sides of the cut out might have also been heating due to the inability of heat to escape and thus added to the inaccurate size of the anomaly detected via the segmentation algorithm. This, together with the poor resolution and FOV effects which were captured in the image, resulting in a large error. This error resulted in a calculated diameter of 66.15mm, which is 46.15mm larger than the actual diameter of 20mm, more than double. This is big, however, not excessively big in terms of the experiment. The smallest error of 37.91% was observed at 750mm.

When looking at the general curve in Figure 5.13 b, the error increases with an increase in distance from the object. The detection is also reasonable good until a distance of 3750mm. This is a result of the poor resolution of the camera as well as a smaller anomaly being detected together with background noise influencing the gradient of the image and in addition, possibly misunderstood camera distance/pixel relationships.

10mm Anomaly

When referring to Tables 5.11 and 5.16 and Figure 5.14, it is observed that the highest error obtained, was for the furthest measurement of 4750mm, with an error of 3168.02%. This could possible be due to the fact that the anomaly was small in terms of the experiment and the sides of the cut out might have also been heating due to the inability of heat to escape and thus added to the inaccurate size of the anomaly detected via the segmentation algorithm. This, together with the poor resolution which was captured in the image, resulting in a large error. This error resulted in a calculated diameter of 57.17mm, which is 47.17mm larger than the actual diameter of 10mm, more than 5 times the orig-

inal. This is big, in terms of the experiment. The smallest error of 1.43% was observed at 750mm. This is a rather impressive figure to achieve and was the only measure to be within the 10% error as aimed for.

When looking at the general curve in Figure 5.14, the error increases with an increase in distance from the object. This is a result of the poor resolution of the camera as well as a smaller anomaly being detected together with background noise influencing the gradient of the image and in addition, possibly misunderstood camera distance/pixel relationships.

Overall

As mentioned above, the overall experiment can be said to be a successful one in that the quantitative size of the errors obtained were not excessively large in relation to the size of the area they were measuring. However, this result is difficult to generalize as it depends on the thermal properties of the insulating material and surrounding conditions. Nevertheless, in general, it appears as though the increase in distance, particularly from 1750mm for the 60mm and 40mm holes results in a larger error, whilst for the smaller holes of 30mm and 20mm, an increase in distance from 2750mm results in a larger error increase. For the smallest hole, anything from 750mm is highly inaccurate. It would seem as though a “sweet” spot can be obtained for optimal area detection.

5.2.3 The building envelope test

The aim of this experiment is to prove that thermal imaging can be used to detect the insulation or lack thereof in older buildings. This experiment will help with the validation of the IR camera as a proof of concept for the purpose of being used in surveying.

Apparatus:

This experiment requires the use of an IR camera and at least two buildings relatively close to each other: one at least 25 years older than the other.

Procedure:

Thermal images will be taken of both the newer an older buildings as soon as possible and compared via their colours and temperature relations on IR images. The images will be taken using the Spectra colour palette as this shows certain heat loss features very well.

General Assumptions:

It is assumed that a building built 25 years ago will have poorer insulation than a recently built one or that the insulation would have degraded considerably.

Expected Results:

It is expected that the older building will show more areas of heat energy loss than the newer building: these will appear as lighter areas on the grey scale thermal images and orange to red on spectra colourmap images. One would expect to see these lighter areas on corners and joints, especially at the ceilings edge as these are areas that are exposed to the environment.

Actual Results:

It is evident from the images in Figures 5.15, 5.16, 5.17, 5.18 that the newer buildings tend to have more insulation in there general envelope than those of the older buildings: This is evident from the fact that if one studies the newer buildings, there are large areas which are lighter in appearance (yellow/green) than on the older buildings. These lighter areas suggest less heat loss through the insulation.

As seen in Figure 5.19, the older mathematics building on the left has many red areas that indicate a large amount of heat loss through the walls. This is particularly seen in

(a) Optical image.

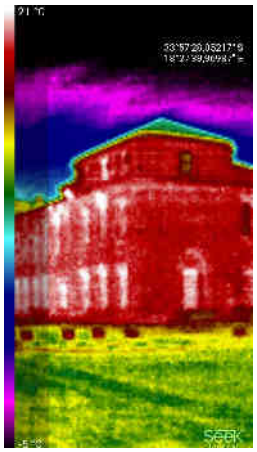

(b) Thermal image.

Figure 5.15: *Optical (a) and Thermal (b) images of the Mathematics building on UCT upper campus.*

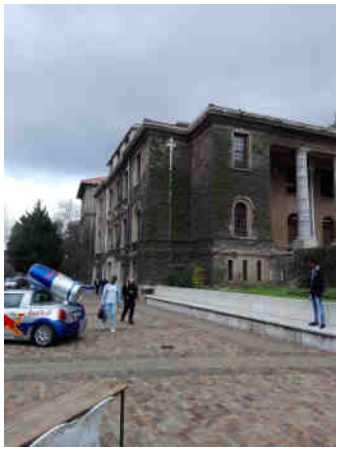

(a) Optical image.

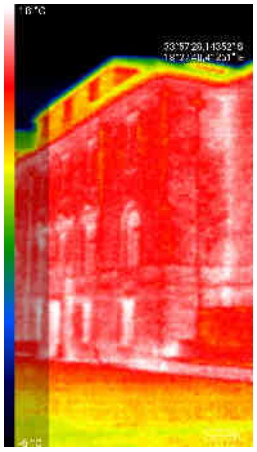

(b) Thermal image.

Figure 5.16: *Optical (a) and Thermal (b) images of the of the Jagger Library on UCT upper campus*

(a) Optical image.

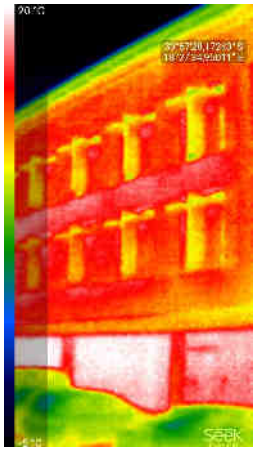

(b) Thermal image.

Figure 5.17: *Optical (a) and Thermal (b) images of the Chemical Engineering building on UCT upper campus.*

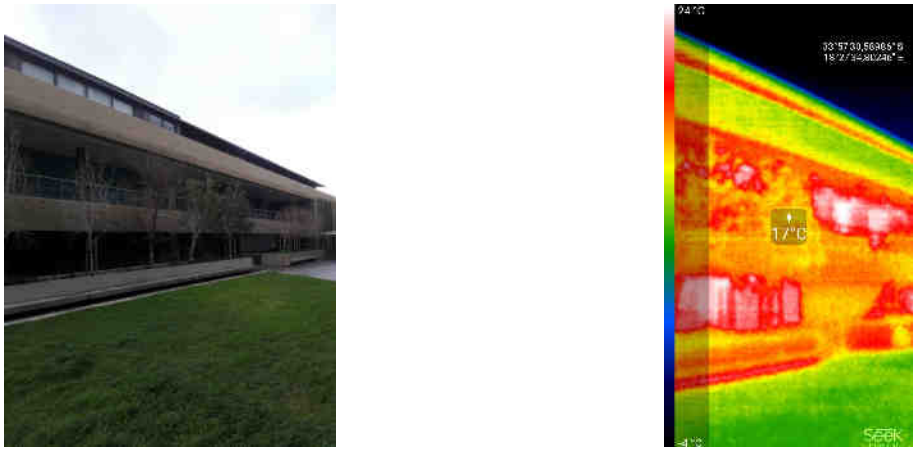

(a) Optical image. (b) Thermal image.

Figure 5.18: *Optical (a) and Thermal (b) images of the of the Snape building on UCT upper campus*

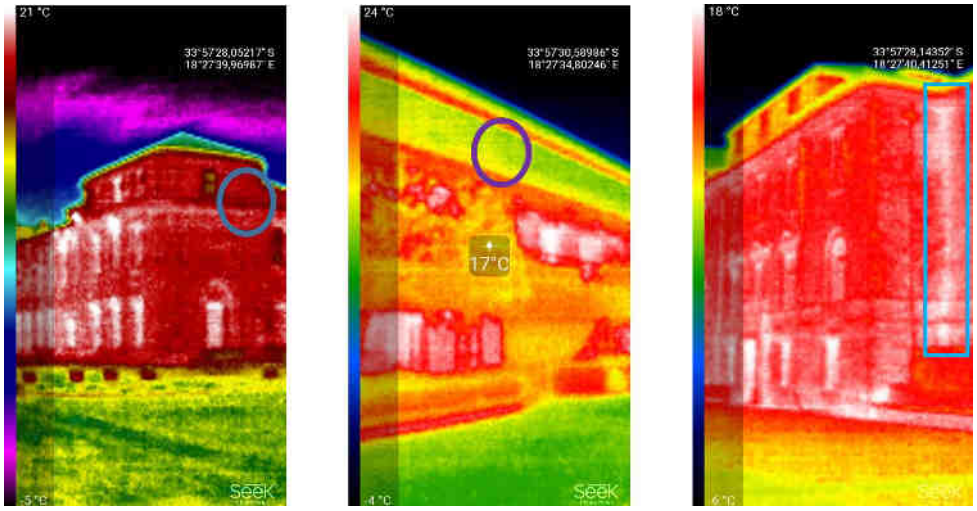

Figure 5.19: *A comparison of old and new buildings as seen through IR images.*

the blue circle on the upper right of the image. It is also seen in the purple circle on the image in the centre that the newer building has more green areas, this indicates less heat loss. The image on the left indicates heat loss and build up along a corner of the old Jagger Library building, this is indicated in the blue rectangle. A possible cause for this would be due to poor insulation or a leak in the corner of the building where the two walls join.

Conclusions:

It is evident from the images above in Figures 5.15, 5.16, 5.17, 5.18 and 5.19 that an IR camera can be used to detect the differences between the insulations of building envelopes and whilst older buildings tend to have a more heat-lossfull structure which will appear to have more brighter red and orange colours on the spectra colour palette of a thermal image, the newer buildings however tend to have more green in their structure

which suggests better insulators in the building envelope and thus less heat loss or gain depending on the temperature differential.

One can thus infer, given that indoor temperatures were the same during the time of the experiment and emissivity was assumed to be the same, that IR cameras can therefore be used qualitatively in the building and surveying environment to help with structural efficiency and heat dissemination from building envelopes.

5.2.4 The building envelope insulation test

The aim of this experiment is to prove that thermal imaging can be used to detect the insulation or lack thereof in older buildings. This will be done quantitatively through the development of an algorithm that will indicate the temperature of the wall of a building. This result will then be used to indicate the efficiency of the envelope of the structure. This experiment will help with the validation of the IR camera as a proof of concept for the purpose of being used in surveying.

Apparatus:

This experiment requires the use of an IR camera and at least two buildings relatively close to each other: one at least 25 years older than the other.

Procedure:

Thermal images will be taken of the old and new buildings on the same day as soon as possible. The images will be taken in greyscale as this helps when processing and reduces data loss if the images where taken in colour and then converted to greyscale.

The indoor air temperature and outdoor air temperature will be measured with a mercury thermometer and recorded. IR images will be taken of the indoor part of the wall and the outdoor part of the wall of the building. These images will then be fed into the algorithm for processing and a weighted average of the temperature will be provided. This will then be used to calculate the relative insulation of the structures of the wall.

General Assumptions:

It is assumed that a building built 25 years ago will have poorer insulation than a recently built one or that the insulation would have degraded considerably.

Expected Results:

It is expected that the older building will show more areas of heat energy loss than the newer building: these will appear as lighter areas on the greyscale thermal images. It can thus be expected that the older building insulators would appear to be less efficient than the newer buildings insulators.

Actual Results:

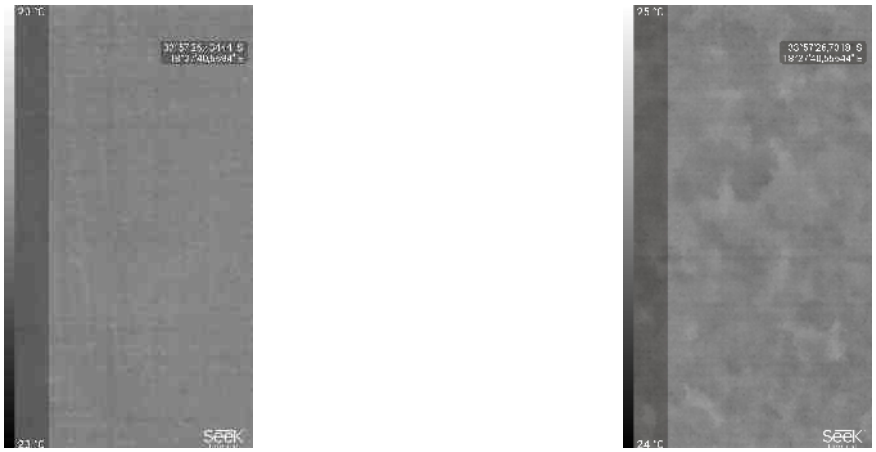

(a) IR image of the inner wall. (b) IR image of the outer wall.

Figure 5.20: *Internal (a) and External (b) IR images of wall of the Mathematics building on UCT upper campus.*

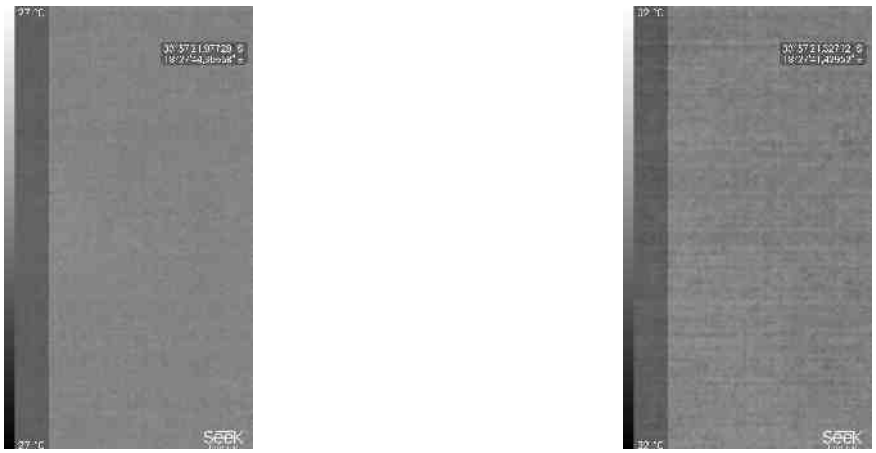

(a) IR image of the inner wall. (b) IR image of the outer wall.

Figure 5.21: *Optical (a) and Thermal (b) images of the of the Jagger Library on UCT upper campus*

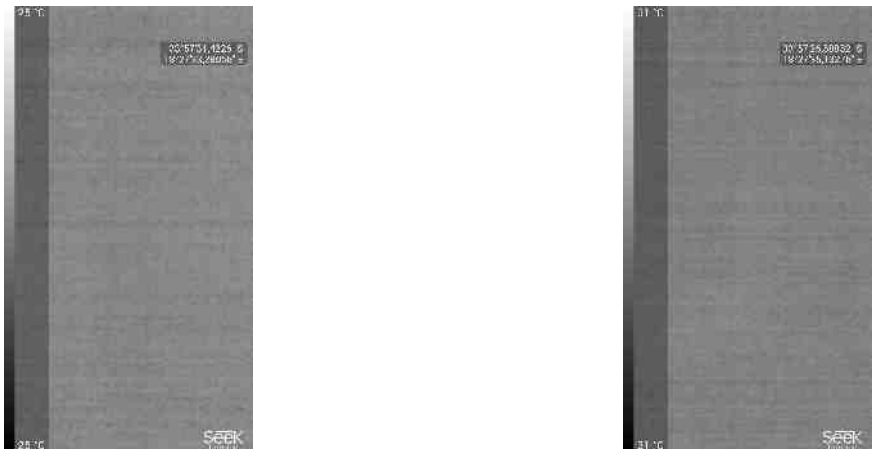

(a) IR image of the inner wall. (b) IR image of the outer wall.

Figure 5.22: *Optical (a) and Thermal (b) images of the Chemical Engineering building on UCT upper campus.*

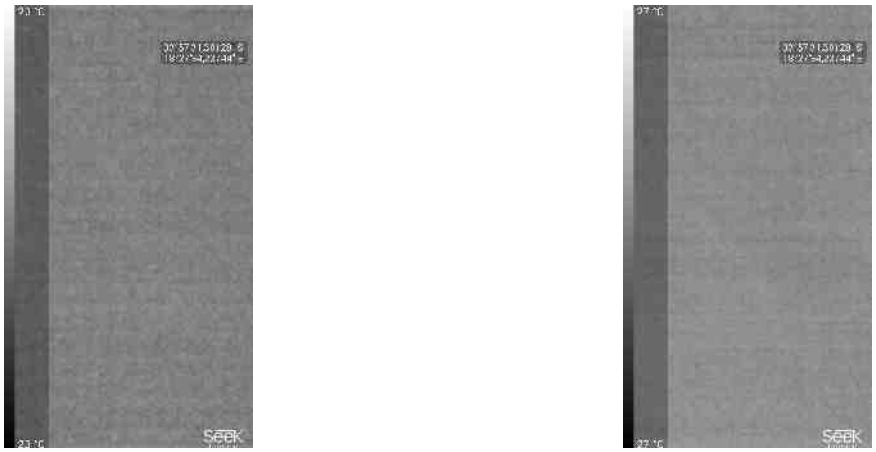

(a) IR image of the inner wall. (b) IR image of the outer wall.

Figure 5.23: *Optical (a) and Thermal (b) images of the of the Snape building on UCT upper campus*

A better indicator of the insulation of the building is seen when looking particularly at the walls of the building as this focusses only on the insulating material of the building and excludes lossy elements such as windows and doorways that are poor insulators.

In order to calculate a more accurate temperature, a weighted average approach was taken, where an iteration through each pixel of the image of the wall occurred. The average value of the pixels was then calculated according to a linear model and using this, an average temperature was calculated for the space of the image. This was done on the same day both for the interior and exterior of 2 new buildings (Snape Building and The New Engineering Building) and 2 old buildings (Mathematics Building and RW James Building). The Buildings have at least a 25 year age gap between new and old and it is hypothesized that the older buildings will provide a less insulated structure than the two newer buildings.

The buildings were compared using the image flow representation as seen in Figure 5.24 below:

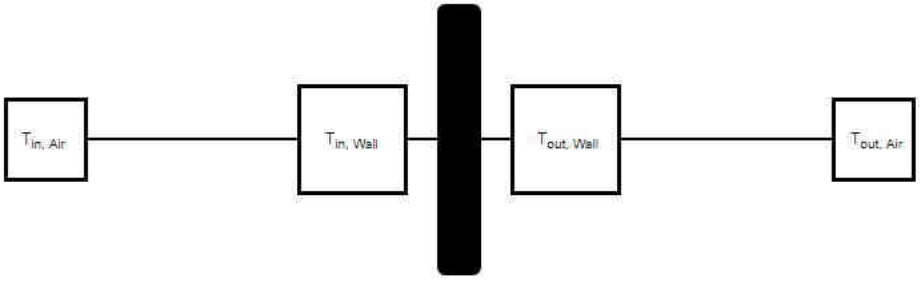

Figure 5.24: *A general quantitative methodology used to determine the effectiveness of an insulator with regards to thermal efficiency.*

Where:

- t_{inair} - Interior air temperature.
- t_{inwall} - Interior wall temperature.
- $t_{outwall}$ - Exterior wall temperature.
- t_{outair} - Exterior air temperature.
- Δt_{wall} - Difference in wall temperature between the internal and external wall temperature.
- Δt_{air} - Difference in air temperature between the internal and external air temperature.
- η - Efficiency of the insulator.

It should be noted that in the ideal situation, the best insulator would not allow any heat transfer between the internal and external environments, thus, it can be said that $t_{inair} = t_{inwall}$ and that $t_{outwall} = t_{outair}$ and where the calculation for efficiency is seen in Equation 5.5

$$\eta = \frac{t_{outwall} - t_{inwall}}{t_{outair} - t_{inair}} \times 100 \tag{5.5}$$

In the ideal case described above, the efficiency would be 100% provided that the internal and external temperatures are not equal. It should also be noted that heat flow from the inside toward the outside of the structure has been taken as positive.

The wall as an insulator can then be modelled using an electrical circuit analogy as seen in Figure 5.25.

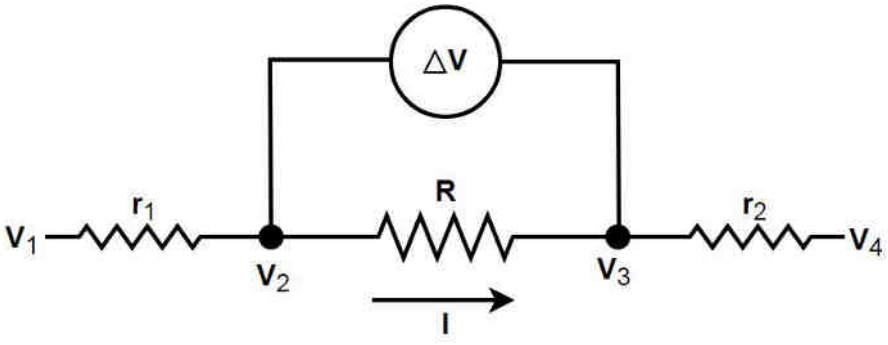

Figure 5.25: *An electrical circuit analogy used to explain the derivation of equation 5.10 and the dependencies on the insulation of an insulating structure.*

- V_1 - Interior air voltage.
- V_2 - Interior wall voltage.
- V_3 - Exterior wall voltage.
- V_4 - Exterior air voltage.
- ΔV - Potential difference accross the wall $= V_3 - V_2$.
- R - Resistance of the wall.

- I - Current through the wall.
- r_1 -Internal air resistance.
- r_2 - External air resistance.

Since heat is defined as the movement of energy from a body of high temperature to a body of low temperature [75]. One can model it as current, I in an electrical circuit. Whilst a difference in temperature is the driving force for heat, a potential difference is the driving force for current, therefore, one can model the temperature difference between the inside and the outside of the wall as a potential difference ΔV. Lastly, since we are interested in the insulation capability of the wall, we can model the wall as a resistor R.

Let us start of by using the general closed circuit equation:

$$R = \frac{V}{I} \tag{5.6}$$

thus, we can say in the case described in Figure 5.25 that:

$$R = \frac{\Delta V}{I} \tag{5.7}$$

Since we are interested in the wall, we will look at the external and internal wall voltages: ΔV, where:

$$\Delta V = RI = V_3 - V_2 \tag{5.8}$$

It can then be said that:

$$I = \frac{V_4 - V_1}{r_1 + r_2 + R} \tag{5.9}$$

Therefore, after substitution of Equations 5.8 into 5.9, we get the following expression:

$$\Delta V = (R) \times \frac{V_4 - V_1}{r_1 + r_2 + R} \tag{5.10}$$

Let us now define the following as the total potential difference of the system:

$$\Delta V_w = V_4 - V_1 \tag{5.11}$$

Thus we can substitute Equation 5.11 into Equation 5.10 and rearrange it to get the following:

$$\frac{\Delta V}{\Delta V_w} = (R) \times \frac{1}{r_1 + r_2 + R} \tag{5.12}$$

One can then find the reciprocal of Equation 5.12 to get:

$$\frac{\Delta V_w}{\Delta V} = 1 + \frac{r_1 + r_2}{R} \tag{5.13}$$

After manipulating Equation 5.13 further, we get:

$$\frac{R}{r_1 + r_2} = \frac{1}{\frac{\Delta V_w}{\Delta V} - 1} \tag{5.14}$$

Given that we are interested in temperature and the insulation capabilities of the the structures, we can replace $\frac{\Delta V_w}{\Delta V}$ with $\frac{\Delta t_{air}}{\Delta t_{wall}}$ to give a new expression below:

$$R_{rel} = \frac{1}{\frac{1}{\eta} - 1} \tag{5.15}$$

Equation 5.15 provides us with a value, R_{rel} a relative insulation that takes into account the external temperatures acting on the surface of the wall and will therefore provide a more accurate result when deciding on which structures are more efficient.

As mentioned previously, an algorithm was developed to indicate the average, weighted temperature of the building wall. The algorithm uses the Pytesseract library which is an Optical Character Recognition (OCR) tool for Python. This tool allows one to read and recognize text on an image and then allows one to covert that text to a string using the image_to_string() command [76]. For this algorithm, the OCR was used on the upper and lower left corners of the seek image in order to identify the text indicating the temperature as per the colour scale of the image. This was then converted to a string and then an integer to be used. Figure 5.26 indicates the flow of the algorithm.

The developed code used in this experiment can be seen here `https://github.com/NaadirV/IR_DRONE_WORK/blob/master/Codes/Weighted_Average_Temperature.ipynb`

As seen in Figure 5.26, the algorithm contains many pre-defined subroutines that are used. Most of the code was adapted from [77]. Firstly, the image is cropped into three parts. The first two parts are the top left and bottom left parts of the image, hence the temperature indicators of the colour palette being used. The third part of the image, which is what is left over after the cropping has occurred, is not considered. The images then get placed through a local segmentation algorithm that uses Otsu's method for the segmenting to occur. This is to segment the text from the background of the image.

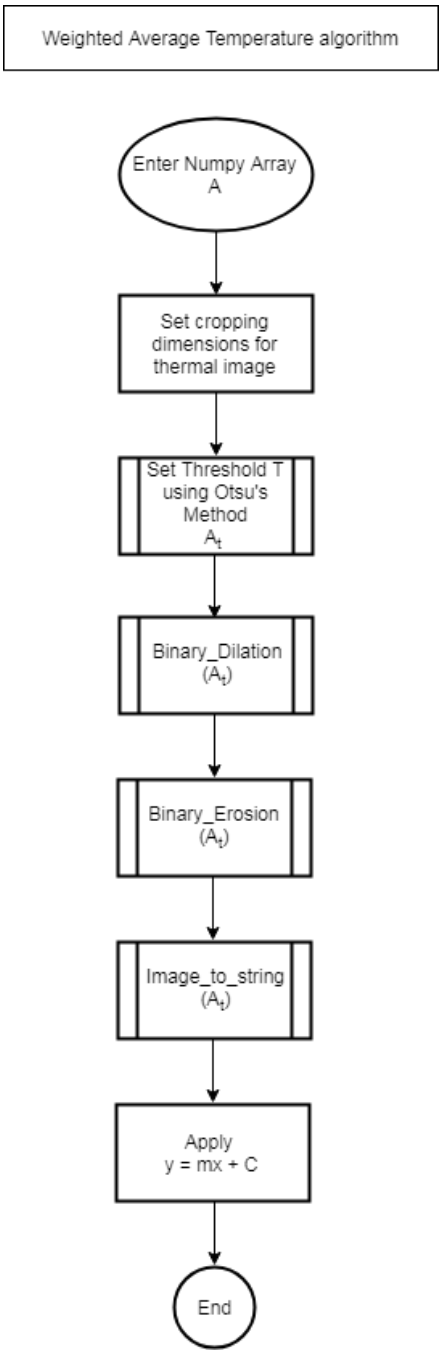

Figure 5.26: *Figure showing the algorithm flow for the weighted-temperature algorithm used to determine the weighted-average temperature.*

The images then get placed through a binary dilator so that they can increase in size, via the number of pixels, without necessarily affecting the resolution of the image as a whole. They are then eroded so that they can appear more defined. One may argue that the process of dilation then erosion, has no effect on the image, but, it does and is referred to as closing and it helps to maintain the shape of the image under which it is operated [78]. The images then both get placed through the image_to_string method in order to be converted to a string. Once converted to a string, they are converted to an integer so that they may be used in the code.

Lastly, the upper number is subtracted from the lower number to find Δx and the intensities of the upper left colour is subtracted from the intensity of the lower left colour in order to find Δy. The gradient m is then found by $\frac{\Delta y}{\Delta x}$. The C value or y-intercept is obtained by using the temperature value at the lower left of the image; this corresponds to the colour black, hence an intensity or x value of 0. Lastly, in order to find an x value to substitute into the linear equation, the average intensity value is calculated.

Table 5.17 indicates the results obtained from the building envelope test using the weighted temperature algorithm.

Table 5.17: *Table indicating the results of the temperature calculation of the walls of 4 buildings on the University of Cape Town Upper Campus. The New Engineering Building, The Snape Building, the Mathematics building and the RW James building.*

Building	t_{ia} [°C]	t_{iw} [°C]	t_{ow} [°C]	t_{oa} [°C]	Δt_w [°C]	Δt_a [°C]	R_{rel}
NEB	21.00	25.00	31.00	32.00	-6.00	-11.00	1.20
Snape	22.00	23.00	27.00	31.00	-4.00	-9.00	0.80
Math	23.00	23.00	24.86	31.00	-1.86	-8.00	0.30
RW James	21.00	27.00	32.00	33.00	-5.00	-12.00	0.71

Conclusions:

It can be seen in Table 5.7 that the newer buildings such as the New Engineering Building (NEB) and the Snape Building had a R_{rel} of 1.20 and 0.80 respectively whilst the older buildings such as the Mathematics building and the RW James building had R_{rel} of 0.30 and 0.71 respectively. Thus indicating that older buildings have building envelopes that offer less insulation that newer buildings.

One can therefore conclude that IR cameras can be used quantitatively for the purpose of efficiency when inspecting building envelopes.

5.3 IR-Drone Automation Experimentation

This section contains two tests. The first focuses on a method to produce an algorithm that will result in automatic segmentation on an image that can help to indicate the area of an anomaly. The second test focuses on the use of a chosen drone as a vehicle for IR, automated, building envelope surveying via an already developed protocol.

5.3.1 Automatic segmentation algorithm tests

The aim of this experiment is to develop an algorithm for automatic segmentation of an image so that the area of an anomaly may be calculated without the physical input of a threshold in the algorithm.

Apparatus:

This experiment requires the use of IR images of an anomaly of a known size. In particular, an anomaly used in The Area Test. The experiment also requires the use of a PC, Jupyter Notebook and Python libraries for the simulations and experimentation to take place.

Context:

As seen in previous tests, the segmentation of the image had occurred manually via the input of a user-defined threshold. This experiment attempts to find a method that will automatically define a threshold that may be used for the image segmentation. The idea to be incorporated is that when building surveying occurs, there will be specifications of the window sizes of the building. One can then use the size of the window in reality and the window in an image to calibrate the size of objects in the image. This will be accurate, given that assumption that the camera dynamics are fully known and correctly implemented into the algorithm.

Procedure:

The experiment aims to use convex optimization in order to optimize an objective function. In this case, we try to optimize the entropy of an image and then incorporate the constraint of the number of pixels in an already segmented anomaly image. This will pass as the window in the real world case.

Controlled Variables:

- The Objective Function to be optimized.
- The incorporated constraint to be added to the optimization.
- The anomaly used for the constrained image.

Expected Results:

It is expected that the threshold that will be obtained from the optimized image will result in segmentation of the image to a point where the anomaly can be detected. The accuracy of the segmentation might not be ideal due to the fact of the camera dynamics not being fully understood. One way around this is to use machine learning to train the algorithm as to what is being searched for, however, this not within the scope of the work and can be looked into for future work.

Procedure and Results:

The chosen anomaly is seen in Figure 5.27. It measures 60mm in diameter and was imaged at 750mm away. It has an area of $2827.43mm^2$. When measured using the Region-Based segmentation method, it appeared to have an area of $4267.37mm^2$. This resulted in an error of 50.93% This error was calculated as a result of the incorrect number of pixels representing the anomaly. Given the Formula 4.1, in order for the image to represent the correct area of $2728.43mm^2$ when imaged at 750mm, it must have 27350.89 pixels which will be rounded up to 27351 pixels that represent it's area.

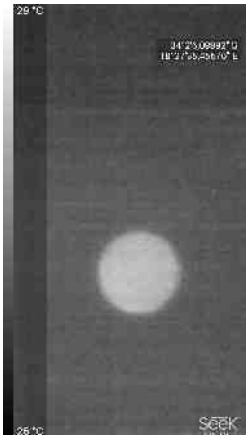

Figure 5.27: *Figure showing the anomaly that will be used for the optimization process as the "window" of a building will be used. This image of the anomaly was taken at 750mm away and the size of the anomaly is 60mm in diameter.*

The entropy of an image can be described as a statistical measure of randomness that can be used to characterize the texture of an image [79]. It is given by the formula:

$$H(X) = -\sum_{i=0}^{N-1} p_i \log_2 p_i \tag{5.16}$$

where:

- N - The total number of elements in the image.
- i - The current element in the image.
- p - The probability of occurrence the element.

The aim of the developed algorithm tends to minimize the entropy of the image with the hope that one can segment the anomaly from the rest of the background. The plot shown in Figure 5.28 (a) indicates the Histogram representation of the image in Figure 5.27 with the x-axis indicating the specific intensities of the pixels in the image and the y-axis indicating the number of pixels with that specific intensity in the image. Figure 5.28 (b) also indicates the Entropy of the image in Figure 5.27 on the y-axis whilst the x-axis indicates the different thresholds as intensities.

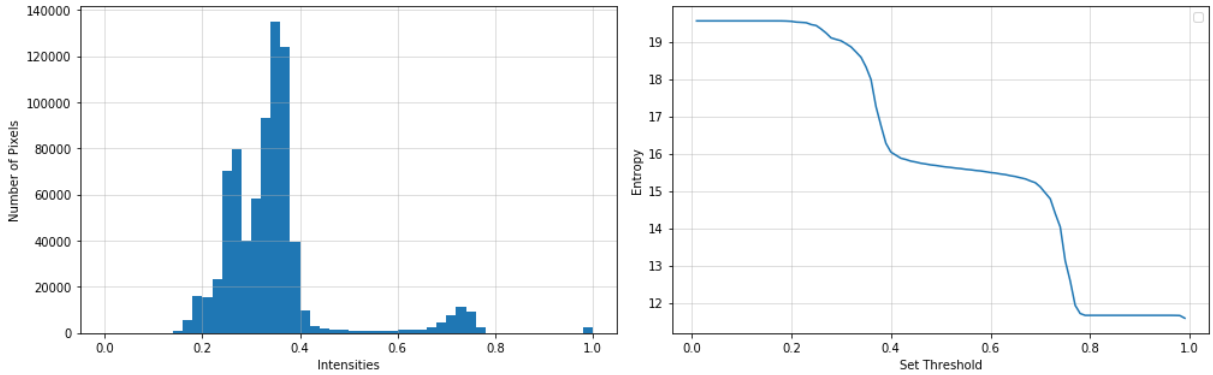

(a) Histogram of the intensities.

(b) Entropy of the image.

Figure 5.28: *Figure showing (a) Histogram representation and (b) Entropy vs thresholds of the associated greyscale image 5.27*

It can be seen in the Histogram, that there are 4 main peaks. The first peak from the left of the Histogram represents the dark grey stripe up the left side of Figure 5.27. The second and larger peak in the Histogram represents the majority grey background in the image whist the smaller and third peak from the left will indicate the anomaly in question. Lastly, the small peak on the right at 1.0 represents the white writing on the image. One can in turn see these 4 regions displayed on Entropy plot in Part (b) of Figure 5.27 as vertical drops. Thus, our area of interest for the intensities representing the anomaly would in general be between 0.64 and 0.77. We can thus be expecting a threshold between 0.64 and 0.77 with an ideal threshold that will be at a point on the peak and roughly around 0.71.

Given the Entropy plot in Part (b), if a minimization optimization was applied to the entropy function, it is clearly seen that the minimal point of the entropy would occur at almost 1 as this is the lowest point of the entropy. It is thus necessary to define constraints around which the optimization must take place. In the real world, these constraints will be obtained from the specified size of the window on a building and the associated pixels within an image that represent that building, however, for the purposes of the experiment, the constraints will applied from the anomaly specifications mentioned previously.

As mentioned previously, the SCIPY.Optimize function allows one to find a minimal point given an objective function. It does this by iterating through a number of input values and inserting them into the objective function. After monitoring the output, the lowest output will be given. As a sanity check, we take a look at the number of white pixels which represent the anomaly with respect to the threshold as well as with respect to the entropy, this can be seen in Figure 5.29.

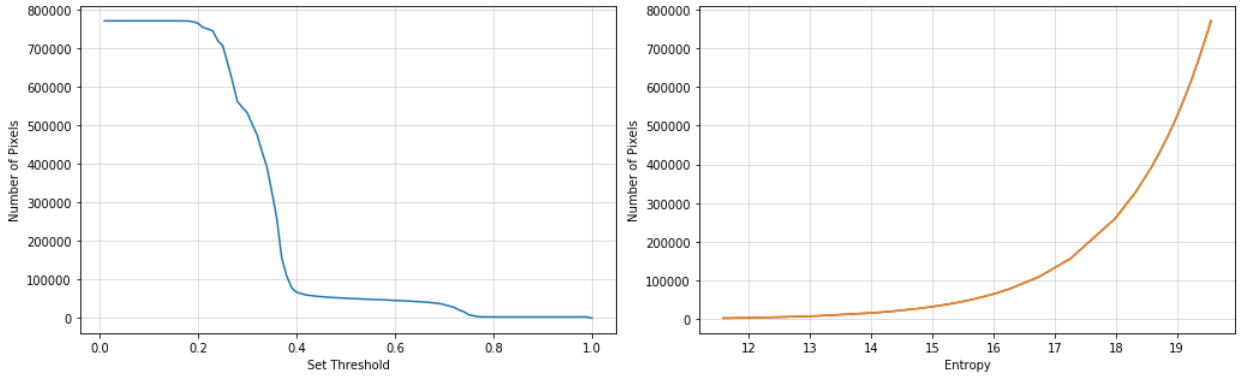

(a) White Pixels vs Intensity Threshold.

(b) White Pixels vs Entropy.

Figure 5.29: *Figure showing (a) White Pixels vs Intensity Threshold(b) Entropy vs number of pixels of the associated greyscale image 5.27*

If one interpolates the plots, we do indeed see that our anomaly of 21351 pixels has a threshold within the 0.64 to 0.77 bounds as previously mentioned, this should correlate to an Entropy between 12 and 15 as a rough estimate.

Whilst trying to constrain the objective function of entropy with the number of white pixels, there were some unforseen issues that had occurred with the optimize.minimize() function. This was due to the fact that Python 3 was used, whilst the optimization function was written for Python 2 and there were some translation issues. The optimize.minimize_scalar() function was used instead and the objective function returned the number of white pixels with the condition that follows:

$$p = number\ of\ white\ pixels$$

$$if\ (p < 23751):$$

$$p = max(image)$$

$$else:$$

$$return(p)$$

This in turn resulted in a plot as seen in Figure that has a clearly define global minimum that can be solved via the optimization method.

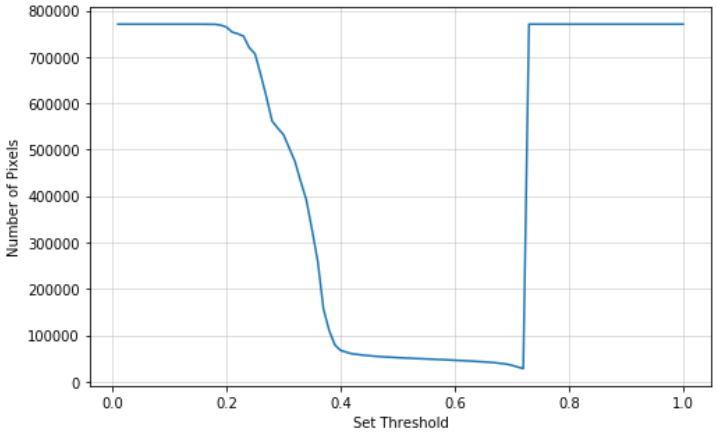

Figure 5.30: *Plot indicating the number of white pixels with respect to the intensities for an anomaly of 60mm imaged at a distance of 750mm after being passed through the optimization algorithm.*

As can be seen in Figure 5.30 there appears to be global minima between the previously theorized regions of 0.64 to 0.77. One can then expect the correct segmentation to occur. After running the image through the segmentation algorithm and the optimization algorithm, a threshold of 0.719 was received. This value was then placed in the segmentation algorithm and an image seen in Figure 5.31 was received.

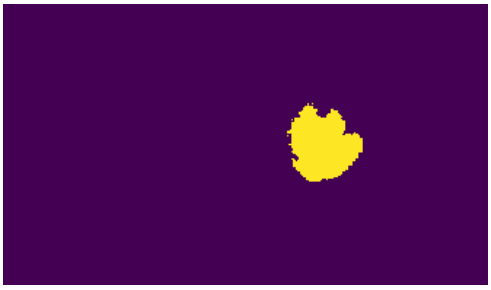

Figure 5.31: *Plot indicating the number of white pixels with respect to the intensities for an anomaly of 60mm imaged at a distance of 750mm after being passed through the optimization algorithm.*

On visual inspection of Figure 5.31, it appears as though the anomaly has not been seg-

mented correctly as it does not appear round, however, on further inspection, on sees that the calculated area as a result of the optimization is $2225.27mm^2$, which results in a 21.29% error, this is much smaller than the 50.93% error that was achieved via the manual segmentation.

The optimization trial was then repeated for the 60mm, 40mm, 30mm and 10mm diameter anomalies. This can be seen in the Tables 5.18, 5.19, 5.20 and 5.21

Table 5.18: *Table indicating the thermal images and processed images taken with the Seek Thermal camera at various distances of 750mm, 1750mm, 2750mm of a 60mm diameter anomaly after optimization has occurred.*

60mm Diameter Anomaly			
OD $[mm]$	**Seek Image**	**Processed Image**	**Area** $[mm^2]$
750	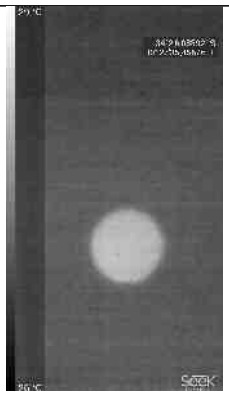		2225.27
1750	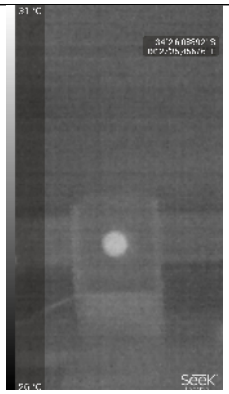	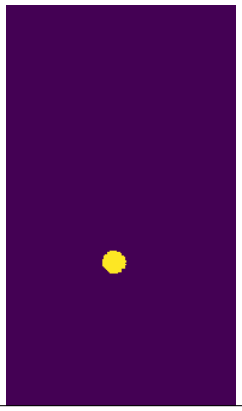	1937.24

60mm Diameter Anomaly			
OD $[mm]$	**Seek Image**	**Processed Image**	**Area** $[mm^2]$
2750	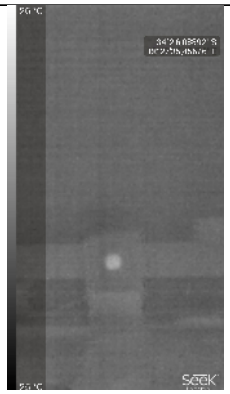	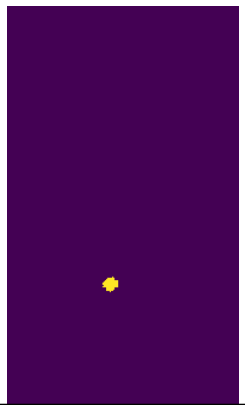	1858.21

Table 5.19: *Table indicating the thermal images and processed images taken with the Seek Thermal camera at various distances of 750mm, 1750mm, 2750mm of a 40mm diameter anomaly after optimization has occurred.*

40mm Diameter Anomaly			
OD $[mm]$	**Seek Image**	**Processed Image**	**Area** $[mm^2]$
750		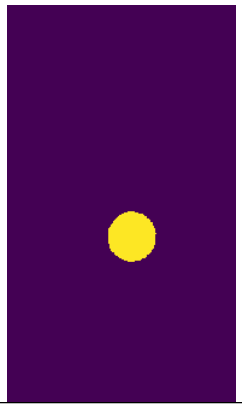	1393.1
1750	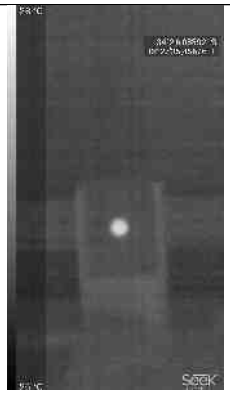	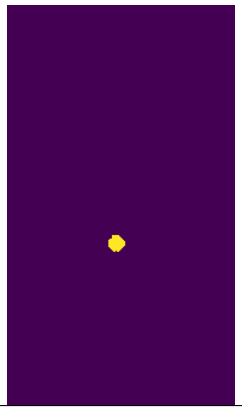	829.61

40mm Diameter Anomaly			
OD $[mm]$	**Seek Image**	**Processed Image**	**Area** $[mm^2]$
2750		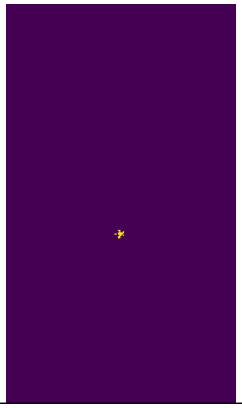	408.61

Table 5.20: *Table indicating the thermal images and processed images taken with the Seek Thermal camera at various distances of 750mm, 1750mm, 2750mm of a 30mm diameter anomaly after optimization has occurred.*

30mm Diameter Anomaly			
OD $[mm]$	**Seek Image**	**Processed Image**	**Area** $[mm^2]$
750	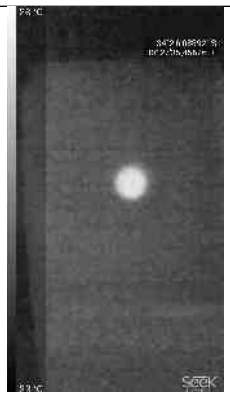	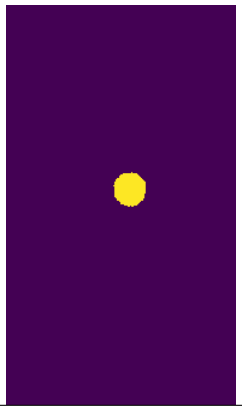	734.17

30mm Diameter Anomaly			
OD $[mm]$	**Seek Image**	**Processed Image**	**Area** $[mm^2]$
1750		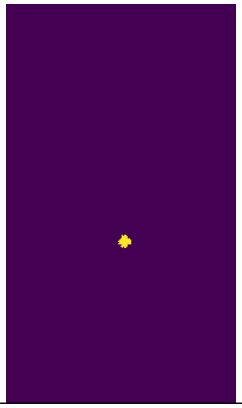	511.05
2750		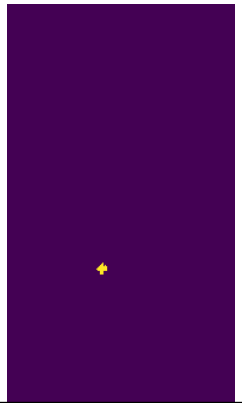	778.31

Table 5.21: *Table indicating the thermal images and processed images taken with the Seek Thermal camera at various distances of 750mm, 1750mm, 2750mm of a 10mm diameter anomaly after optimization has occurred.*

10mm Diameter Anomaly			
OD $[mm]$	**Seek Image**	**Processed Image**	**Area** $[mm^2]$
750	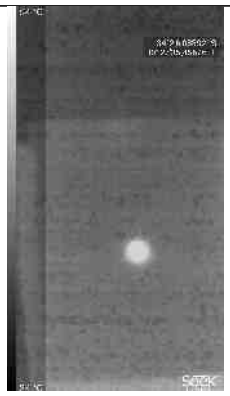	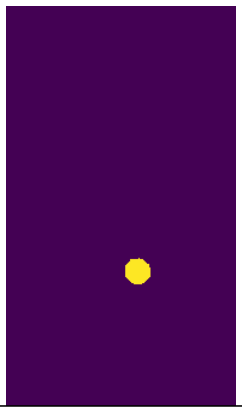	442.66
1750		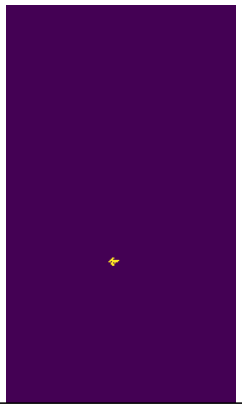	201.49
2750		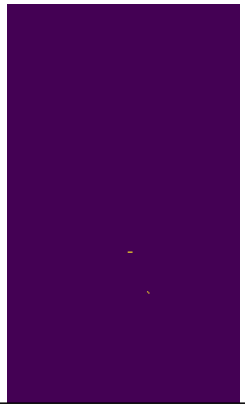	95.90

It should be noted that the segmentation had occurred only for images up to and including a distance of 2750mm. The results of the images taken at further distances yielded no results and were thus not added. A possible reason for this lack in results could be due

to the misunderstanding of the actual camera dynamics and hence the formula used to calculate the actual area. However, this has been assumed to be correct for the purpose of this experiment. The results from the Tables 5.18, 5.19, 5.20 and 5.21 were then recorded and analysed and can be seen in Tables 5.22, 5.23, 5.24 and 5.25 respectively.

Table 5.22: *Table indicating the results from the Automatic Segmentation experiments from the images in Table 5.18 taken with the Seek Thermal camera at various distances of 750mm, 1750mm, 2750mm of a 60mm diameter anomaly.*

Distance $[mm]$	**750**	**1750**	**2750**	**3750**	**4750**
Actual $[mm^2]$	2827.43	2827.43	2827.43	2827.43	2827.43
Calc $[mm^2]$	2225.27	1937.24	1858.21	NA	NA
Error $[\%]$	21.30	31.48	34.27	NA	NA
Diameter $[mm]$	53.23	49.67	48.64	NA	NA

Table 5.23: *Table indicating the results from the Automatic Segmentation experiment from the images in Table 5.19 taken with the Seek Thermal camera at various distances of 750mm, 1750mm, 2750mm of a 40mm diameter anomaly.*

Distance $[mm]$	**750**	**1750**	**2750**	**3750**	**4750**
Actual $[mm^2]$	1256.64	1256.64	1256.64	1256.64	1256.64
Calc $[mm^2]$	1393.10	829.61	408.61	NA	NA
Error $[\%]$	9.80	33.98	67.48	NA	NA
Diameter $[mm]$	42.12	32.50	22.81	NA	NA

Table 5.24: *Table indicating the results from the Automatic Segmentation experiment from the images in Table 5.20 taken with the Seek Thermal camera at various distances of 750mm, 1750mm, 2750mm of a 30mm diameter anomaly.*

Distance $[mm]$	**750**	**1750**	**2750**	**3750**	**4750**
Actual $[mm^2]$	706.86	706.86	706.86	706.86	706.86
Calc $[mm^2]$	734.17	511.05	778.31	NA	NA
Error $[\%]$	3.72	27.70	10.11	NA	NA
Diameter $[mm]$	30.57	25.51	31.48	NA	NA

A url to the codes used for the results of this section can be found on Github at `https://github.com/NaadirV/IR_DRONE_WORK/blob/master/Codes/Automatic_Segmentation_Algorithm.ipynb`

Table 5.25: *Table indicating the results from the Automatic Segmentation experiment from the images in Table 5.21 taken with the Seek Thermal camera at various distances of 750mm, 1750mm, 2750mm of a 10mm diameter anomaly.*

Distance $[mm]$	**750**	**1750**	**2750**	**3750**	**4750**
Actual $[mm^2]$	78.54	78.54	78.54	78.54	78.54
Calc $[mm^2]$	442.66	201.49	95.90	NA	NA
Error $[\%]$	463.61	156.54	22.10	NA	NA
Diameter $[mm]$	23.74	16.02	11.05	NA	NA

Conclusions:

On visual inspection of the results seen from Tables 5.18 to 5.21, it is generally seen as though the actual figure being segmented is different from the anomaly being presented, especially for those of the 60mm diameter anomaly. When measured at 750mm, it appears to be extremely irregular and when measured at 1750mm and 2750mm, it appears to be a lot smaller than it's original size as seen in its comparative greyscale image. With regards to the 40mm diameter and 30mm diameter anomalies, they appear to be much more regular in shape and similar in size for all distances especially when being compared to there corresponding greyscale images.

When visually inspecting the 10mm diameter anomaly in Table 5.21, it is seen that for the distance of 750mm, the anomaly appears to be processed in a manner that results in it maintaining its shape. For the image taken at 1750mm, its shape is not maintained and lastly when taken at 2750mm, one can see influence from unwanted noise as well as hardly see the anomaly itself.When comparing the results seen in Tables 5.18, 5.19, 5.20 and 5.21 to those acquired and displayed in Tables 5.22, 5.23, 5.24 and 5.25, the results indicate the following:

60mm Anomaly

It is observed that the highest error obtained, was for the furtherest measurement of 2750mm, with an error of 34.27%, it resulted in a calculated diameter of 48.64mm, which is only 11.36mm smaller than the actual diameter of 60mm. It must also be mentioned that this was 0.42% larger than when manual segmentation had occurred. The smallest error of 21.30% was observed at 750mm and resulted in a measured diameter of 53.23mm which is only 6.77mm smaller than the actual diameter.

40mm Anomaly

It is observed that the highest error obtained, was for the furtherest measurement of

2750mm, with an error of 67.48%, it resulted in a calculated diameter of 22.81mm, which is 17.19mm smaller than the actual diameter of 40mm. It must also be mentioned that this was 23.19% smaller than when manual segmentation had occurred at the same distance. The smallest error of 9.80% was observed at 750mm and resulted in a measured diameter of 42.12mm which is only 2.12mm bigger than the actual diameter.

30mm Anomaly

It is observed that the highest error obtained, was for the middle most measurement of 1750mm, with an error of 27.70%, it resulted in a calculated diameter of 25.51mm, which is only 4.49mm larger than the actual diameter of 30mm. It must also be mentioned that this was 5.03% smaller than when manual segmentation had occurred. In addition, it is only 1.07% larger than the smallest error that had been recorded for the 30mm anomaly under manual segmentation. The smallest error of 3.72% was observed at 750mm and resulted in a measured diameter of 30.57mm which is only 0.77mm larger than the actual diameter.

10mm Anomaly

It is observed that the highest error obtained, was for the closest measurement of 750mm, with an error of 463.61%, it resulted in a calculated diameter of 23.74mm, which is 13.74mm larger than the actual diameter of 10mm. It must also be mentioned that this was 462.18% larger than when manual segmentation had occurred. The smallest error of 22.10% was observed at 3750mm and resulted in a measured diameter of 11.05mm which is only 1.05mm larger than the actual diameter.

Overall

After comparing all the results in the Automatic segmentation algorithm tests with those in the Area test, it was generally noticed that when manual segmentation had occurred, the shape was preserved a lot better than in comparison to the automatically segmented cases, however, for the measured cases, it appears that generally area, in terms of physical size, is conserved better for the automatically segmented cases.

The automatic segmentation algorithm does however have a problem with the measurement of targets that are far away, but one can assume that this would be due to the relatively poor resolution of the thermal camera as well as the ambient background noise in the images taken. In addition, the fact that errors were observed eventhough the number of pixels were recorded and then used in the algorithm suggest that the camera dynamics are incorrectly understood and therefore further work is necessary.

5.3.2 The drone flight test

The aim of this experiment is to ensure that the selected low cost drone can fully survey a building within it's designated flying time utilising the protocol developed by Entrop et al [26].

Apparatus:

This experiment requires the use of a low cost drone, weights, a stop watch and a building for the purpose of surveying.

The Parrot AR.Drone2.0 (Elite Edition) will be used for this experiment as seen in figure 5.32 below. The drone is cheap and can be purchased for R3 505.00, it therefore fits the cost constraints [80]. The drone also has the following specifications [81]:

Figure 5.32: *Image showing the Parrot Ar.Drone2.0 quadcopter that will be used for the building survey.*

- **Running Speed:** 18km/h
- **Weight:**
  - without the hull: 366g
  - with indoor hull: 436g
  - with outdoor hull: 400g
- **Dimensions:**
  - without the hull: 45 × 29 cm
  - with indoor hull: 51.5 × 51.5 cm
  - with outdoor hull: 45.2 × 45.2 cm
- **Battery:**

  - Lithium polymer battery (3 cells, 11.1V, 1000 mAh)
  - Charging time: 1h30
  - Running time: 12min
- **Range:** 45m

Procedure:

Using the University of Twente developed protocol as seen in Figure 2.5 above, the drone will be fully charged and made to survey the chosen building. Due to the fact that a drone with gimbal and thermal camera attached could not be acquired, a readily available low cost drone will be used and weighted in order to account for the addition of a thermal camera, smart phone and gimbal. The Outdoor hull will be weighted with an additional 15g to compensate for the mass of the IR camera. It is speculated that in the case of a successful operational unit, one can utilize the on-board micro controller to trigger image taking from the IR camera. In cases where the drone should have been used to take images, a pause of 5 seconds will be used in order to compensate for the necessary time that it would otherwise take to capture an IR image.

It should also be noted that depending on the nature of the survey and what is being surveyed, the time of flight and weather conditions are of utmost importance. Due to the fact that this survey will be for the purpose of anomalies detection, the most suitable time, which would provide the best results to would be before sunrise as it is cooler during these hours and one will not receive interference from reflections of the sun.

Table 5.26: *Table indicating the flight procedures used for the final drone flight test on the Mathematics Building at the University of Cape Town as described by the protocol developed by the University of Twente.*

#	Co-ordinates	Height	Description	Picture
1a	Set-up point -33.957541;18.461326	Ground Level 0m	For this experiment, the Mathematics building at the University of Cape Town was to be surveyed. The building is a 3 storey structure with 2 tall trees on the North North Westerly side of the building. The set-up point will be on the Jameson Plaza marked in red.	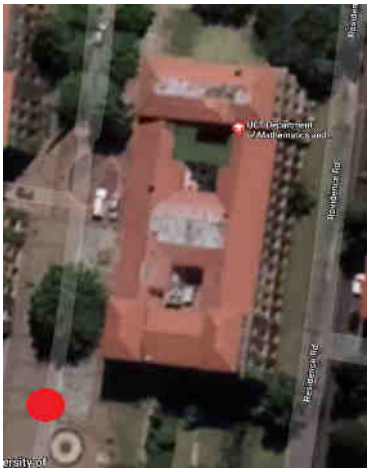

#	Co-ordinates	Height	Description	Picture
1b	Increase height -33.957541;18.461326	1.5m	As per SACAA (South African Civil Aviation Act), the drone or RPAS(Remotely Piloted Aircraft System) must first be approved by the South African civil Aviation Authority. Permission must also be granted to operate the RPAS within 50m [82].	
1c	Starting point -33.957467;18.461373	1.5m	The point of take off will be also used as a point of assembly for the drone as marked in green.	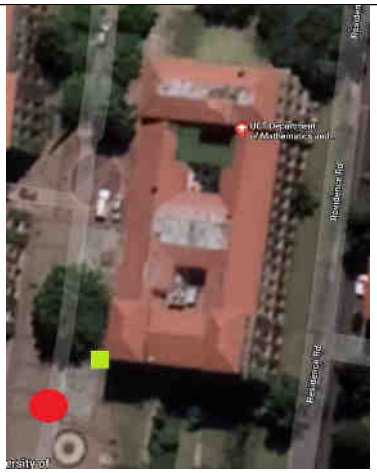
1e	Starting point -33.957467;18.461373	1.5m	The drone will be piloted from the Jameson Plaza and will be followed throughout its flight path so as to keep it in constant sight.	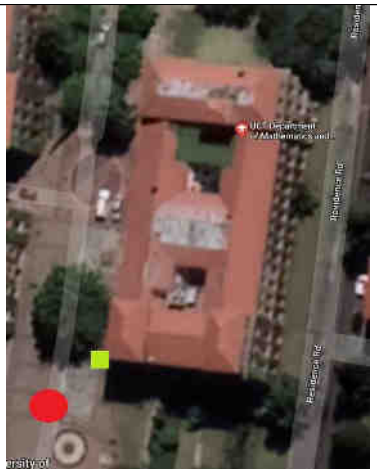

#	Co-ordinates	Height	Description	Picture
2a	Increase height to roof line -33.957467;18.461373	1.5m 2.8m 4.1m 5.4m 6.7m 8m 9.3m	The drone will be taking images at a distance of 2m from the building. The images will be focused on corners, open walls, and vents. Images will also be taken of the roof-lining. In addition, the drone must always fly perpendicular to the area of interest.	
2b	Maintain height -33.957467;18.461373 -33.956967;18.461459	9.3m	The drone will be piloted from the Jameson Plaza and the drone will be followed throughout its flight path.	
2d	Decrease height -33.956967;18.461459	9.3m 8m 6.7m 5.4m 4.1m 2.8m 1.5m	A secondary landing sight will be on the lawn on the North side of the building in the event of any unplanned circumstances as highlighted by the blue X.	

#	Co-ordinates	Height	Description	Picture
3a	Increase height and continue -33.956967;18.461459 -33.956987;18.461740	9.3m	The Seek Thermal Compact will be used for the imaging of the of the building using the greyscale colour pallet as this will ensure simpler processing of the images using the algorithm described in experiment 4.	
3b	Decrease height -33.956987;18.461740	9.3m 8m 6.7m 5.4m 4.1m 2.8m 1.5m	The drone will begin the flight from the Jameson Plaza and fly along the North North Western side of the building at an altitude of above the ground level so as to take images at the point of meeting between the wall and roof whilst maintaining a distance of 2m from the structure at all times. A total of 128 images will be taken along the roof line. 28 images will be taken on the corners and 12 images will be taken of the walls of the building.	
3c	Increase height and continue -33.956987;18.461740 -33.957494;18.461652	9.3m	The drone will be 2m away from the structure at all times with the flight path indicated in white.	

#	Co-ordinates	Height	Description	Picture
3d	Decrease height -33.957494;18.461652	9.3m 8m 6.7m 5.4m 4.1m 2.8m 1.5m	The total time for imaging is calculated to be 14 minutes. A further 2 minutes and 39 seconds should be allotted for flight time between imaging points (see calculations below). A further 30 seconds will be added as a safety. Thus a total of 17 minutes and 9 seconds will be necessary for the operation.	
4a	Increase height and move to starting point -33.957494;18.461652 -33.957467;18.461373	9.3m	The entire surveying flight path is shown in white.	
4c	Decrease height and move to set-up point -33.957541;18.461326 -33.957467;18.461373	1.5m 0m	The battery capacity of the chosen drone is only 12 minutes, therefore, the survey will have to take part in two parts. with the first part taking place until the moment mentioned in 3b. Thereafter, the drone will move to the secondary landing sight and be recharged before continuing with the flight path and eventually landing at the set up sight marked in red.	

Figure 5.33: *Figure showing the flight path in white along the Northern breadth and side of the Mathematics Building at the University Cape Town which will be surveyed as part of the Flight test.*

Figure 5.34: *Figure showing the flight path in white along the length of the Mathematics Building at the University Cape Town which will be surveyed as part of the Flight test.*

Figure 5.35: *Figure showing the flight path in white along the Southern breadth and side of the Mathematics Building at the University Cape Town which will be surveyed as part of the Flight test.*

Time Calculation for flight path:

Given that the drone will be 2m from the building at all times, using trigonometric calculations as seen in Figure 4.2 together with the 36°FOV, a distance of 1.2996m can be covered with a single image. Given that the building has the following specifications:

- **Length:** 55m
- **Width:** 26m
- **Height:** 9.5m to the roof line.

The number of images is therefore calculated as follows;

$$Images_{param} = \frac{parmeter \times \#.sides}{image\ distance} = \#.\ images \tag{5.17}$$

$$Images_{length} = \frac{55 \times 2}{1.2996} = 84.6414 = 86\ images * \tag{5.18}$$

$$Images_{Width} = \frac{26 \times 2}{1.2996} = 40.0123 = 42\ images * \tag{5.19}$$

$$Images_{Height} = \frac{8 \times 4}{1.2996} = 24.6230 = 28\ images * \tag{5.20}$$

$$Images_{Sidewall} = 12\ images \tag{5.21}$$

The total number of images, with the assumption of no overlaps occurring, is therefore:

$$86 + 42 + 28 + 12 = 168\ images \tag{5.22}$$

*It should be noted that the number of images must be rounded to the nearest whole number and should be an even number so as to ensure an equal number of images are taken of each side.

One can then use the equation of motion below to calculate the required flight time of the quadcopter between imaging points.

$$\Delta x_f = \Delta x_i + \frac{1}{2}(v_i + v_f)\Delta t \tag{5.23}$$

Where:

- Δx_f - Final Displacement = 1.2996m
- Δx_i - Initial Displacement = 0m
- v_i - Initial Velocity = $0m.s^{-1}$

- v_f - Final Velocity = $5m.s^{-1}$
- Δt - Change in time = 0.8660s

One can then calculate the total time necessary for the complete Flight test to take place using the formula below:

$$t_{Total} = t_{flight} + t_{images} + t_{safety} \tag{5.24}$$

Where:

$t_{flight} = \Sigma(Images_{param} \times \Delta t)$

$t_{images} = \Sigma(5 \times Images_{param})$

$$t_{Total} = (0.866 \times 86) + (0.866 \times 42) + (0.866 \times 28) + 13.12^{*} + (0.866 \times 12) \tag{5.25}$$

$$+(168 \times 5) + 30^{*} = 1028.61s = 17m09s$$

* The additional 13.12s has been added to the total time above as it incorporates the time necessary for drone to increase its altitude along the height of the building after it has taken its images whilst declining. In addition, 30s were added as a safety factor for unaccounted complications when flying.

Controlled Variables:

- The points at which the images are taken.
- The flight path.

General Assumptions:

It will be assumed that the building surveyed will be a fair representation in terms of a building that would usually be surveyed with respected to surface area being covered.

Expected Results:

If the drone datasheet is reliable and the calculations have been done correctly, the drone should be able to survey the entire building within 2 battery capacity cycles.

Actual Results:

The survey was timed and both parts were completed in a time of 16 minutes and 58 sec-

(a) Set-up point.

(b) Southern Side wall.

Figure 5.36: *Optical images of (a) Set-up point and (b) Southern Side Wall of the Mathematics Building during the flight test at UCT upper campus.*

(a) North North Western roof-line.

(b) Northern Side wall.

Figure 5.37: *Optical images of the (a) North North Western roof-line and (b) Northern Side Wall of the Mathematics Building during the flight test at UCT upper campus.*

Figure 5.38: *Figure showing the secondary landing sight that was used for the drone flight test.*

onds which occurred within two charged battery cycles. All stops for images were taken into account and both landing sights were successfully used.

Conclusions:

Given the results of the experiment, one can say that the experiment was a success

and that as a prototype, a low cost drone can be used to survey a building. It can also be confirmed that the Parrot AR.Drone 2.0 can indeed be used for surveying purposes. However, it is worth noting that this low cost drone is no longer in production, but can still be bought from some local retailers. An upgraded Parrot Bebop or Parrot Mambo seems to have replaced the AR and should thus be looked into in addition to the drones mentioned in Table 4.3.

It is also of utmost importance that when one attempts to survey a building, they should be aware of the limitations of the drone as well as be experienced in piloting that particular drone; this can save a lot of time and money as well as result in a far more efficient survey.

Chapter 6

Conclusions, Limitations and Future Work

This chapter provides a look at the conclusions and limitations of the project from a procedural and experimental point of view whilst referring to the results in the completed tests. In addition, we provide a comparison between our recommended system and current available systems. Lastly, we look at possible recommendations for the future works to be completed on this endeavour.

6.1 Conclusions

When looking at the available IR-drone products available today, the project, aimed to provide the ground work for producing a drone coupled with and IR camera that can be used as a cost-effective solution for effective building envelope surveying. There were 8 Acceptance Test Procedures as seen in Chapter 3, Table 3.4 and experiments that were completed as well in order for this project to be realised. They will be validated against the requirements from which they were set.

A1. *The system will we weighed after it is tested.*
Satisfied
When using the AR. Parrot Drone, the entire system: Drone (372.4g) + Samsung S4 Smartphone (135.1g) + IR camera(13.2g) = 520.7g which is below the 1.8kg as per the requirement.

A2. *A range test for operability shall be conducted.*

Not Satisfied
When using the AR. Parrot Drone, it proved to operate as high as 42m.

A3. *A flight test shall be conducted to monitor the time the drone can be tested for.*
Satisfied
When using the AR. Parrot Drone, the drone was able to fly for 12min in one battery cycle.

A4. *Specifications shall be checked when deciding on the thermal Camera for use.*
Satisfied
Seek Thermal operates on objects within -40°C - 330°C.

A5. *Images shall be processed to determine the area of a known anomaly.*
Partially Satisfied
Whilst the area of an anomaly could be calculated using the algorithms, the accuracy was not always within the acceptable 10% error region. In addition, the shape of the anomaly was not always conserved.

A6. *Images shall be processed to determine the number of anomalies present in a known environment.*
Partially Satisfied
Most of the processed images resulted in the correct number of anomalies being detected, however, for further distances, the correct number was not given due to unwanted noise within the image which was treated as an anomaly.

A7. *The IR camera shall be validated against a thermometer as a means for accurate temperature measurement.*
Satisfied

A8. *Images shall be processed to determine the average temperature of a surveyed environment.*
Satisfied

Overall, when looking at the project at a whole, one can say that the idea of a low cost IR-drone set-up is certainly plausible, given that that all the ATP's except one were fully satisfied. It should be mentioned that the ATP that was not satisfied can easily be overcome by purchasing the UpOne Air drone as mentioned in the section on Drone selection in Chapter 4.

With regards to the experiments, most experiments were successful in that results were obtained.The overall cost of the equipment used was namely the Seek Thermal Compact

IR camera (R3656.00) + AR.Parrot Drone(R3505.00) was R7161.00, which is within the R10 000 as budgeted for, hence one can do the surveying at low cost.

6.2 Limitations

6.2.1 IR Camera Limitations

Whilst most of the experiments that were tested during duration of this project were successful in terms of meeting the ATP's, there did appear to be many limitations throughout.

Firstly, the resolution of the camera was not ideal for the processing that had occurred. Whilst the results can be obtained as seen in the previous sections. If the resolution was better, the results obtained would have been better with respect to the accuracy received in the area and detection tests. One suspects that anomalies might be detected from a further range and with a smaller error. However, the camera is indeed value for money as it has the best resolution for its price and can indeed be used for anomaly detection as theorized

Secondly, the camera changes the colour scale with respect to environment in which it is used. This makes sense for environments with a large temperature difference as the camera would need to display all the different temperature values with a fixed number of colours. Whilst this is great for the workings of the camera, it makes the algorithm set-up particularly difficult as one would need to change the scales that represent certain intensities.
Thirdly, we suspect that the relationship between FOV, distance and pixel size is not completely understood with respect to how the camera registers the image. We also suspect that it is one of the reasons for the large errors in our calculations and results.
The export regulations were also a major limitation during the course of this project as they did not allow us to purchase the FLIR IR camera as we would have liked and the shipping time to South Africa has also been excessively timely.

The environment in which the experiments were conducted were not necessarily the best as there was a lot of background noise which affected the colour scale on the camera when the images were taken. In addition, the material used whilst doing the experiment did conduct heat, hence the area of the anomaly being processed could not be accurately found as the heated part of the material was registered as part of the anomaly itself.

6.2.2 Drone Limitations

As with the IR camera, when doing the drone test, most of the ATP's were realized apart from the range test. If the UpOne Air drone is used, this can be realized as the range is 1000m. In addition to the IR cameras, there were also export regulation issues with the drone as it could not ship to South Africa. There are other drones such as the Parrot Beebop which can be used instead of the Parrot, but there are other low cost DIY drones that can be used.

Secondly, the control on the AR.Parrot was not ideal for the stop start motion that was necessary for images to be taken, but nevertheless, it is possible to be done with such a drone.

6.3 Comparisons

This section provides a brief comparison between our recommended system and two available coupled thermal imaging and drone systems.

Table 6.1: *Table showing the comparison between three IR-drone setups, namely the Seek Thermal and AR Parrot, The Mavic Enterprise 2 Dual and the Inspire 1 - Zenmuse XT*

IR Camera Name	SEEK Thermal Compact	Mavic Enterprise 2 Dual	Zenmuse XT
Image			
Temp Range [°C]	-40 : 330	-10 : 400	-10 : 40
IR Resolution	206×156	160×120	640×512
FOV [°]	36×36	57×57	90×69
Mass [g]	13.2	-	270
Price [R]	3 656.00	-	122 560
Drone Name	AR. Parrot Drone	Mavic Enterprise 2 Dual [83]	Inspire - 1[84]
Image			
Flight Time [min]	12	32	18
Range [m]	50	6 000	2 500
Mass [g]	372.4	-	3 500
Price [R]	3 505.00	-	30 488.15
Total Mass [g]	520.7	905.0	3 770
Total Price [R]	7 160.00	41 164.34	205 309.20

6.4 Future Work

It is recommended that in the future, when conducting similar experiments as those done in this project firstly, more images should be taken in order to validate the sensor, this will lead to better statistical results and give more accurate readings. Secondly, it would be ideal to do the Area and detection tests with a material that is used in an actual building envelope such as concrete or brick, however, one must ensure that the they have the correct tools to cut the holes. A regular drill will not work and a masonry drill will result in the material breaking. A diamond tipped bit works best.

Also ensure that the environment is thermally sealed when doing tests, this will ensure better results from the variable that you are measuring with the IR camera. Also ensure that you have a stand or tripod of some sort when taking your images as this also increases the clarity of the image. Make sure that the colour palette you are using is also the correct one in order to highlight certain features of interest.

If one does intend to make the images greyscale before processing, it is advised that you take the image as a greyscale image to begin with as converting later can cause some of the bits to appear as if they were another colour due to the fact that they have been changed from 256×3 to just 256 greyscale.

For image processing, as a future recommendation, the use of Machine learning algorithms will be advantageous as well use Random-Walker segmentation. Perhaps the training set can be used to identify thermal anomalies. In addition segmentation can also be done via Artificial Neural Networks (ANN) which provide a rather elaborate solution to the problem.

More testing needs to be done on real world structures such as buildings, bridges, pipelines and dam walls in order to get a more realistic idea of what crack detection is possible. Utilization of the system in factories and industries is also recommended in order to evaluate ventilation in such spaces - this can be done via the continuous use of IR-drone set-ups and will be used to see how effective current ventilation is in the factory environment . A validation between current bridge sensors and this technology may also be feasible for the maintenance industry. Most importantly, testing needs to be done in order to validate the theory of using a window area to validate the threshold. Lastly, a look into the medical industry with IR imaging may also prove to be lucrative as a form of non-invasive-testing that can be used to detect illnesses that affect the thermoregulatory centres on individual.

With regards to the drone, it is recommended to use a drone that has loiter function-

ality. This allows the drone to be completely still at the point of imaging which will ultimately result in a less distorted image with more clarity. It is also recommended to get an experienced pilot to do the flights to ensure that the best results are received. In addition, the best time to do the do the survey would be dawn as this will produce images that contain the least interference from the sun and be the best time to see the thermal difference between the interior and exterior of the building envelope.

As a final recommendation, in addition to the protocol developed by the University of Twente, I feel as though it is mandatory to have a regulatory form that can be used as a formal document of legality for surveying purposes. A template document can be found on the next page.

All codes and images used in this dissertation can be at the following Github Link `https://github.com/NaadirV/IR_DRONE_WORK`

Infra Red Unmanned Aerial Vehicle Survey Form (IRUAVSF)

Company Details:

Purpose of the Survey:

UAV used: _____ IR camera used: _____

Location of Survey: (Physical Address:)

Location Boundary: (Co-ordinates)

Expected Duration of Survey: Start:_____ Stop: _____

General check:(tick)

UAV Regulation ☐ Permission for survey ☐ Flight Path ☐ Set-up sight ☐

Primary Landing ☐ Secondary Landing ☐ 72 hour Notice ☐

Name: _____

Signature: _____

Bibliography

[1] S. Cox, "Building energy codes: Policy overview and good practices," NREL (National Renewable Energy Laboratory (NREL), Golden, CO (United States)), Tech. Rep., 2016.

[2] UNEP, *Building Design and Construction: Forging Resource Efficiency and Sustainable Development*, June 2012.

[3] X. Sun, M. A. Brown, M. Cox, and R. Jackson, "Mandating better buildings: a global review of building codes and prospects for improvement in the united states," *Wiley Interdisciplinary Reviews: Energy and Environment*, vol. 5, no. 2, pp. 188–215, 2016.

[4] R. Young, S. Hayes, M. Kelly, S. Vaidyanathan, S. Kwatra, R. Cluett, and G. Herndon, "The 2014 international energy efficiency scorecard," in *American Council for an Energy-Efficient Economy*, 2014.

[5] R. A. Athalye, D. Sivaraman, D. B. Elliott, B. Liu, and R. Bartlett, "Impacts of model building energy codes," Pacific Northwest National Lab.(PNNL), Richland, WA (United States), Tech. Rep., 2016.

[6] M. LaFrance *et al.*, "Technology roadmap: Energy efficient building envelopes," in *Energy Technol. Pol. Div.* IEA, 2013.

[7] J.-J. Kim and J. W. Moon, "Impact of insulation on building energy consumption," in *Building Simulation*, vol. 2009. Citeseer, 2009, pp. 674–680.

[8] U.S. Department of Energy. Building Envelopes. (2019). [Online]. Available: https://betterbuildingsinitiative.energy.gov/alliance/technology-solution/building-envelope

[9] P. De Wilde, "The gap between predicted and measured energy performance of buildings: A framework for investigation," *Automation in Construction*, vol. 41, pp. 40–49, 2014.

[10] A. Raheem, "Use of Drone and Infrared Camera for a Campus Building Envelope Study," Master's thesis, East Tennessee State University, 2016.

[11] J. Lucas, "What is Infrared?" *Live Science*, vol. Planet Earth, March 26, 2015.

[12] Sapling Learnung. Electromagnetic spectrum. (2017). [Online]. Available: https://sites.google.com/site/chempendix/em-spectrum

[13] B. Pavlin, G. Pernigotto, F. Cappelletti, P. Bison, R. Vidoni A. Gasparella, "Real-time Monitoring of Occupants' Thermal Comfort through Infrared Imaging: A Preliminary Study," *MDPI*, 2017.

[14] Wikipedia. ASHRAE 55. (2018, March 26). [Online]. Available: https://en.wikipedia.org/wiki/ASHRAE55

[15] AUTODESK. Thermal Comfort. (2017). [Online]. Available: https://sustainabilityworkshop.autodesk.com/buildings/human-thermal-comfort

[16] M. Kato, J. Sugenoya, T. Matsumoto, T. Nishiyama, N. Nishimura, Y. Inukai, T. Okagawa, H. Yonezawa, "The effects of facial fanning on thermal comfort sensation during hyperthermia." *PubMed*, vol. 443, pp. 175–179, 2001.

[17] H. Liu, J. Liao, D. Yang, X. Du, P. Hu, Y. Yang, B. Li,, "The response of human thermal perception and skin temperature to step-change transient thermal environments." *Build.Environ*, vol. 73, pp. 232–238, 2014.

[18] N.D. Dahlan, Y.Y. Gital,, "Thermal sensations and comfort investigations in transient conditions in tropical office." *PubMed*, vol. 54, pp. 169–176, 2016.

[19] D. Wang,H. Zhang,E. Arens,C. Huizenga,, "Observations of upper-extremity skin temperature and corresponding overall-body thermal sensations and comfort." *Build.Environ*, vol. 42, pp. 3933–3943, 2007.

[20] F. De Oliveira, S. Moreau, C. Gehin, A. Dittmar,, "Infrared imaging analysis for thermal comfort assessment." in *In Proceeding of the 29th Annual International Conference of the IEEE Engineering in Medicine and Biology Society,*, editor, Ed.

[21] P. Andrew, "Using Thermal Cameras to Promote Energy Efficiency in Buildings," 2016.

[22] International Energy Agency. Technology Roadmap: energy efficient building envelopes. (2013, December 18). [Online]. Available: https://webstore.iea.org/technology-roadmap-energy-efficient-building-envelopes

[23] V. Khatereh, A. de Melo e Silva Henrique, D.K. Harris, T.M. Ahlborn, "Application of thermal ir imagery for concrete bridge inspection." *PCI/NBC*, 2011.

[24] The American Society of Non-destructive Testing. Introduction to Nondestructive Testing. (2019). [Online]. Available: https://www.asnt.org/MinorSiteSections/AboutASNT/Intro-to-NDT

[25] J. Crisóstomo and R. Pitarma, "The importance of emissivity on monitoring and conservation of wooden structures using infrared thermography," *IntechOpen*, 2019.

[26] A.G. Enthrop, A. Vasenev, "Infrared drones in the construction industry: designing a protocol for building thermography procedures," *Energy Procedia*, 2017.

[27] E. Solberg. Cooled Vs. Uncooled Thermal Cameras for Long-Range Surveillance. (2013, October 24). [Online]. Available: http://www.thermalvideo.com/blog/cooled-vs-uncooled-thermal-cameras-for-long-range-surveillance

[28] FLIR, "IR Detectors for Thermographic Imaging," p. 4.

[29] lady ada. How PIR's work. [Online]. Available: https://learn.adafruit.com/pir-passive-infrared-proximity-motion-sensor/how-pirs-work

[30] Jaeseok Yun, Sang-Shin Lee, "Human Movement Detection and Idengification Using Pyroelectric Infrared Sensors," *sensors*, vol. 4, Issue 5, 5 May, 2014.

[31] Y. Watabe, Y. Honda, K. Aizawa, and T. Ichihara, "Infrared sensor," May 22 2001, uS Patent 6,236,046.

[32] T. Target. Seebeck Effect. 2008, December. [Online]. Available: https://searchnetworking.techtarget.com/definition/Seebeck-effect

[33] Wang, Hongchen; Xinjian Yi, Jianjun Lai and Yi Li . Microbolometer. (2007). [Online]. Available: http://enacademic.com/dic.nsf/enwiki/937915

[34] K. Sheets, "What is a digital image," *LearnImageJ*, p. 2, 2013.

[35] E. Anjna, E. R. Kaur, "Review of Image Segmentation Technique," *International Journal of Advanced Research in Computer Science*, vol. 8, No.4, May, 2017.

[36] Dwayne Phillips. Image processing, part 9: Histogram-based image segmentation. (1993). [Online]. Available: http://collaboration.cmc.ec.gc.ca/science/rpn/biblio/ddj/Website/articles/CUJ/1993/9302/phillips/phillips.htm

[37] Sci-kit image development team. Thresholding. (2017). [Online]. Available: http://scikit-image.org/docs/dev/auto_examples/xx_applications/plot_thresholding.html

[38] S. U. Lee, S. Y. Chung, and R. H. Park, "A comparative performance study of several global thresholding techniques for segmentation," *Computer Vision, Graphics, and Image Processing*, vol. 52, no. 2, pp. 171–190, 1990.

[39] J. Canny, "A computational approach to edge detection," *IEEE Transactions on pattern analysis and machine intelligence*, no. 6, pp. 679–698, 1986.

[40] Ruye Wang. Canny Edge Detection. (2013, September 25). [Online]. Available: http://fourier.eng.hmc.edu/e161/lectures/canny/node1.htmll

[41] Wikipedia. Canny Edge Detection. (2018, September 24). [Online]. Available: https://en.wikipedia.org/wiki/Canny_edge_detector

[42] Scikit-image. Edge-based Segmentation. (2018, October 27). [Online]. Available: http://scikit-image.org/docs/dev/auto_examples/xx_applications/plot_coins_segmentation.html

[43] M. Mueller, K. Segl, and H. Kaufmann, "Edge-and region-based segmentation technique for the extraction of large, man-made objects in high-resolution satellite imagery," *Pattern recognition*, vol. 37, no. 8, pp. 1619–1628, 2004.

[44] Wikipedia. Watershed (image processing). 2018, October 11. [Online]. Available: https://en.wikipedia.org/wiki/Watershed_%28image_processing%29

[45] DRONE WORLD. Parrot Bebop-Pro Thermal. (2018). [Online]. Available: https://tinyurl.com/y95ee75b

[46] DRONE WORLD. Inspire Thermal Combo Ready-To-Fly Flir Vue Pro. (2018). [Online]. Available: https://tinyurl.com/yczyvgxj

[47] Wikipedia. Climate of South Africa. 2016, November 19. [Online]. Available: https://en.wikipedia.org/wiki/Climate_of_South_Africa

[48] SEEK. CompactXR. (2017). [Online]. Available: https://www.thermal.com/uploads/1/0/1/3/101388544/compactxr-sellsheet-usa-web.pdf

[49] adafruit. SPECIFICATIONS FOR Infrared Array Sensor . (2011, August 30). [Online]. Available: https://cdn-learn.adafruit.com/assets/assets/000/043/261/original/Grid-EYE_SPECIFICATIONS%28Reference%29.pdf?1498680225f

[50] FLIR Systems. FLIR LEPTON® 3 Long Wave Infrared (LWIR) Datasheet. (2014). [Online]. Available: https://www.flir.com/globalassets/imported-assets/document/lepton-3-engineering-datasheet-1.pdf

[51] FLIR Systems. FLIR ONE. (2018). [Online]. Available: https://www.flir.com/flirone/

[52] FLIR Systems. FLIR ONE PRO. (2017, August 06). [Online]. Available: https://www.flir.com/globalassets/imported-assets/document/17-1746-oem-flir_one_pro_datasheet_final_v1_web.pdf

[53] Dongguan Xintai Instrument Co., Ltd. . Handheld Thermal Imaging Camera (HT-02). (2009). [Online]. Available: https://hytechcn.en.alibaba.com/product/60083134636-800587624/Handheld_Thermal_Imaging_Camera_HT_02_.html

[54] FLIR Systems. FLIR DUO. (2016). [Online]. Available: https://www.flir.com/globalassets/imported-assets/document/flir-duo-datasheet.pdf

[55] FLIR Systems. FLIR Vue Pro and Vue Pro R User Guide. (2016). [Online]. Available: https://www.flir.com/globalassets/imported-assets/document/436-0013-10-vue-pro-and-r-user-guide.pdf

[56] Yuneec. Tech Specs. (2017). [Online]. Available: http://us.yuneec.com/typhoon-4k-specs

[57] FLIR Systems. Unlock the possibilities of sight. (2018). [Online]. Available: https://www.dji.com/zenmuse-xt/info

[58] F. S. AB, "INFRARED ESOLUTION AND CONTRAST ENHANCEMENT WITH FUSION," Patent US 8 520 970 B2.

[59] John V. Battle of the thermal imaging cameras: Flir one vs seek thermal compact. (2016, February 06). [Online]. Available: https://www.phonearena.com/news/Battle-of-the-thermal-imaging-cameras-FLIR-ONE-vs-Seek-Thermal-Compact_id78033

[60] DJI. Phantom 3 4K specs. (2018). [Online]. Available: https://www.dji.com/phantom3-4k/info

[61] DJI. SPARK. (2018). [Online]. Available: https://www.dji.com/spark/info

[62] DJI. DRONEISTA. (2018). [Online]. Available: https://droneista.com/upair-one-drone/

[63] Banggood. ZOP Power 11.1V 5400mah 20C 3S Lipo Battery XT60 Plug for RC Quadcopter. (2018). [Online]. Available: https://www.banggood.com/ZOP-Power-11_1V-5400mah-20C-3S-Lipo-Battery-XT60-Plug-for-RC-Quadcopter-p-1237190

[64] Tom. QUADCOPTER FLIGHT TIME: HOW TO CALCULATE? (2017, March 19). [Online]. Available: https://www.flitetest.com/articles/quadcopter-flight-time-calculator-how-to

[65] Enthought. Image Analysis in Python with SciPy and Scikit Image — SciPy 2015 Tutorial — Stefan Van der Walt. (2015, July 8). [Online]. Available: https://www.youtube.com/watch?v=olb7R1cuzyU

[66] Sci-kit image development team. Adaptive Thresholding. (2017). [Online]. Available: http://scikit-image.org/docs/0.12.x/auto_examples/segmentation/plot_threshold_adaptive.html

[67] Sci-kit image development team. Comparing edge-based and region-based segmentation. (2017). [Online]. Available: http://scikit-image.org/docs/dev/auto_examples/xx_applications/plot_coins_segmentation.html

[68] Montgomery, P. What is the accuracy of a mercury thermometer? (2017, September 13). [Online]. Available: https://www.quora.com/What-is-the-accuracy-of-a-mercury-thermometer

[69] Grigull, Ulrich, " Fahrenheit, a Pioneer of Exact Thermometry." *The Proceedings of the 8th International Heat Transfer Conference, San Francisco.*, vol. 1, pp. 9 – 18, 1966.

[70] Distribution Analyzer. Distribution Analyzer 1.2 Help. [Online]. Available: http://www.variation.com/da/help/hs141.htm

[71] Statistics how to. Paired T-Test. [Online]. Available: http://www.statisticshowto.com/probability-and-statistics/t-test/#PairedTTest

[72] R. Coe, "It's the effect size, stupid:what effect size is and why it is important," in *booktitle*, Education-Line, Ed.

[73] Simulation math. T distribution table. [Online]. Available: http://simulation-math.com/TDistTable.pdf

[74] DroneZon, "DJI Mavic Pro Reviewed With Frequently Asked Questions." [Online]. Available: https://www.dronezon.com/drone-reviews/dji-mavic-pro-highlights-review-frequently-asked-questions/

[75] Pokapū Akoranga Pūtaiao, "Heat energy," *Science Learning Hub*, 2007-2018.

[76] Python Software Foundation. Pytesseract 0.2.6. (2019). [Online]. Available: https://pypi.org/project/pytesseract/

[77] Adrian Rosebrock. Using Tesseract OCR with Python . (2017, July 10). [Online]. Available: https://www.pyimagesearch.com/2017/07/10/using-tesseract-ocr-python/

[78] Slide Share. Dilation and Erosion. (2019). [Online]. Available: https://www.slideshare.net/aswinishere007/dilation-and-erosion-39733096

[79] R. C. Gonzalez, R. E. Woods, and S. L. Eddins, "Digital image processing using matlab: And mathworks, matlab sim sv 07," 2007.

[80] Price check. Price check. (2019). [Online]. Available: https://www.pricecheck.co.za/offers/105339841/Parrot+Ar.drone+2.0+Elite+Edition+Quadcopter+-+Snow#product-details

[81] Parrot. PARROT AR.DRONE 2.0 ELITE EDITION. (2018). [Online]. Available: https://www.parrot.com/global/drones/parrot-ardrone-20-elite-edition#parrot-ardrone-20-elite-edition

[82] Dji. Drone Laws. (2018). [Online]. Available: https://www.dronedeals.co.za/south-african-drone-laws-7-most-important-rules/

[83] DJI. Mavic 2 Enterprise Series. 2019. [Online]. Available: https://www.dji.com/mavic-2-enterprise/specs

[84] DJI. Inspire Series. 2019. [Online]. Available: https://store.dji.com/product/inspire-1-v2?site=brandsite&from=buy_now_bar